การสังเคราะห์วัสดุไฮบริดนาโนคาร์บอนและแมงกานีสออกไซด์นาโนชีท สำหรับตัวเก็บประจุยิ่งยวดแบบอสมมาตร

SYNTHESIS OF NANOCARBON AND MANGANESE OXIDE NANOSHEET HYBRID MATERIALS FOR ASYMMETRIC SUPERCAPACITOR

ปาวีณา ดุลยเสรี
PAWEENA DULYASEREE

วิทยานิพนธ์นี้เป็นส่วนหนึ่งของการศึกษาตามหลักสูตรปริญญาปรัชญาดุษฎีบัณฑิต
สาขาวิชานาโนวิทยาและนาโนเทคโนโลยี
วิทยาลัยนาโนเทคโนโลยีพระจอมเกล้าลาดกระบัง
สถาบันเทคโนโลยีพระจอมเกล้าเจ้าคุณทหารลาดกระบัง
พ.ศ. 2560

KMITL-2017-NT-D-001-006

SYNTHESIS OF NANOCARBON AND MANGANESE OXIDE NANOSHEET HYBRID MATERIALS FOR ASYMMETRIC SUPERCAPACITOR

PAWEENA DULYASEREE

A THESIS SUBMITTED IN PARTIAL FULFILLMENT
OF THE REQUIREMENT FOR THE DEGREE OF
DOCTOR OF PHILOSOPHY IN NANOSCIENCE AND NANOTECHNOLOGY
COLLEGE OF NANOTECHNOLOGY
KINGMONGKUT'S INSTITUTE OF TECHNOLOGY LADKRABANT
2017

KMITL-2017-NT-D-001-006

COLLEGE OF NANOTECHNOLOGY

KING MONGKUT'S INSTITUTE OF TECHNOLOGY LADKRABANG

หัวข้อวิทยานิพนธ์	การสังเคราะห์วัสดุไฮบริดนาโนคาร์บอนและแมงกานีสออกไซด์นาโนชีทสำหรับตัวเก็บประจุยิ่งยวดแบบอสมมาตร
นักศึกษา	นางสาวปาวีณา ดุลยเสรี
รหัสประจำตัว	54670203
ปริญญา	ปรัชญาดุษฎีบัณฑิต
สาขาวิชา	นาโนวิทยาและนาโนเทคโนโลยี
พ.ศ.	2560
อาจารย์ที่ปรึกษาวิทยานิพนธ์	ผู้ช่วยศาสตราจารย์ ดร.วินัดดา วงศ์วิริยะพันธ์
อาจารย์ที่ปรึกษาวิทยานิพนธ์ร่วม	ดร.วิรัตน์ เจริญบุญ

บทคัดย่อ

งานวิจัยนี้ศึกษาเกี่ยวกับวัสดุไฮบริดนาโนคาร์บอนแบบผนังหลายชั้นกับแมงกานีสออกไซด์นาโนชีทสำหรับตัวเก็บประจุยิ่งยวดแบบอสมมาตร โดยงานวิจัยนี้ต้องการเพิ่มประสิทธิภาพของตัวเก็บประจุยิ่งยวดด้วยการเพิ่มค่าความหนาแน่นพลังงาน ซึ่งมีตัวแปรสำคัญ 2 ตัวแปร คือ ค่าความจุไฟฟ้าจำเพาะและช่วงความต่างศักย์ของขั้วไฟฟ้า ดังนั้นในงานวิจัยจึงเพิ่มค่าความจุไฟฟ้า โดยการเพิ่มหมู่ฟังก์ชันของท่อนาโนคาร์บอนแบบผนังหลายชั้น (งานวิจัยส่วนที่ 1) และโดยการสังเคราะห์วัสดุไฮบริดท่อนาโนคาร์บอนและแมงกานีสออกไซด์นาโนชีท (งานวิจัยส่วนที่ 2) และได้เพิ่มช่วงความต่างศักย์ของขั้วไฟฟ้า โดยการประดิษฐ์ตัวเก็บประจุยิ่งยวดแบบอสมมาตร (งานวิจัยส่วนที่ 3) ในงานวิจัยส่วนที่ 1 ศึกษาเกี่ยวกับการเพิ่มหมู่ฟังก์ชันของท่อนาโนคาร์บอนแบบผนังหลายชั้น โดยการเปรียบเทียบการทรีตเมนต์ท่อนาโนคาร์บอนด้วยเทคนิคไมโครเวฟ และเทคนิคออกซิเจนพลาสมา ซึ่งการทรีตเมนต์ด้วยเทคนิคไมโครเวฟ นำท่อนาโนคาร์บอนไปให้ความร้อนที่อุณหภูมิ 500 องศาเซลเซียส หลังจากนั้นนำไปทรีตเมนต์ด้วยไมโครเวฟ โดยการใช้กำลังไฟฟ้า 650 วัตต์ ส่วนการทรีตเมนต์ด้วยออกซิเจนพลาสมา นำท่อนาโนคาร์บอนไปออกซิเจนพลาสมา ที่ความถี่อาร์เอฟ 13.56 เมกกะเฮิร์ต กำลังไฟฟ้า 18 วัตต์ พบว่าท่อนาโนคาร์บอนที่ผ่านการทรีตเมนต์ด้วยเทคนิคไมโครเวฟและเทคนิคออกซิเจนพลาสมา แสดงหมู่ฟังก์ชันของออกซิเจน และมีความไม่สมบรูณ์บริเวณผนังของท่อนาโนคาร์บอนมากขึ้นทำให้มีสมบัติความชอบน้ำ ซึ่งการทรีตเมนต์ด้วยเทคนิคออกซิเจนพลาสมาแสดงสมบัติการชอบน้ำมากที่สุดเมื่อเปรียบเทียบการทรีตเมนต์ด้วยเทคนิคไมโครเวฟ จากนั้นนำท่อนาโนคาร์บอนที่ผ่านการทรีตเมนต์ไปประดิษฐ์ขั้วของตัวเก็บประจุยิ่งยวดและทดสอบสมบัติไฟฟ้าเคมีแบบสามขั้วโดยใช้โซเดียมซัลเฟตเป็นอิเล็กโทรไลต์โดยมีช่วงความต่างศักย์ไฟฟ้า 0.8 โวลต์ พบว่าท่อนาโนคาร์บอนที่ผ่านการทรีตเมนต์ด้วยเทคนิคออกซิเจนพลาสมา มีค่าความจุไฟฟ้าจำเพาะสูงที่สุดคือ 104.62 ฟารัดต่อกรัม ค่าความหนาแน่นของพลังงาน 9.30 วัตต์ชั่วโมงต่อกิโลกรัมและค่าความหนาแน่นของกำลังไฟฟ้า 0.33 กิโลวัตต์ต่อกิโลกรัม ค่าความจุไฟฟ้าจำเพาะและค่าความหนาแน่นของ

พลังงานเพิ่มขึ้น 4.3 เท่าเมื่อเปรียบเทียบกับท่อนาโนคาร์บอนดั้งเดิม การเพิ่มขึ้นของค่าความจุไฟฟ้าจำเพาะอาจเกิดจากการที่มีหมู่ฟังก์ชันของออกซิเจนเพิ่มมากขึ้น ซึ่งการทรีตเมนต์ด้วยเทคนิคออกซิเจนพลาสมาเป็นวิธีการที่มีประสิทธิภาพและรวดเร็วสำหรับการเพิ่มหมู่ฟังก์ชันของท่อนาโนคาร์บอน งานวิจัยส่วนที่ 2 การสังเคราะห์วัสดุไฮบริดท่อนาโนคาร์บอนและแมงกานีสออกไซด์นาโนชีท ในงานวิจัยได้สังเคราะห์ขั้วไฟฟ้าทั้งหมด 2 ชั้น ได้แก่ ชั้นแรกชั้นท่อนาโนคาร์บอนที่ผ่านการทรีตเมนต์ด้วยเทคนิคออกซิเจนพลาสมาและชั้นที่สองชั้นฟิล์มบางแมงกานีสออกไซด์นาโนชีทด้วยวิธีการเคลือบด้วยไฟฟ้า พบว่าวัสดุไฮบริดท่อนาโนคาร์บอนและแมงกานีสออกไซด์นาโนชีทที่เวลา 15 นาที มีค่าความจุไฟฟ้าจำเพาะสูงที่สุดคือ 144.10 ฟารัดต่อกรัม ค่าความหนาแน่นของพลังงาน 12.80 วัตต์ชั่วโมงต่อกิโลกรัมและค่าความหนาแน่นของกำลังไฟฟ้า 0.28 กิโลวัตต์ต่อกิโลกรัมที่ช่วงความต่างศักย์ไฟฟ้า 0.8 โวลต์ ค่าความจุไฟฟ้าจำเพาะและค่าความหนาแน่นของพลังงานเพิ่มขึ้น 5.8 เท่าเมื่อเปรียบเทียบกับท่อนาโนคาร์บอนดั้งเดิม การเพิ่มขึ้นของค่าความจุไฟฟ้าจำเพาะเกิดจากการเพิ่มขึ้นของพื้นที่ผิวของขั้วไฟฟ้าจากวัสดุไฮบริดแมงกานีสออกไซด์นาโนชีทและท่อนาโนคาร์บอน และการเพิ่มขึ้นของปฏิกิริยาฟาราเดอิกจากแมงกานีสออกไซด์นาโนชีท งานวิจัยส่วนที่ 3 การประยุกต์ใช้งานเป็นตัวเก็บประจุยิ่งยวดแบบอสมมาตร โดยใช้วัสดุไฮบริดท่อนาโนคาร์บอนและแมงกานีสออกไซด์นาโนชีทเป็นขั้วไฟฟ้าขั้วบวกและท่อนาโนคาร์บอนที่ผ่านการทรีตเมนต์เป็นขั้วไฟฟ้าขั้วลบ จากนั้นทดสอบสมบัติไฟฟ้าเคมีแบบสองขั้วและใช้โซเดียมซัลเฟตเป็นอิเล็กโทรไลต์ที่ช่วงความต่างศักย์ไฟฟ้า 2.0 โวลต์ ตัวเก็บประจุยิ่งยวดแบบอสมมาตรมีค่าความจุจำเพาะสูงที่สุดคือ 66.97 ฟารัดต่อกรัม ค่าความหนาแน่นของพลังงาน 37.21 วัตต์ชั่วโมงต่อกิโลกรัมและค่าความหนาแน่นของกำลังไฟฟ้า 4.11 กิโลวัตต์ต่อกิโลกรัม ค่าความหนาแน่นของพลังงานเพิ่มขึ้น 17 เท่าเมื่อเปรียบเทียบกับท่อนาโนคาร์บอนดั้งเดิม ซึ่งโครงสร้างขั้วไฟฟ้าแบบอสมมาตรที่ออกแบบนี้ จะสามารถเพิ่มความหนาแน่นพลังงานของตัวเก็บประจุยิ่งยวดได้จากการเพิ่มขึ้นของช่วงความต่างศักย์ของขั้วไฟฟ้าที่วัสดุต่างกันและจากการเพิ่มขึ้นของค่าความจุจำเพาะของขั้ววัสดุไฮบริด นอกจากนี้ในงานวิจัยได้ศึกษาความเป็นไปได้ของการนำใบไม้มาเป็นวัสดุตั้งต้นของถ่านกัมมันต์และศึกษาสมบัติไฟฟ้าเคมี พบว่าถ่านกัมมันต์ที่สังเคราะห์จากใบมะละกอมีพื้นที่ผิวของขั้วไฟฟ้าสูง (2664 ตารางเมตรต่อกรัม) มีโครงสร้างที่มีรูพรุน (1.27 ลูกบาศก์เซนติเมตรต่อกรัม) มีการนำไฟฟ้าที่ดีและมีการเจือของไนโตรเจนและออกซิเจนเข้าไปในโครงข่ายคาร์บอน ซึ่งจากผลเหล่านี้สามารถสรุปได้ว่าถ่านกัมมันต์จากใบมะละกอสามารถนำมาเป็นวัสดุสำหรับขั้วไฟฟ้าของตัวเก็บประจุยิ่งยวดได้และมีค่าความจุไฟฟ้าจำเพาะ 68.49 ฟารัดต่อกรัม

คำสำคัญ : ท่อนาโนคาร์บอนแบบผนังหลายชั้น ถ่านกัมมันต์ แมงกานีสออกไซค์นาโนชีท ตัวเก็บประจุยิ่งยวดแบบอสมมาตร

Thesis Title	Synthesis of nanocarbon and manganese oxide nanosheet hybrid materials for asymmetric supercapacitor
Student	Miss Paweena Dulyaseree
Student ID	54670203
Degree	Doctor of Philosophy
Program	Nanoscience and Nanotechnology
Year	2017
Thesis advisor	Asst. Prof. Dr. Winadda Wongwiriyapan
Thesis Co-advisor	Dr. Wirat Jarernboon

ABSTRACT

This research studies on carbon nanotube (CNT) and manganese dioxide (MnO_2) nanosheet hybrid materials for asymmetric supercapacitor application. Two important parameters to improve energy density of supercapacitor are capacitance and voltage window. In this research, the capacitance of supercapacitor was increased by functionalization of multi-walled carbon nanotube (MWNT) (Part I) and synthesis of MnO_2 nanosheet and f-MWNT hybrid materials (MnO_2/f-MWNT) (Part II). Moreover, the voltage window of supercapacitor was increased by designing asymmetric supercapacitors (ASC) based on f-MWNT and MnO_2/f-MWNT (Part III). Firstly, functionalization of MWNT by microwave and oxygen plasma treatments were studied. The f-MWNT were treated by heating under air ambient at 500 ºC and then were treated by microwave at 650 W (m-MWNT) meanwhile another batch of MWNT were treated by oxygen plasma at an RF frequency of 13.56 MHz, power of 18 W (p-MWNT). It was found that the m- and p-MNWT exhibits the increasing of oxygen-containing functional groups, surface area, and wettability property. The p-MNWT shows the best hydrophilic property. 1 M Na_2SO_4 aqueous solution was used as an electrolyte at the voltage window of 0.8 V. It was found that p-MWNT achieved the best performance with a specific capacitance of 104.62 Fg^{-1}, an energy density of 9.30 $Whkg^{-1}$ and power density of 0.33 $kWkg^{-1}$. The p-MWNT shows the highest specific capacitance and energy density with the 4.3-fold increasing compared to that of the pristine-MWNT. The oxygen plasma treatment is an efficient and rapid method for functionalization of MWNTs. The second part of the thesis studies on the MnO_2 nanosheet and f-MWNT hybrid materials (MnO_2/f-MWNT) for supercapacitor application. The electrode consists of 2 layers; f-MWNT, and MnO_2 nanosheets. Supercapacitor performance based on these hybrid materials were optimized by varying synthesis times of MnO_2. The MnO_2/f-MWNT electrode prepared by 15-min-deposited MnO_2 nanosheet shows the highest specific capacitance of 144.10 Fg^{-1}, energy density of 12.80 $Whkg^{-1}$ and power density of 0.28 $kWkg^{-1}$ at the voltage window of 0.8 V. The specific capacitance and energy density of MnO_2/f-MWNT was increased 5.8-fold with compared to pristine-MWNT. The highest specific capacitance of 15 min-MnO_2/f-MWNT is due to the increase in effective surface area by the combination of MnO_2 nanosheet and the f-MWNT and the increase in Faradaic reaction by MnO_2 nanosheet. In the third part, asymmetric supercapacitor (ASC) based on f-MWNT and MnO_2/f-MWNT was studied. The MnO_2/f-MWNT were used as a positive electrode, assembled with the f-MWNT as a negative electrode. 1 M Na_2SO_4 was used an electrolyte at the voltage window of 2.0 V. The specific capacitance of ASC is 66.97 Fg^{-1} The ASC shows an energy density of 37.21 $Whkg^{-1}$ at a power density of 4.11 $kWkg^{-1}$, indicating both considerable energy density and excellent power capability. The energy density of ASC was increased 17-fold with compared to pristine-MWNT. The ASC is an effective approach to enhance the energy density by increasing the operation voltage by utilizing the different potential windows of the two electrodes, and by increasing the specific capacitance by using hybrid materials. In addition, the possibility to synthesize activated carbon from papaya leaves (PL) as a precursor and its electrochemical properties was studies. It was found that PL-derived activated carbon has the high specific surface area (2664 m^2g^{-1}), hierarchical porous structure (1.27 $cm^3\ g^{-1}$), good conductivity and heteroatom doping. The PL-derived activated carbon can be used as the electrode materials for supercapacitor application with a specific capacitance of 68.49 Fg^{-1}.

Keywords : Multi-walled carbon nanotube, Activated carbon, Manganese dioxide nanosheet, Asymmetric supercapacitor

ACKNOWLEDGEMENTS

First of all, I would like to express my deep and sincere gratitude to my advisor, Asst. Prof. Dr. Winadda Wongwiriyapan (College of Nanotechnology, King Mongkut's Institute of Technology Ladkrabang, KMITL) and co-advisor, Dr. Wirat Jarernboon (Khon Kaen University) for their encouragement, helpful suggestions, remarkable patience, and kind support.

I am deeply grateful to Asst. Prof. Dr. Benchapol Tunhoo, Dr. Mayuree Phonyium (College of Nanotechnology, KMITL), Dr. Annop Klamchuen (National Nanotechnology Center, NANOTEC), Asst. Prof. Dr. Masatsugu Fujishige, and Assoc. Prof. Dr. Kenji Takeuchi (Shinshu University) for their comments and suggestions on this dissertation.

I would like to acknowledge the financial support from the Strategic Scholarships Fellowships Frontier Research Networks (Specific for Southern region) from the Office of the Higher Education Commission (OHEC).

I would like to thank all the colleagues and friends, especially those who are the members of Nanocarbon Materials Research Laboratory, College of Nanotechnology, KMITL for their supports and kindnesses.

Finally, this dissertation is dedicated to my parent, my husband, my daughter, my brother and sister for their supports.

Paweena Dulyaseree

CONTENTS

CONTENTS (Cont.)

Page

CONTENTS (Cont.)

Page

CONTENTS (Cont.)

Page

LIST OF TABLES

Table Page

LIST OF FIGURES

Figure Page

LIST OF FIGURES (Cont.)

Figure Page

LIST OF FIGURES (Cont.)

CHAPTER 1

INTRODUCTION

1.1 Significance of Research

Nowadays, the important issue among energy is interested all the world. Global warming and limited resources of fossil fuels is on demand to move towards renewable resources. Currently, there are discovered in renewable production from the sun, wind and water, as well as the improvement of electronic devices and hybrid electronic vehicles. The tremendous growth of portable electronic device and hybrid electronic vehicles has been the urgent and increasing demand for environmentally friendly high-power and high-energy resources. Supercapacitor have come to called ultracapacitor or electrochemical capacitor (EC). Supercapacitor is a combine between high power capability and good specific energy, bridging the gap between batteries and conventional capacitors for energy storage of electrical device. Supercapacitor exhibit a higher power density than battery, a higher energy density than conventional capacitor, very fast charging, and long cycle life [1–5]. Supercapacitor are principally based on two types of capacitive behavior: (1) electrical double-layer capacitor (EDLC) by an electrostatic charge between the electrode/electrolyte interface, and (2) pseudocapacitors that is developed from Faradaic reaction process [3]. For supercapacitor, the carbon materials are the most generally used as electrode materials for EDLC because of high surface area, good conductivity, and good electrolyte accessibility [6]. In the case of pseudocapacitors, transition metal oxides and conducting polymers are used as materials for supercapacitor [7]. The new trend in supercapacitor development is asymmetric supercapacitor (ASC), ASC combining EDLC anode (carbon materials) and pseudocapacitor cathode (transition metal oxides materials) present capability to improve the energy density, that is ASC depending on the use of two electrodes as different voltage to increase the operating voltage to see some effect on the energy density [8].

Recently, to apply supercapacitor to practical application, supercapacitor with a high energy density is required. Since the energy density is proportional to capacitance and a square of cell voltage. Therefore, there have two parts in increasing energy density. First, to increase capacitance must have the discovery of advanced electrode materials, and use of an aqueous electrolyte. Therefore, substantial effort have been expended to increasing the energy density of electrode materials through the discovery of electrode materials by, for example, high surface area of electrode materials [9–13], or functionalized surface as well as the increased accessibility of the electrolytes to electroactive species [14–18], or hybrid EDLC and pseudocapacitor; hybrid materials try to take advantage of the relative advantage and appease the relative disadvantage of EDLC and pseudocapacitor to realize better performance characteristics. The combination of Faradaic and non-Faradaic processes to store charge, hybrid materials have succeed energy density and power density greater than EDLC [19–22]. In the part of an aqueous electrolyte, such as KOH, H_2SO_4, and Na_2SO_4 aqueous electrolytes have the advantage of high ionic conductivity (up to ~1 Scm^{-1}), low cost, and wide acceptance (~1.2 V, that is lower than that organic electrolyte) [8,23–25]. Second, to increase of cell voltage, the most intensive procedures include the use of organic electrolyte or ionic liquids electrolyte and development of asymmetric supercapacitor (ASC). In the electrolyte part, there has been a trend to used organic or ionic liquids electrolyte in order to achieve higher operational voltage and greater specific energy [10,24,26,27]. And the ASC part, the ASC is fabricated by combining a pseudocapacitors (as the energy source) and an EDLC (as the power source) in a cell. The main requirements of ASC are complementary electrochemical operating window, which increasing the operation voltage much be the enhanced to energy density while maintain a high-power density [24,28–31].

In this study, to enhance energy density, asymmetric supercapacitor based on functionalized multi-walled carbon nanotube (f-MWNT) and hybrid f-MWNT with manganese dioxide (MnO_2) nanosheet materials was proposed. The research consists of 3 parts; (1) functionalization of MWNT (f-MWNT) by oxygen plasma treatment, (2) the synthesis of MnO_2 nanosheet and f-MWNT hybrid materials (MnO_2/f-MWNT), and (3) asymmetric supercapacitor (ASC) based on f-MWNT and MnO_2/f-MWNT.

1.2 Objective of the study

1.2.1 To improve the energy density of supercapacitor by increasing its capacitance and voltage window

1.2.1.1 To increase capacitance of supercapacitor by functionalization of multi-walled carbon nanotube (f-MWNT) using microwave or oxygen plasma treatment

1.2.1.2 To increase capacitance of supercapacitor by using hybrid materials based on manganese dioxide nanosheet and functionalized multi-walled carbon nanotube (MnO_2/f-MWNT)

1.2.1.3 To increase voltage window of supercapacitor by designing asymmetric supercapacitor based on f-MWNT and MnO_2/f-MWNT

1.2.2 To synthesize activated carbon from green leaves of papaya as a precursor and study its electrochemical properties

1.3 Scope of the study

1.3.1 Preparation of functionalization of MWNT (f-MWNT) by microwave and oxygen plasma treatments

1.3.2 Preparation of hybrid materials based on MnO_2 nanosheet and f-MWNT

1.3.3 Preparation of asymmetric supercapacitor (ASC) cell assembly

1.3.4 Synthesis of activated carbon from green leaves of papaya

1.3.5 Measurement of electrochemical properties of f-MWNT, MnO_2 nanosheet/ f-MWNT hybrid materials, ASCs and activated carbon

1.4 Expected results

1.4.1 Successfully fabricate hybrid materials based on functionalized MWNT (f-MWNT) and MnO_2 nanosheet.

1.4.2 Successfully fabricate asymmetric supercapacitor based on f-MWNT and MnO_2/f-MWNT.

1.4.3 Improve the performance of supercapacitor based on hybrid materials and asymmetric supercapacitor

1.4.4 Improve to increase energy density by an increase in total capacitance and an increase in cell voltage

1.4.5 Successfully synthesize activated carbon from green leaves of papaya

CHAPTER 2

LITERATURE REVIEW

2.1 Properties of supercapacitor

Electrochemical capacitor (EC), also called supercapacitor or ultracapacitor, is one of energy storage device and its name describes the fundamental charge storage principle. Supercapacitor has very high capacitance compared with the conventional capacitor, while the energy density of the supercapacitor is lower compared with battery. Therefore, supercapacitor has the potential to bridge the gap between conventional capacitor and battery as shown in the Ragone plot in Fig. 2.1. In term of energy density and power density, supercapacitor shows high power density, but lower energy density compared with battery. In additional, from the charge-discharge process, the supercapacitor can be fully charge in second to minutes compared to the battery that requires to hours in charging. Supercapacitor has longer life time (> 10 years) than battery (approximately 3 years) but shorter life time than conventional capacitor (>> 10 years). Comparison of typical capacitor and battery characteristics is summarized in Table 2.1 [32].

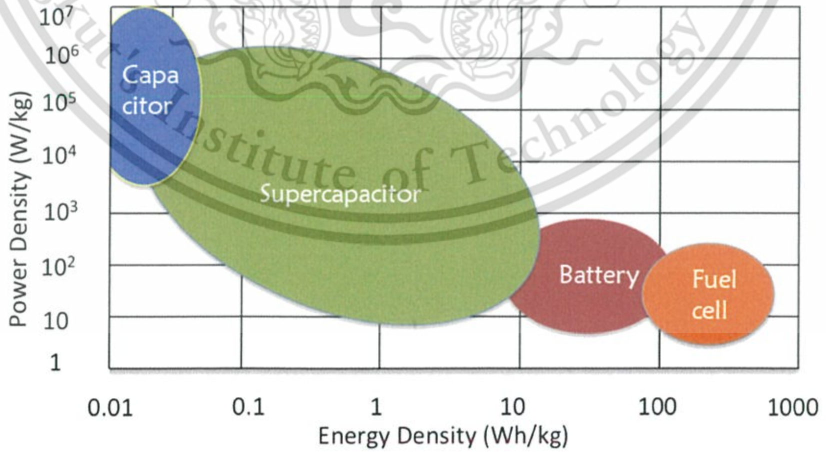

Figure 2.1 Ragone plot showing the specific power against specific energy for various electrical energy storage systems [33]

Table 2.1 Comparison of typical capacitor and battery characteristics

Characteristics	Capacitor	Battery	Supercapacitor
Storage mechanism	Electrostatic	Chemical	Electrostatic
Energy density ($Whkg^{-1}$)	<0.1	~ 20-150	1-100
Power density (Wkg^{-1})	>>10000	<10000	500-1000
Discharge time	10^{-6}-10^{-3} s	0.3-3 h	Second to minutes
Cycle life	>> 10 yr	~ 3 yr	>10 yr
V_{max}	High	Low	<3
Charge storage	Between charged plates	Entire electrode	Electrode-electrolyte interface
Determined by	- Geometric area of the electrodes - Dielectric	- Active mass - Thermodynamics	- Electrode (microstructure) - Surface area - Electrolyte

2.2 Structure of supercapacitor

The structure of supercapacitor plays as important to an enhancement of performance. The structure of supercapacitor consists of three important parts; the electrode, the electrolyte, and the separator as shown in Fig. 2.2. The electrode coated with carbon materials or metal oxide, the electrolyte contains free mobile ions and the separator prevents electrodes from shorting together. These compositions can be improved to enhance supercapacitor performance.

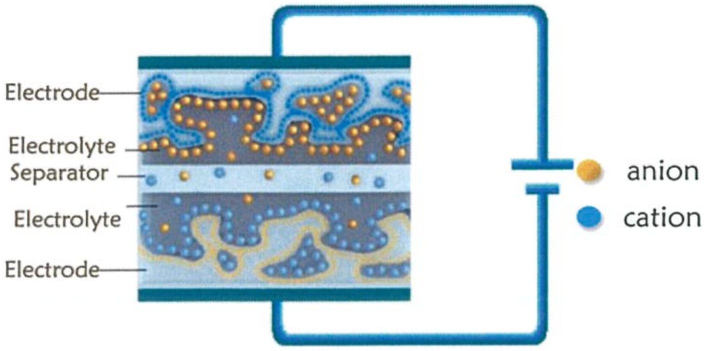

Figure 2.2 Schematic view of structure of supercapacitor [34]

2.2.1 Electrode materials

An electrode used in supercapacitors is constructed with the symmetric electrode or with the asymmetric electrodes such as positive and negative electrode of the same or different materials, respectively. The properties of electrode materials required for supercapacitor are as follows:

- High surface area (1000-2000 m^{2}g^{-1}), necessity to development the electric double layer
- Controlled pore size distribution to develop increased capacitance
- Cyclic stability (>10^5) indicating long cycle life
- Resistance to irreversible redox reactions with the surface of electrode that is significant of supercapacitor performance
- Good chemical stability
- Surface wettability of the electrode, to improve the accessibility of the electrolyte ions into the electrode materials

The properties of electrode materials also depend on type of supercapacitor (electric double layer capacitor (EDLC) or pseudocapacitance).

2.2.2 Electrolyte

An electrolyte plays an important role in development of supercapacitor, i.e. the electric double layer in DELC and for the reversible adsorption and intercalation redox process in pseudocapacitance. Currently, the aim of electrolyte has been developed to high conductivity and stable electrolyte for a wider voltage. Three types of electrolytes are currently employed in supercapacitor: (i) aqueous electrolyte, (ii) organic electrolyte and (iii) ionic liquid. The requirements for an electrolyte in supercapacitor include wide voltage window, high electrochemical stability, high ionic conductivity, and low toxicity. Comparison of typical electrolyte properties is summarized in Table 2.2 [35].

Table 2.2 Comparison of typical electrolyte properties

Characteristics	Electrolyte		
	Aqueous	Organic	Ionic liquids (ILs)
Voltage window (V)	≤ 1	2.5-2.7	3-6
Ionic conductivity ($mScm^{-1}$)	High	Low	High
Cost	Low	Moderate/High	Very high
Assembly environment	Air	Inert atmosphere	Inert atmosphere
Toxicity	Low	Moderate/High	Low

2.2.2.1 Aqueous Electrolyte

The advantages of aqueous electrolyte have attracted much attention due to high ionic conductivity (0.5-1 Scm^{-1}), low cost and low toxicity. However, the disadvantage of aqueous electrolyte is their relatively narrow voltage window, which is limited by the electrochemical breakdown of water to ~1.23 V [36]. An operating range of 0.8-1.0 V is employed to avoid the loss of the electrolyte, introduction of oxygen or hydrogen that leads to cell rupturing, and additional losses in current from competing Faradaic reaction. Furthermore, the careful selection of packaging of the current collector is also required to avoid corrosion in the acidic or alkali electrolyte.

2.2.2.2 Organic Electrolyte

Organic electrolytes are used in commercial supercapacitor owing to their operating voltage above 2 V (2.5-2.7 V). Organic electrolytes have low conductivity (0.01-0.05 Scm^{-1}), which leads to increase in resistivity (20-60 Ωcm). However, its toxicity and flammability of organic electrolyte require more stringent and costly preparation processes. Besides, organic electrolyte needs the purification process to remove any residual water content, which can lead to the corrosion of current collectors at high voltage. Efforts have been currently done to find a replacement nontoxic organic electrolyte yielding good ion conductivity.

2.2.2.3 Ionic liquid (IL) electrolyte

Ionic liquid (IL) exists as solvent-free molten salts at or below room temperature [36], possesses high thermal and electrochemical stability above of 3 V (3-6 V). Moreover, the advantages of using IL include nontoxic solvent and nonflammable, making them attractive choices to organic solvents. The ionic conductivity of these IL at room temperature is very low, so they are largely used at higher temperature [37]. The disadvantage of IL includes relatively high viscosities and much lower ionic conductivities than aqueous electrolytes, high cost, and limiting the larger scale production. In addition, IL is hygroscopic, which require being managed in stringent and controlled processes.

2.2.3 Separator

The separators have been selected by thin, nonconducting separator, which is minimizing the electrolyte resistance contribution. Separator made of polymer or paper is used with aqueous and organic electrolytes. Property of separator is good transport, which can be the electrolyte ion accessing into the electrode materials and subsequently enhancement of their capacitive characteristics.

2.2.4 Working of supercapacitor

The working of supercapacitor consists of two parts; before and after bias of voltage. Before charging, in electrolyte, positive and negative ion are uniformly dispersed and there is not electric field at the electrode surface. When the voltage is applied, the ions are attracted to the electrode with the opposite charge. Thus, energy is stored as a charge separation in double layer formed at the interface between the surface of electrode materials and the electrolyte. The schematic of working of supercapacitor is shown in Fig. 2.3.

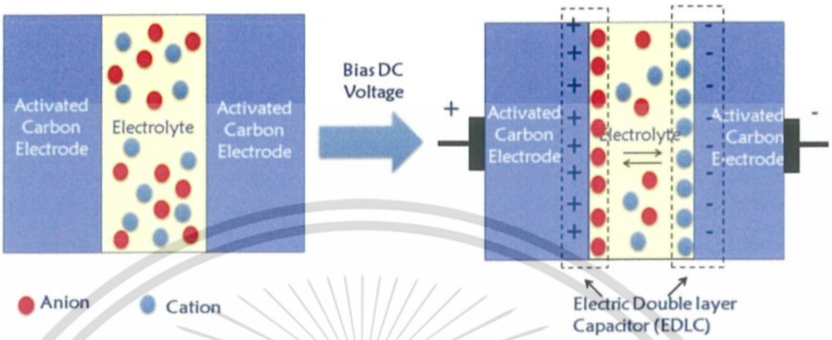

Figure 2.3 Schematic view of working of supercapacitor

2.3 Type of supercapacitor

Supercapacitor can be divided by the charge mechanism of active material used for electrode structure. Primarily, the development of supercapacitor was focused on the electrical double layer capacitor (EDLC) that developments in porous carbon materials. After that, different form of supercapacitor can be divided as a pseudocapacitive charge mechanism and asymmetric supercapacitor (ASC) form. The EDLC, pseudocapacitor, and ASC have fundamental differences in the electrochemical processes appearing for design of structure and charge storage. Main characteristics of each types of supercapacitor are summarized in Table 2.3 [38]. The following section describes each type of supercapacitor in detail.

Table 2.3 Main characteristics of three types of supercapacitor

Type	Mechanism	Materials	Advantage	Disadvantage
EDLC	Charge separation at the electrode-electrolyte interface	Carbon materials	High power density, Good cycling behavior	Low energy density, Low working voltage
Pseudo-capacitor	Reversible surface Faradic redox reaction	Transition metal oxide, Conducting polymer	High capacitance, High energy density	Poor cycling, Low working voltage
Asymmetric supercapacitor (ASC)	Redox reaction for one electrode and electric double-layer absorption/desorption for others electrode	Porous carbon, Graphene, Metal oxide, Conductive polymer	Relative high energy and power densities, Good cycling	Almost every performance is at the intermediate level

2.3.1 Electrical double layer capacitor (EDLC)

2.3.1.1 Mechanism of EDLC

EDLC is the most common supercapacitor that has the same mechanism as a traditional capacitor, namely, by means of charge separation at the electrode-electrolyte interface. Carbon materials are the most commonly used electrode material for EDLC. Activated carbon (AC) is the main carbon material used in commercial owing to cheapness, widely available locally and ready availability. Currently, the development of EDLC is widely focused on designing new electrode materials such as carbon nanotube (CNT), graphene and mesoporous or hierarchical templated carbon. The electrode material is selected to improve the energy storage and charge rate capacity of EDLC. EDLC can store considerably more energy than a conventional capacitor owing to the following:

i. High surface area of EDLC to increase number of charge at the electrode-electrolyte interface
ii. High electrical conductivity

iii. Distribution of pores for controlled size, normally, the size of pore materials was selected to match with the ion size of electrolyte.

iv. Good wettability of electrolyte to improve the accessibility of the electrolyte ion into the electrode materials, which therefore supports the effective development of capacitive charge

v. A thin thickness at the electrode-electrolyte interface as so-called electrical double layer

The structure of EDLC is similar to battery that there are two electrodes immersed in an electrolyte, with a separator prevents electrodes from shorting together as shown in Fig. 2.4.

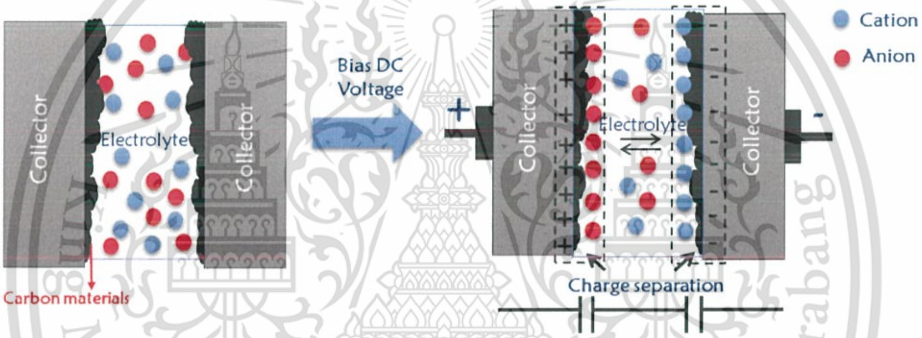

Figure 2.4 Schematic view of EDLCs construction

2.3.1.2 Electrode materials for EDLC

The properties of carbon materials used as electrode are summarized in Table 2.4 [35].

Table 2.4 Properties of carbon materials used as electrode in aqueous electrolyte

Electrode material	Surface area (m^2g^{-1})	Specific capacitance (Fg^{-1})
Activated carbon	1000-3000	200-400
Carbon nanotubes (CNT)	120-500	20-180
Graphene	2000-3000	100-200
Carbon black	250-2000	<300

(1) Activated carbon (AC)

Activated carbon (AC) has been the most commonly used electrode materials for EDLC due to its high specific surface area (SSA) in the range of 1000-2000 m^2g^{-1}, moderate cost, excellent chemical and thermal stability. ACs are synthesized from various of carbon-rich organic precursors such as shells, wood, leaves [39–43] as to increase the pore volume and high surface area that is the key for enhancement of supercapacitor performance. The porous structure of activated carbon composes of different size micropore (<2 nm), mesopores (2-50 nm), and macropores (>50 nm) as seen in Fig. 2.5.

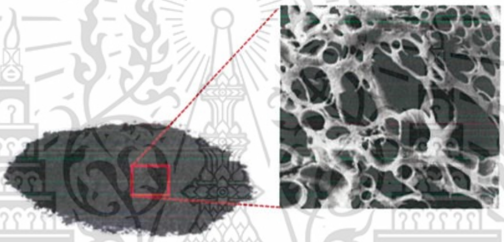

Figure 2.5 The sample of activated carbon [44]

(2) Carbon nanotube (CNT)

Carbon nanotube (CNT) possesses specified properties that are advantageous in its use as an EDLCs electrode material. CNT structure can be divided into two types; multi-walled carbon nanotube (MWNT) and single-walled carbon nanotube (SWNT) as shown the structure in Fig. 2.6. CNT has excellent properties such as high electrical conductivity, light weight, unique pore structure, thermal stability and suitable mechanical. However, the specific capacitance (SC) of CNT is still low due to the limitation of their surface area (less than 600 m^2g^{-1}) [45,46]. CNT electrode material has a lower resistance than AC because of the electrolyte ions can diffuse more easily into the mesoporous network at the surface of electrode. In addition, CNT can be grown directly onto the current collectors that could help reduce resistance allows higher power densities [15,47].

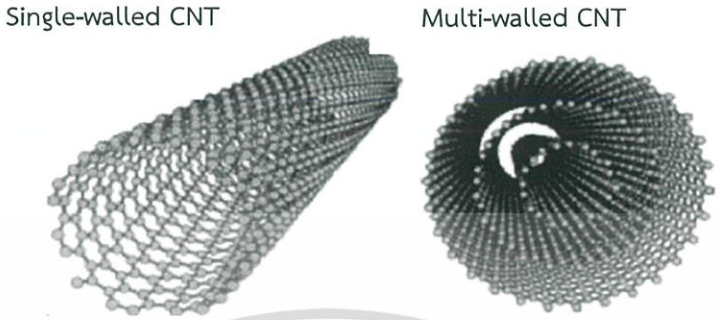

Figure 2.6 The structure of SWNT and MWNT [48]

(3) Graphene

Graphene is a single-layer two-dimensional (2D) carbon atoms as shown in Fig. 2.7 with a high surface area (2630 m^2g^{-1}), high electrical, thermal conductivity, mechanical strength, and good chemical stability. This material shows higher storage device than other carbon materials such as a high specific capacitance of ~100-200 Fg^{-1}, energy density of 28.5 $Whkg^{-1}$, and power density of 10 $kWkg^{-1}$ in aqueous electrolyte [49] owing to high surface area and excellent electrochemical performance.

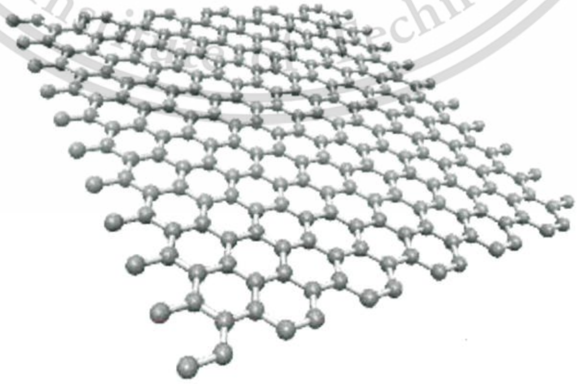

Figure 2.7 The structure of graphene [50]

2.3.2 Pseudocapacitor

2.3.2.1 Mechanism of pseudocapacitor

Pseudocapacitor is originally Faradaic oxidation/reduction reaction at specific potential during charging and discharging due to thermodynamic process. Depending on the material design and structure, the charge mechanism appearing between the electrode-electrolyte interface can also involve adsorption or intercalation of the electrolyte. The advantage of pseudocapacitor is the high energy density and high capacitance (10-100 times of the EDLC capacitance) due to the electron transfer reactions during charging, which contrast the electrostatic process (no Faradaic reaction) [7]. The most commonly investigated classes of pseudocapacitive materials are the transition metal oxide, e.g. MnO_2, NiO, RuO_2 and Co_3O_4 and conducting polymer, e.g. PPy, Polythiophene, and polyaniline (PANi).

2.3.2.2 Electrode materials for pseudocapacitor

(1) Transition metal oxides

Transition metals oxide has a number of properties making suitable for use as pseudocapacitors such as ruthenium dioxide (RuO_2), iron (Fe_3O_4), vanadium pentoxide (V_2O_5), tin dioxide (SnO_2) and manganese dioxide (MnO_2) [51–53].

In the case of MnO_2 material, MnO_2 has attracted significant interest as electrode material for supercapacitor due to its high theoretical specific capacitance (1000 Fg^{-1}), low cost, and environmentally friendly nature. Currently, two mechanisms were proposed to explain the MnO_2 charge storage behavior, which involves the Faradaic reactions occurring on the surface and in the bulk of the electrode [54]:

The first mechanism in MnO_2 mainly occurs via the insertion and intercalation in the bulk of proton:

$$(MnO_2)_{surface} + H^+ + e^- \leftrightarrow (MnOOH)_{surface} \tag{2.1}$$

The second mechanism in MnO_2 also exhibits pseudocapacitance via surface adsorption of electrolyte cation (C^+= H^+, Li^+, Na^+ and K^+, etc.,), depending on the electrolyte used, according to

$$(MnO_2)_{surface} + C^+ + e^- \leftrightarrow (MnOOC)_{surface} \qquad (2.2)$$

Noticeably, both the proposed charge storage mechanisms involve a redox reaction between the III and IV oxidation states of manganese (Mn).

In the past few years, various MnO_2 with different crystalline structure (amorphous, α-, β-, γ-,δ-MnO_2) have been investigated. Pore size and structure remain key factors in all these materials, which the large pore sizes are required to provide an accessible high surface area and excellent ion mobility, both of which are principle features for high capacitance.

(2) Conducting polymer

Conducting polymers have stimulated great interest due to their rapid and reversible redox reactions such as polyaniline (PANI), polythiophene (PTh), polypyrrole (PPy), etc. [1]. The advantages of conducting polymer include relatively high voltage window, and high-doping rate during charge-discharge process. However, high resistance and low stability limit the wide application. Especially, swelling and shrinkage may occur during charge-discharge processes, leading to mechanical degradation of the electrode and fading of capacitive performance. Fabricating composite electrode materials to improve the stability become the new development direction. For example, a high-performance polyaniline electrode has been prepared by electrochemical deposition on a porous carbon, showing the advancement of high-specific capacitance, excellent rate capability, and good cycling stability.

2.3.3 Asymmetric supercapacitor (ASC)

2.3.2.1 Principles for the asymmetric supercapacitor design

EDLC, symmetric supercapacitor based on aqueous electrolyte has a drawback about a limitation of the working voltage window (~1.2 V). Oxygen or hydrogen gas evolution due to water decomposition according to

$$2H_2O \rightarrow O_2 + 4H^+ + 4e^- \quad (E^{o}_{cell} = 1.23\ \text{V vs SHE}) \qquad (2.3)$$

However, one of the most critical aspects in the development of supercapacitor is to increase their working voltage window for energy density enhancement. The working voltage of supercapacitor depends on the electrolyte solvent used. Normally, working voltage is around 1.0 V for an aqueous-based electrolyte, 2.5-2.7 V for an organic-based electrolyte and 3.0-6.0 V for an ionic liquid electrolyte. Organic electrolyte has higher cell voltage than aqueous electrolyte, but organic electrolyte is lower ionic conductivity and higher toxic than aqueous electrolyte. Consequently, most efforts have done to increase voltage of supercapacitor based on aqueous electrolyte by designing asymmetric supercapacitor. Different strategies have been developed to increase the working voltage in the aqueous system. One of these is to build the asymmetrical supercapacitor using hybrid capacitor, asymmetric in material capacitor and asymmetric in mass capacitor. The different materials as the positive and negative electrode have been the most commonly used to design asymmetric supercapacitor. The asymmetric supercapacitor with different materials allows the combination of a pseudocapacitor and a EDLC electrodes in one device. This combination allows taking advantage of the high capacitances and high energy density of pseudocapacitor, while the operational voltage window and capacitance is enhanced by the proper selection of a porous carbon (EDLC) material. Besides, the storage mechanism of asymmetric supercapacitor is combined between electrostatic mechanism from EDLC and chemical mechanism from pseudocapacitor as shown in Fig. 2.8, which increases energy density.

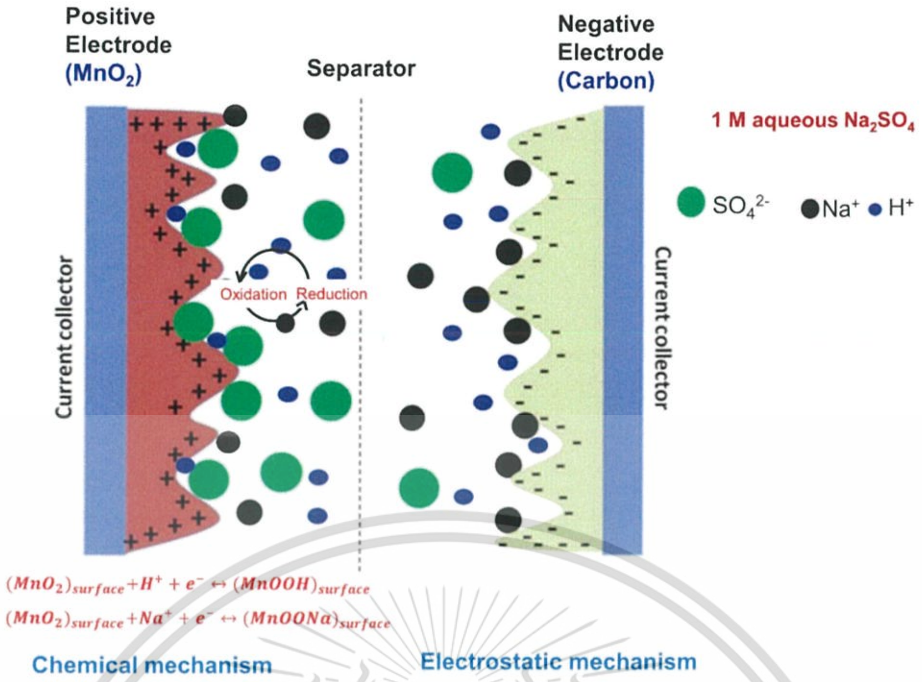

Figure 2.8 Schematic view of storage mechanism of asymmetric supercapacitor

Electrode materials for asymmetric supercapacitor was selected by, (i) EDLC base on carbon nanomaterials, such as activated carbon, carbon nanotube and grapheme have been explored as the electrode materials in EDLC due to high specific surface area and good conductivity properties. (ii) pseudocapacitor base on metal oxide, such as ruthenium oxide (RuO_2), manganese oxide (MnO_2), cobalt oxide (CoO_2) and molybdenum oxide (MoO_2). High specific capacitance and better cycling stability are advantage of metal oxide.

The key factors required in the optimization and structure design of asymmetric supercapacitor to enhance energy density are as follows: (i) the optimal mass ratio for increasing specific capacitance of asymmetric supercapacitor and (ii) the working voltage window of an electrochemical cell. The both factors are required to enhance energy density as shown in equation (2.4)

$$E = \frac{1}{2}CV^2 \tag{2.4}$$

where C is a total capacitance, and V is a cell voltage.

Thus, the design of asymmetric supercapacitor to enhance energy density are required as follows:

(1) To have a charge-balance device, the desired mass ratio between positive and negative electrodes is estimated using the mass-balance relation given as:

$$Q^{+} = Q^{-} \tag{2.5}$$

$$m^{+}C^{+}\Delta V^{+} = m^{-}C^{-}\Delta V^{-} \tag{2.6}$$

$$\frac{m^{+}}{m^{-}} = \frac{C^{-}\Delta V^{-}}{C^{+}\Delta V^{+}} \tag{2.7}$$

where m^{+},m^{-} are the mass of active materials, C^{+},C^{-} are the capacitance at the same scan rate and ΔV^{+}, $\Delta V^{-}$are the potential range for positive and negative electrode material.

(2) The maximum operating voltage window is strongly governed by (a) difference in work functions (i.e., $\Phi_n - \Phi_p$) of electrode (from physical aspects) and (b) decomposition energy of the positive and negative electrodes (from electrochemical aspect). The maximum working potential of the both methods were calculated as follows:

a) The difference in work function, the operating voltage window of a device can be given as:

$$E = \left(\Phi_n - \Phi_p\right)\frac{qN_A}{F} + \Delta E_1 + \Delta E_2 \tag{2.8}$$

where Φ_n and Φ_p are the work functions [eV] for the negative and positive electrodes, while q, N_A and F represent electron charge (1.6x10^{-9} C), the Avogadro's number (6.022x10^{23}) and Faraday constant (96,500 C/mol). ΔE_1 and ΔE_2 are the electrode potentials for the positive and negative electrodes, respectively [55–58]. This is schematically explained by an energy band diagram as shown in Fig. 2.9.

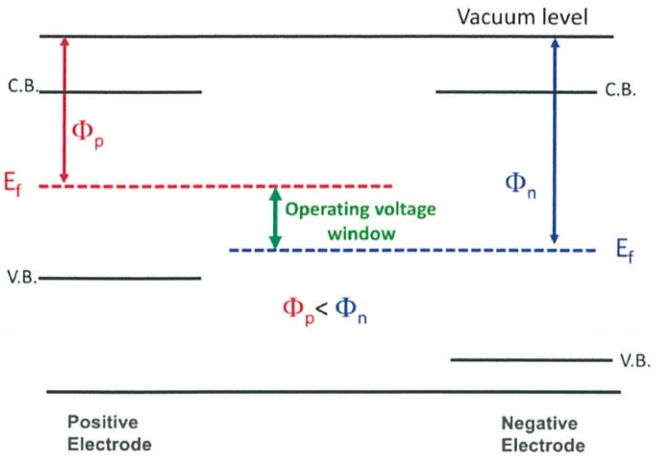

Figure 2.9 Energy band diagram to explain maximum achieved operating voltage window

b) The decomposition energy of the positive and negative electrodes, the decomposition energy can be given by standard reduction potentials (E^0_{cell}) as shown in this equation:

$$E^o_{cell} = E^o_{red(anode)} - E^o_{red(cathode)} \tag{2.9}$$

Thus, to obtain the maximum operation voltage window, the electrode materials should have more difference in work function (from physical aspects) or in standard reduction potentials (from electrochemical aspects).

2.3.2.2 The capacitance of asymmetric supercapacitor

Asymmetric supercapacitor is a connection in series between positive and negative electrodes. The total capacitance of asymmetric capacitance in series is given by the following equation:

$$\frac{1}{C_T} = \frac{1}{C_+} + \frac{1}{C_-} \tag{2.10}$$

$$C_T = \frac{C_+ \times C_-}{C_+ + C_-} \tag{2.11}$$

where C_T, C_+ and C_- are the capacitance of asymmetric supercapacitor, positive electrode and negative electrode, respectively.

In asymmetric device, the specific capacitance of the positive electrode is close to that of the negative electrode (i.e., $C_+ \approx C_- \approx C_e$), so that the capacitance of the completed cell becomes a half of the capacitance of each individual electrode; that is,

$$C_T = \frac{1}{2}\, C_e \tag{2.12}$$

Table 2.5 summarizes the electrochemical performance of the previous work on asymmetric supercapacitor (ASC). For these ASC, AC is commonly used as a typical negative electrode material, metal oxides are employed as the positive electrode material. The poor specific capacitance of AC and low stability of metal oxides/hydroxides would also greatly restrict the supercapacitor performance, resulting relatively low-energy density (10~30 Whkg^{-1}), power density, and cyclic stability. Recently, the discovery of new electrode materials and new synthesis method provide a promising approach to develop advanced supercapacitor with high performance.

Table 2.5 Electrochemical performance of the ASC based on conventional electrode materials

Electrode	Electrolyte	Capacitance (Fg^{-1})	Potential window (V)	Energy density (Whkg^{-1})	Power density (kW/kg^{-1})	Stability
$NaMnO_2$// AC	Na_2SO_4	38.9	1.9	19.5	0.13	97% (10,000 cycles)
$KMnO_2$// AC	K_2SO_4	57.7	1.8	25.3	0.14	98% (10,000 cycles)
NiO//AC	KOH	38	1.5	-	-	50% (1,000 cycles)
MnO_2-AC//AC	Na_2SO_4	33.2	2.0	18.2	10.1	92% (2,500 cycles)

2.4 Characterization techniques

2.4.1 Characterization of electrode materials

2.4.1.1 Transmission electron microscopy (TEM)

TEM is generally used to characterize the internal structure at the high resolution. Information about the crystal structure and morphology can be obtained by a combination of electrooptical imaging. The principle of TEM, the electrons are focused with electromagnetic lenses and the image is obtained on a fluorescent screen, or recorded on film or digital camera as shown a schematic diagram of TEM in Fig. 2.10a. In this work, TEM images were obtained by a JEOL JEM-2010 transmission electron microscope operated at an accelerated voltage at 200 kV with LaB_6 filament.

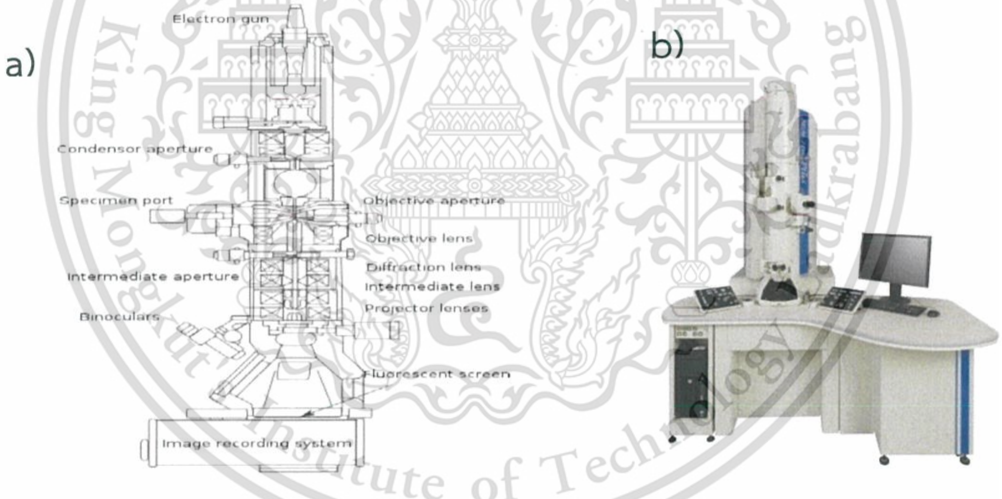

Figure 2.10 a) A schematic diagram of TEM and b) A photograph of JEOL JEM 2010 transmission electron microscope [59]

2.4.1.2 Scanning electron microscopy (SEM)

SEM is also used to characterize the morphology of sample that backscatter, or secondary electrons are scanned on the sample and detected to create image of the sample. A schematic diagram of SEM is shown in Fig. 2.11. In this work, SEM images were measured by a HITACHI S-4700 scanning electron microscope, which was operated at an acceleration voltage of 10 kV.

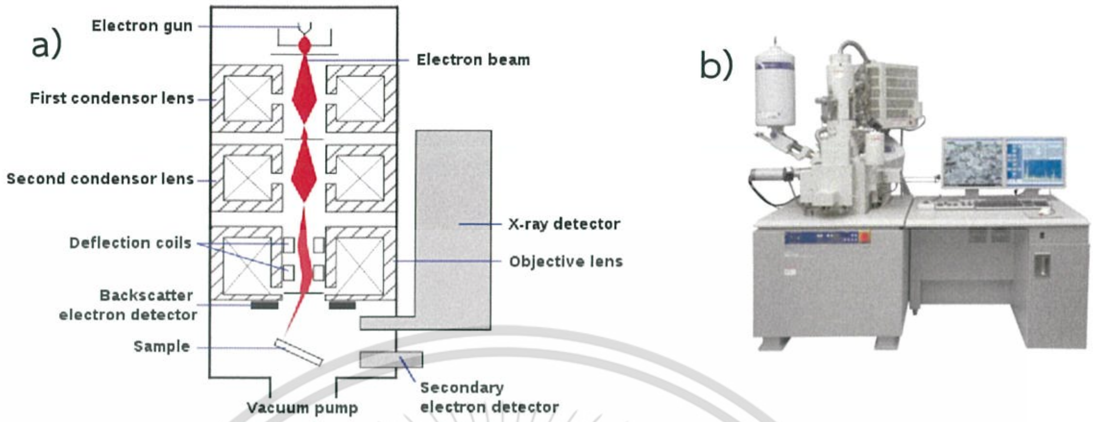

Figure 2.11 a) A schematic diagram of SEM and b) A photograph of HITACHI S-4700 scanning electron microscope [60]

2.4.1.3 Fourier transform infrared spectroscopy (FTIR)

A FTIR spectrometer records the interaction of infrared radiation (IR) with sample measuring the frequencies at which the sample absorbs the radiation and the intensities of the absorptions. The FTIR is a technique used to identify the chemical functional group, chemical bonding and chemical structure. Chemical functional groups are known as absorb some specific frequencies of light. The molecule is excited into a higher vibrational and rotational state as shown in a schematic diagram of FTIR in Fig. 2.12. Thus, the chemical structure can be determined from the frequencies recorded. In this work, FI-IR spectra were obtained by a Thermo Scientific Nicolet 6700 and collected in a wavelength range of 500-4000 cm^{-1}.

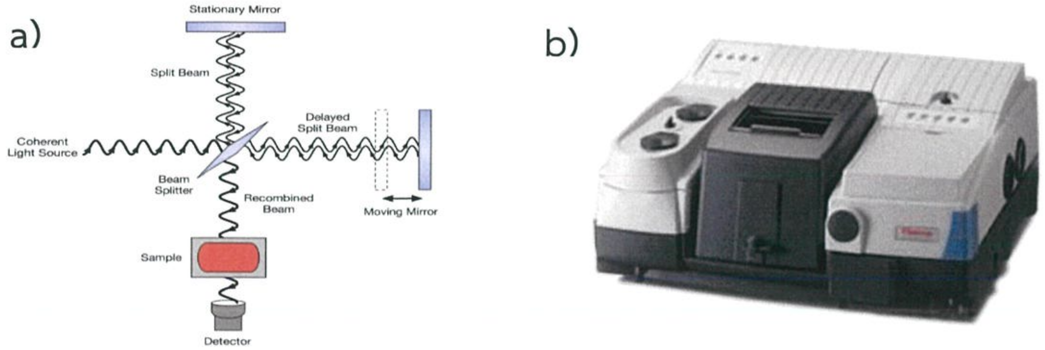

Figure 2.12 a) A schematic diagram of FT-IR and b) A photograph of Thermo Scientific Nicolet 6700 [61]

2.4.1.4 Raman spectroscopy

Raman spectroscopy is a technique used to study the carbon structure, purity, and crystallinity of CNT. The principle of Raman spectroscopy is a technique based on inelastic scattering, or Raman scattering of monochromatic light, usually from a laser in the visible near infrared. The laser light interacts with vibrating molecules in the system, resulting in the energy being shifted up or down. The shift in energy gives information about the vibrational modes in the system as shown in Fig. 2.13. In this work, the Raman spectra were carried out using a Thermo Scientific DXR smart Raman with a 532-nm laser source.

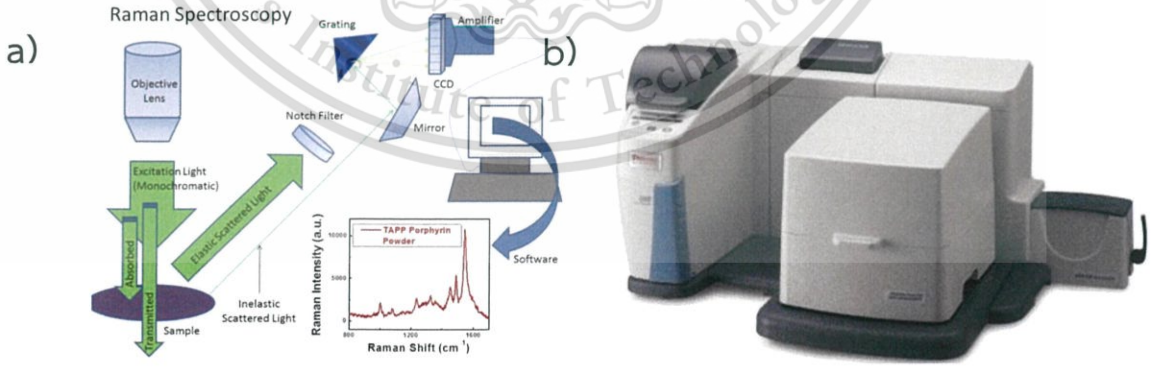

Figure 2.13 a) A schematic diagram of Raman spectroscopy and b) A photograph of Thermo Scientific DXR smart Raman [62]

2.4.1.5 X-ray diffraction (XRD)

X-ray diffraction (XRD) is a technique used to analyze the crystal structure of materials as shown in a schematic diagrams in Fig. 2.14 . The XRD analysis is based on constructive interference of monochromatic X-ray and a crystalline sample. X-rays are generated by cathode ray tube and accelerated to the sample. XRD result is produced the constructive interference of a monochromatic beam of X-rays diffracted at specific angle by lattice planes separated by the interplanar distance (d) which correspond to Bragg's law in equation (2.13).

$$n\lambda=2d\sin\theta \qquad (2.13)$$

where n is a positive integer

λ is a wavelength of incident X-ray

d is an interplanar distance of lattice

θ is a scattering angle

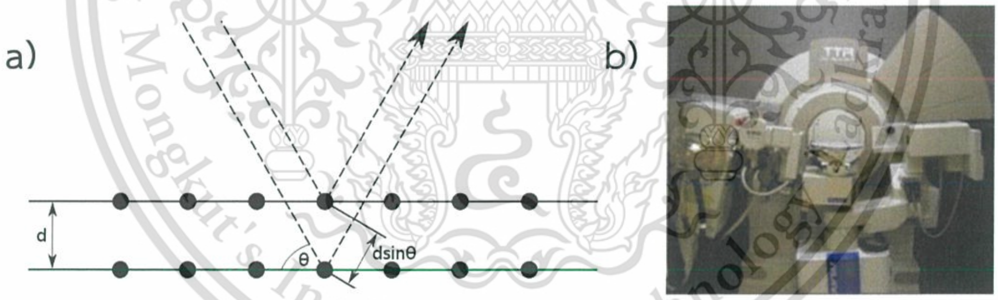

Figure 2.14 a) A schematic diagram of Raman spectroscopy and b) A photograph of Rigaku, TTRAX III [63]

2.4.1.6 Nitrogen-adsorption isotherm

Adsorption is the adhesion of atoms, ions or molecules from a nitrogen gas to a surface. The adsorption isotherm is used to describe the relationship between the amount of the adsorbate on the adsorbent as a function of its pressure (in case gas) at a constant temperature. Adsorption isotherms are classified according to international union of pure and applied chemistry (IUPAC)-recommendations in six different types as shown in Fig. 2.15a. In this work, the surface area and porosity were characterized by the N_2 adsorption isotherm using a micromeritics ASAP 2020 as shown in Fig. 2.15b.

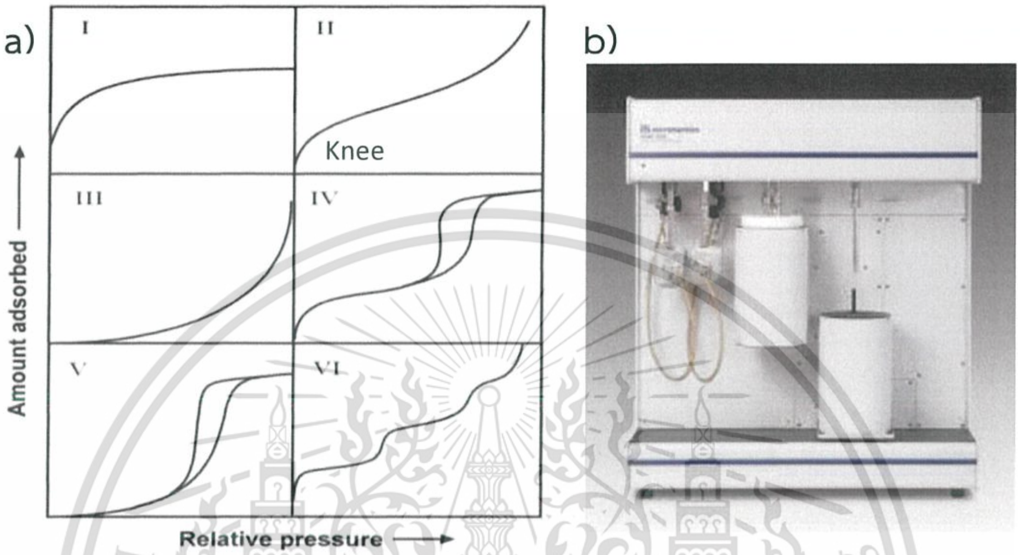

Figure 2.15 a) Types of gas adsorption isotherms and b) A photograph of micromeritics ASAP 2020 [64]

Type I isotherm is a monolayer adsorption of adsorbate at the adsorbent surface. This isotherm can be explained using Langmuir adsorption isotherm. Langmuir adsorption isotherm is derived based on the uniform surface and all the surface sites have the same activity for adsorption. Adsorbed molecules do not interaction with the other adsorbed molecules on the surface. Adsorption of all molecules occurs by the same mechanism and results in the same adsorbed structure and the extent of adsorption is less than one complete monolayer coverage.

$$A_g + S \leftrightarrows A_{ad} \qquad (2.14)$$

where A_g is unadsorbed gas molecule, S is unoccupied surface and A_{ad} is adsorbed gas molecule. This isotherm depicts a relationship between the number of active sites of the surface undergoing adsorption and pressure.

$$\theta = \frac{KP}{1+KP} \tag{2.15}$$

where θ is the number of sites of the surface which covered with gas molecule, P is pressure and K is the equilibrium constant for distribution of adsorbate between the surface and the gas phase. For example, the adsorption of oxygen on carbon black at -183 °C.

Type II isotherm is not saturation limit as type I isotherm. Type II isotherm exhibits an indefinitely multi-layer formation after completion of the monolayer. This isotherm can be explained using Brunauer, Emmett and Teller (BET) isotherm. BET adsorption isotherm is based on the multilayer formation. At the low pressure, molecules start to adsorb onto the surface according to Langmuir adsorption isotherm. As the pressure is increased, next molecules will adsorb to preabsorbed molecules, resulting in a multilayer formation.

$$\frac{P}{V(P_0-P)} = \frac{1}{V_m C} + \frac{(C-1)P}{V_m C P_0} \tag{2.16}$$

where V is volume of adsorbed vapor at standard temperature and pressure (STP), V_m is monolayer capacity at STP, P is partial pressure of the adsorbate and P_0 is the saturation vapor pressure of the adsorbate, C is BET constant. For example, the adsorption of water on carbon black at 30 °C is type II isotherm.

Type III isotherm is obtained when the amount of gas adsorbed increases without limit as its relative saturation approaches unity. For example, bromine is adsorbed on silica gel at 20 °C.

Type IV isotherm, at lower pressure region is quite similar to type II isotherm which involve the formation of monolayer followed by multilayer. The saturation reaches at a pressure below the saturation vapor pressure. This type of isotherm is obtained by the adsorption of benzene on silica gel at 500 °C.

Type V isotherm is similar variation of type III and this can be attributed to relatively weak adsorbent-adsorbate interactions. For example, the water vapor is adsorbed on charcoal at 1000 °C.

Type VI isotherm is representation of layer-by-layer adsorption on a highly uniform surface. For example, the adsorption of argon on graphitized carbon blacks at low temperature.

2.4.1.7 Contact angle

Contact angle is a technique used to study on the wettability properties. Wettability properties can be measured from contact angle of wetting interact (degree). The contact angle (<90°, small contact angle) correspons to the best wettability and (>90°, large contact angle) indicates low wettability as shown in schematic diagram of contact angle drops on surface in Fig. 2.16a. In this work, the contact angles were carried out using a Dataphysics OCA 40 as shown in Fig. 2.16b.

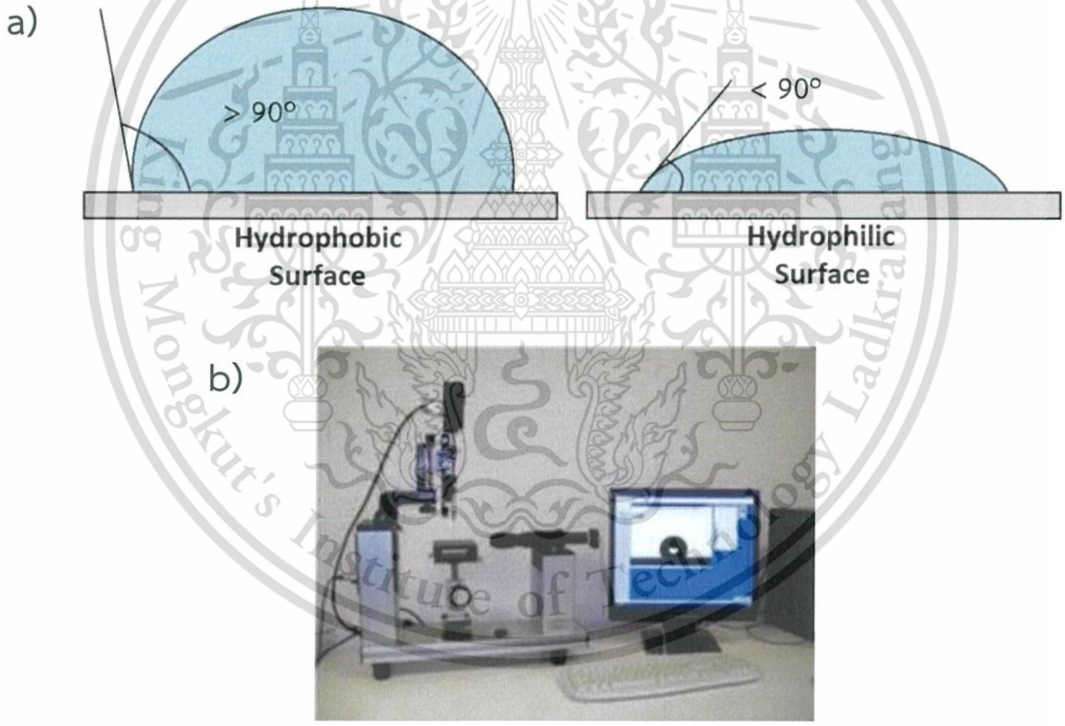

Figure 2.16 a) A schematic diagram of contact angle drops on surface and b) A photograph of Dataphysics OCA 40 [65]

2.4.2 Characterization of electrochemical properties

Measurement of capacitive properties is necessary to evaluate performance and application for designing electrode materials. Electrochemical measurement was carried out in a three or two electrode cell to an electrochemical workstation by Metrohm AUTOLAB PGSTST 302 as shown in Fig. 2.17. The main tests used to characterize performance were analyzed by cyclic voltammetry, galvanostatic charge-discharge, electrochemical impedance spectroscopy.

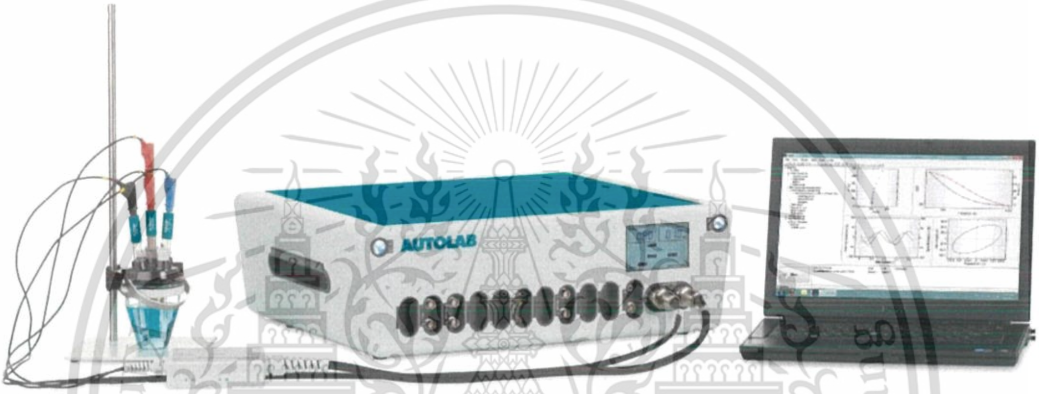

Figure 2.17 A photograph of Metrohm AUTOLAB PGSTST 302 [66]

2.4.2.1 Cyclic voltammetry (CV)

Cyclic voltammetry (CV), is one of the commonly used electrochemical measurement techniques with the advantage of ability to characterize an electrochemical system that is surface and electrolyte electrochemical reaction. In CV measurement, a sweep voltage is applied for current measurement. Characteristic profiles of these capacitive mechanism from the CV technique are shown in Fig. 2.18. The specific capacitance can be calculated from the integration of the current response in a cyclic voltammogram using the following equation;

$$C = \frac{\int i\, dV}{\Delta V v_s} \tag{2.17}$$

where, C is the capacitance (F), $\int idV$ is the integration of sweep in CV, ΔV is the potential window width, and V_S is the potential scan rate.

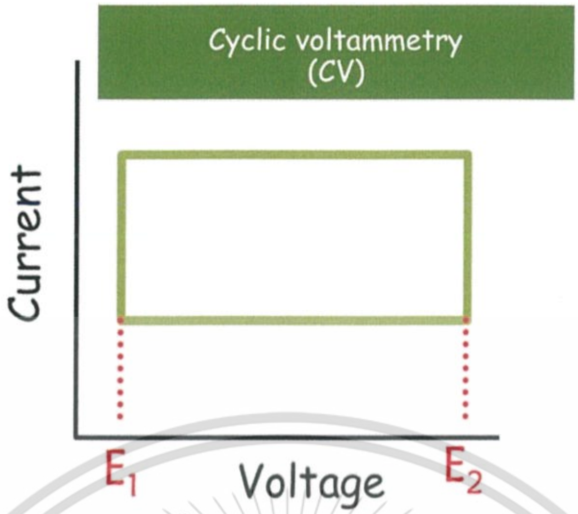

Figure 2.18 Cyclic voltammogram of an ideal EDLC

2.4.2.2 Galvanostatic charge-discharge (CD)

Galvanostatic charge-discharge (CD) is the standard technique used to test the performance, equivalent series resistance, and cycle-life of supercapacitor. In CD measurement, a constant current is applied for voltage vs time measurement as shown in CD profile in Fig. 2.19. The capacitance from CD curve can be calculated by equation (2.18). The loop is repeated in many cycles to observe repeatability and cycle-life time before performance is dropped.

$$C = \frac{I\Delta t}{\Delta V} \tag{2.18}$$

where, C is the capacitance, I is a constant current, Δt is discharge time, and ΔV is the potential window.

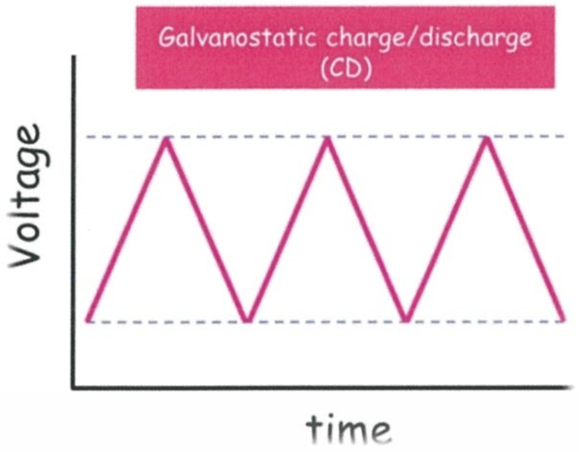

Figure 2.19 Galvanostatic curve of supercapacitor

2.4.2.3 Electrochemical impedance spectroscopy (EIS)

The resistance and capacitance of supercapacitors can be explained by electrochemical impedance spectroscopy (EIS). In EIS measurement, voltage is applied over a frequency range for impedance measurement. Fig. 2.20 shows the Nyquist plots of supercapacitor. The Nyquist spectra consists of 2 parts: in the high-frequency (HF, semicircle) and in the low-frequency (LF, liner line). The HF region shows a resistance information that the offset on the x-axis is series resistance (R_s) which is the sum of the intrinsic resistance of the electrode material, the electrolyte resistance and the contact resistance between the electrode material and the current collector. The diameter of the semicircle shows the kinetic resistance to the ion transfer (R_{CT}). The LF region shows a straight line, indicating the ion diffusion rate at the interface between the electrode-electrolyte materials.

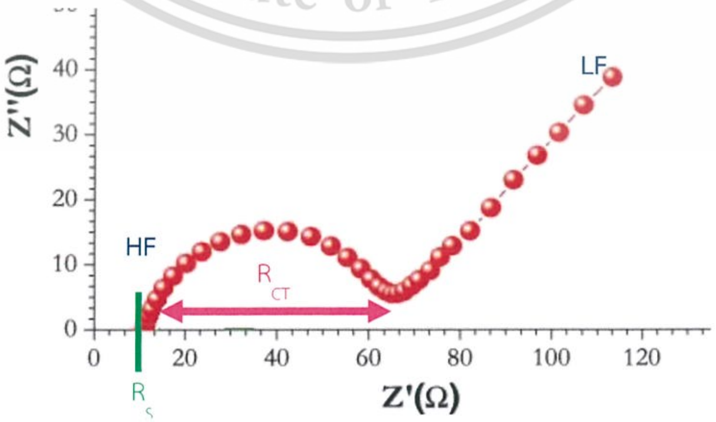

Figure 2.20 Nyquist plot of supercapacitor

2.4.2.4 Energy and power density

Two primary attributes of a capacitor are its energy and power density, both of which can be expressed as quantity per unit weight (specific energy or power) or per unit volume. The energy *E* [J] stored in a capacitor is related to the charge *Q* [C], at each interface and the potential different *V* [V], and therefore is directly proportional its capacitance as show in equation (2.4)

Maximum energy is achieved when *V* is at a maximum, which is usually limited by the breakdown strength of the dielectric.

In general, power (*P*) is the rate of energy delivery per unit time. The resistance of the internal components of the capacitor (e.g., current collectors, electrode materials, dielectric/electrolyte, and separator) needs to be considered to determine *P* for a certain capacitor. The resistance of these components is usually measured in the total resistance referred to as the equivalent series resistance (ESR) [Ω]. The ESR, by introducing a voltage drop, determines the maximum voltage of the supercapacitor during discharge and therefore limits the maximum energy and power of a supercapacitor. The measurement of power for supercapacitor is often measured at match impedance (i.e., the resistance of the load is assumed to be the same as the supercapacitor ESR) which corresponds to the maximum power P_{max}, given by

$$P_{max} = \frac{V^2}{4ESR} \tag{2.19}$$

However, even though the resistance of a good supercapacitor is typically much lower than that of the connected load, the actual delivered peak, although still very high, is usually lower than P_{max}.

CHAPTER 3

FUNCTIONALIZATION OF MULTI-WALLED CARBON NANOTUBE

This chapter describes the method to improve energy density of supercapacitor by increasing capacitance. Functionalization of multi-walled carbon nanotube (f-MWNT) was prepared using microwave and oxygen plasma techniques to add oxygen-containing functional groups to MWNT. The functional group of f-MWNT material was characterized by Fourier transform infrared spectroscopy (FTIR). The carbon structure of materials was analyzed by Raman spectroscopy and transmission electron microscopy (TEM). The nitrogen-adsorption isotherm was observed by the gas adsorption analyzer. The hydrophilic property of materials was analyzed by the contact angle. The supercapacitor performance was analyzed by 3 techniques; cyclic voltammetry, galvanostatic charge/discharge and electrochemical impedance spectroscopy (EIS).

3.1 Synthesis of electrode materials

3.1.1 Functionalization of f-MWNT by microwave and plasma treatments

The multi-walled carbon nanotube (MWNT) with a diameter of 10-20 nm and a length of 1-5 μm was used as electrode material. Functionalization of surface material by increasing oxygen-containing functional group is a key factor to enhance supercapacitor performance as shown in Fig. 3.1. The MWNT was functionalized by two techniques. Microwave and oxygen plasma treatments and its properties were compared.

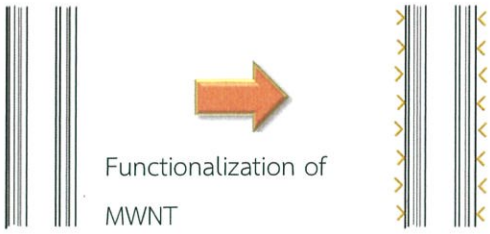

Figure 3.1 Schematic view of functionalized MWNT

3.1.1.1 Microwave treatment

For microwave treatment, MWNT (2.5 g) was heated at 500 °C for 1 h under air ambient and after that treated via commercial microwave oven at 650 W for 70 s in air, called m-MWNT. The m-MWNT was characterized by Fourier transform infrared spectroscopy, Raman spectroscopy, and transmission electron microscopy. The wettability property of the m-MWNTs was analyzed by the contact angle technique.

3.1.1.2 Oxygen plasma treatment

For oxygen plasma treatment, MWNT (0.55 g) was treated by oxygen plasma technique at an RF frequency of 13.56 MHz and a power of 18 W for 30 min by an expanded plasma cleaner (Harrick Scientific), called p-MWNT. The p-MWNT was characterized their functional groups, graphitic structures and hydrophilic properties by Fourier transform-infrared spectroscopy, Raman spectroscopy, and contact angle technique, respectively.

3.1.2 Electrode preparation based on f-MWNT

The MWNT paste was prepared by mixing the f-MWNT as the active materials, and polyvinylidene fluoride (PVDF) in n-methyl-2-pyrrolidone (NMP) as the binder in the weight ratio of 11:1. The mixture of f-MWNT and PVDF solution was homogenized for 30 min at 7,000 rpm and subsequently sonicated for 30 min. To fabricated, f-MWNT based electrode, current collector was used as stainless-steel type 304 (SS304). The SS304 was cleaned with 10 min in hydrochloric acid (HCl) and washed with deionized

(DI) water to remove remaining HCl solution until pH 7. The SS304 was covered via f-MWNT paste with an area of 5x5 mm^2 and dried at room temperature for 12 h.

3.2 Morphology and structural characterization of f-MWNT

The analytical instruments used for characterization of electrode materials were summarized in Table 3.1.

Table 3.1 Characterization techniques and their corresponding information

Techniques	Information
Transmission electron microscopy (TEM; JEOL JEM-2010)	Internal structure
Raman spectroscopy (Thermo Scientific DXR smart Raman)	Carbon structure
Fourier transform infrared spectroscopy (FTIR; Thermo Scientific Nicolet 6700)	Surface functional group
Brunauer, Emmett and Teller (BET; Micromeritic ASAP 2020)	Surface area and porosity
Contact angle (Dataphysics OCA 40)	Hydrophilic property

3.2.1 Internal structure of f-MWNT

The internal structure of the f-MWNT was characterized by transmission electron microscopy (TEM) using an accelerated voltage at 200 kV with LaB_6 filament. The sample for TEM characterization was prepared by dispersing f-MWNT in ethanol solution and subsequently dropped onto copper (Cu) grid.

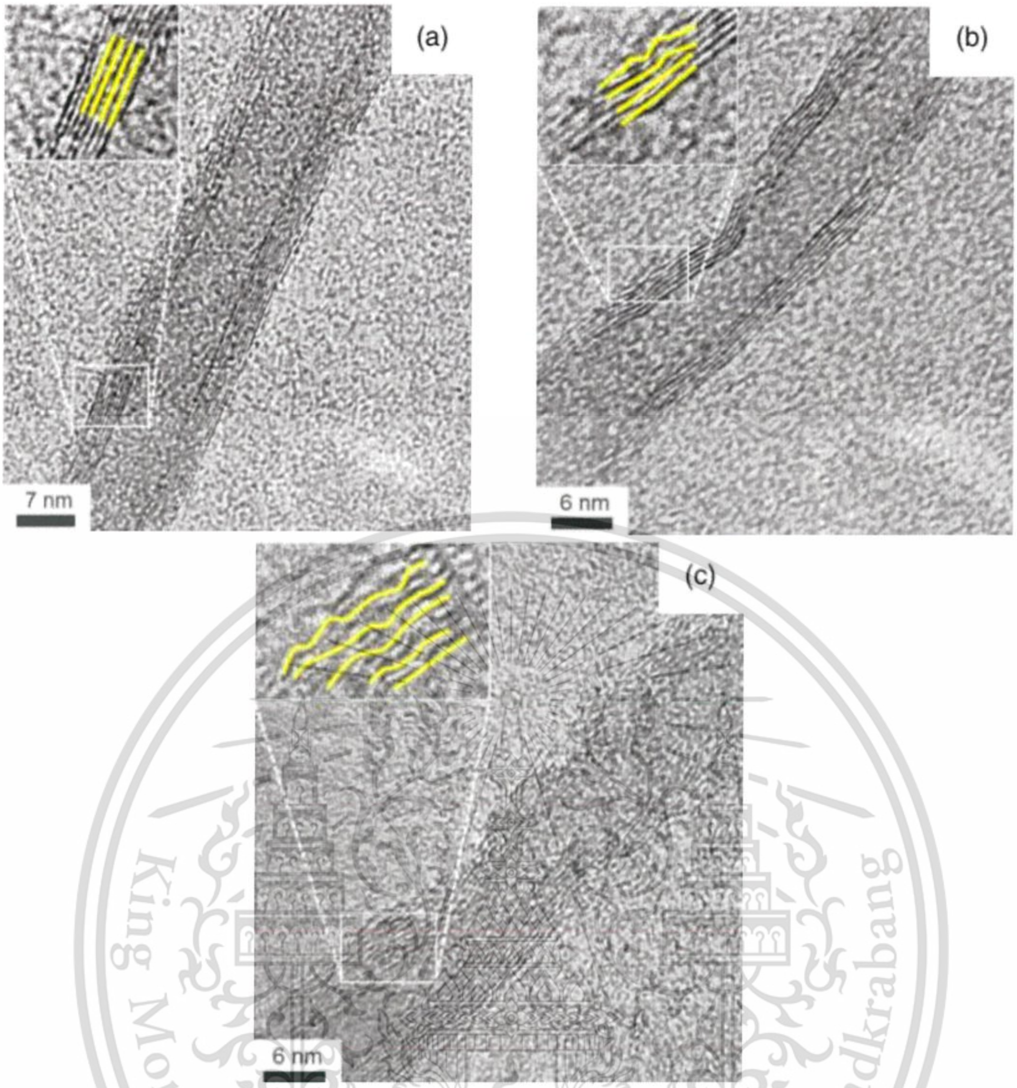

Figure 3.2 TEM images of (a) pristine MWNT, (b) m-MWNT and (c) p-MWNT

The morphologies of MWNT was investigated by TEM. Fig. 3.2 shows the TEM images of pristine MWNT, m-MWNT, and p-MWNT, respectively. Pristine MWNT (Fig. 3.2a) show graphene planes parallel, indicating the MWNT structure. The m-MWNT (Fig. 3.2b) was partially damaged sidewalls, while the p-WMNT (Fig 3.2c) was significantly damaged on sidewalls of MWNT. These results found that inner walls of MWNTs still remained entire whereas the outer walls of MWNTs only were damaged owing to the defect generation. It is known that functionalized MWNT created defect on sidewalls of MWNT. The defect of MWNT was confirmed by Raman spectroscopy characterization.

3.2.2 Carbon structure of f-MWNT

The carbon structure, graphitic and defect of f-MWNT was analyzed by Raman spectroscopy with a laser wavelength of 532 nm (2.33 eV). The Raman spectra of the different electrode materials are shown in the Fig. 3.3. The Raman spectra of pristine MWNT, m-MWNT, and p-MWNT composed of two peaks around ~1336 cm^{-1} and ~1567 cm^{-1} which are known as the D-band (the sp^3 hybridized carbon and disordered carbon structure) and G-band (the graphitic structure dominated by sp^2 bonds) [67,68]. The intensity ratio of the G- and D-band (I_D/I_G) of pristine MWNT was 1.22. After treatment, the I_D/I_G ratio of m-MWNT and p-MWNT were 1.26 and 1.41 respectively, implying that the oxygen plasma cloud etch sp^3 carbon slower than sp^2 carbon [16].

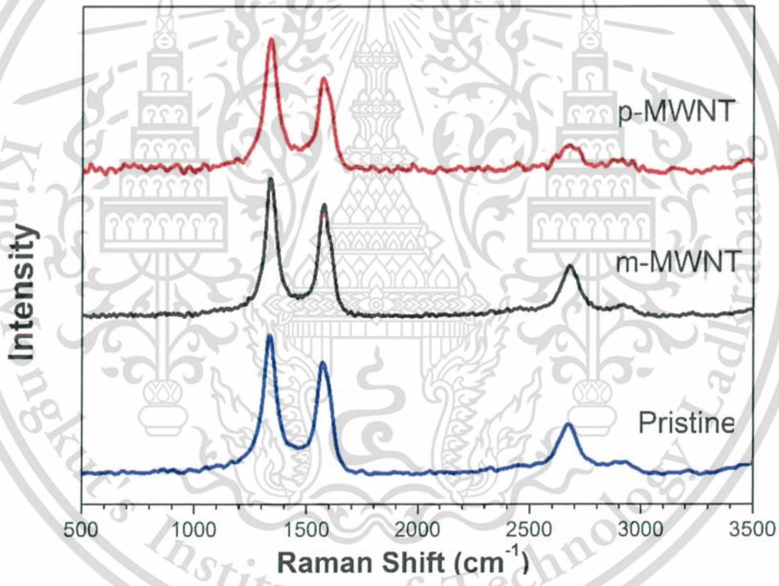

Figure 3.3 Raman spectra of the different electrode materials

After treatment, it was found that the sidewalls of MWNT created defect and MWNT tips were removed. The oxygen-contained functional groups were introduced onto MWNT surface. In the case of m-MWNT, microwaves are a part of the electromagnetic spectrum with frequencies ranging from 915 to 2,450 MHz, which induces polar molecules to rotate and produce thermal energy in a process known as dielectric heating. Microwave heating is more efficient and fast via direct energy transfer. In the case of p-MWNT, atoms or radicals from the plasma chemically react with the surface. Plasma treatment was an efficient method to generate a large amount of oxygen-containing functional groups on the surface of MWNT. In addition, compared both of m- and p-MWNT, it was found that p-MWNT can effectively create the defect on the sidewalls of MNWT more than m-MWNT due to chemical reaction via oxygen radicals.

3.2.3 Functional group of f-MWNT

The functional group characterization of f-MWNT was operated by Fourier transform infrared (FTIR) spectroscopy. The f-MWNT powder and potassium bromide (KBr) was mixed and pressed into a pellet form for FTIR sample. The FTIR spectra were scanned in a wavenumber range of 500-4000 cm^{-1}.

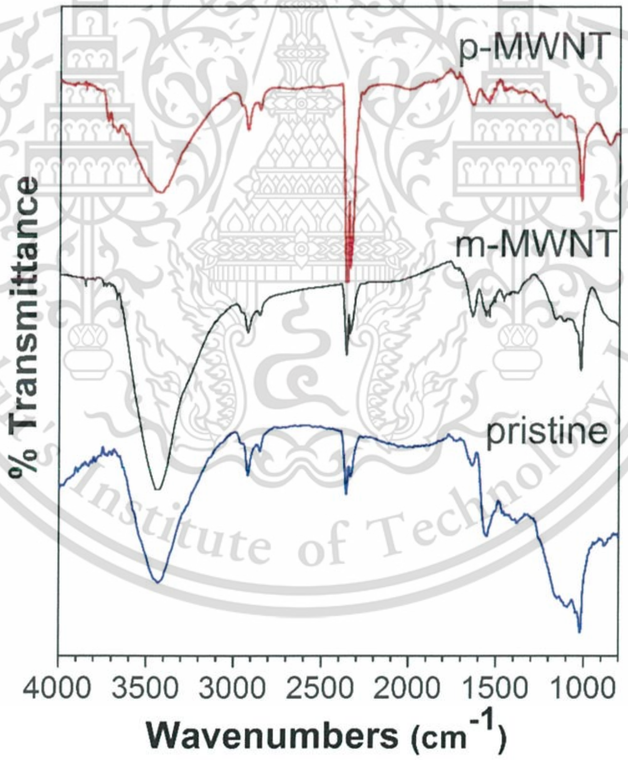

Figure 3.4 FTIR spectra of the different electrode materials

Fig. 3.4 shows the functional group in the pristine MWNT, m-MWNT, and p-MWNT with several peaks. The FTIR spectra indicates the peaks located at 1020, 1596, 1640, 1750 cm^{-1}, corresponds to C-O group, aromatic ring (C=C), carbonyl (C=O), carboxyl, respectively. The band at 2336, 2361 cm^{-1} are attributed to the O-H stretch from strongly hydrogen-bonded-COOH. The peak at 2856 and 2922 cm^{-1} are assigned to the C-H of the methyl group. The peak at 3432 cm^{-1} corresponds to the hydroxyl (-OH) group. The point of this study, focusing on the peak at 1596, 1640, and 2361 cm^{-1}, the C=C stretching was decreased, the carbonyl group was increased in m-MWNT and p-MWNT, and the carboxyl group was increased in p-MWNT after functionalization. These results found that the microwave and oxygen plasma treatments exhibit the effective methods to increase the functional groups on the walls of CNTs. On the basis of this structure, the reaction mechanisms that occur during the plasma treatment including the generation of the C-O, C=O, and O-C=O bonds. The concentration of C=C bond was decreased with increasing treatment time. Oxygen radicals were also generated on the surface, as shown in Fig. 3.5. The new C-O and C=O bonds are believed to form from these oxygen radicals through intramolecular reorganization on the C-C bonds. New O-C=O bonds were believed to form on the C=O bonds through the combination of the plasma generate radicals on the C=O bonds and the active oxygen atoms [69]. These results show that p-MNWT was generated a large amount of O-C=O bonds on the surface than m-MWNT due to the reactivity of oxygen radicals and treatment time of p-MWNT longer than m-MWNT

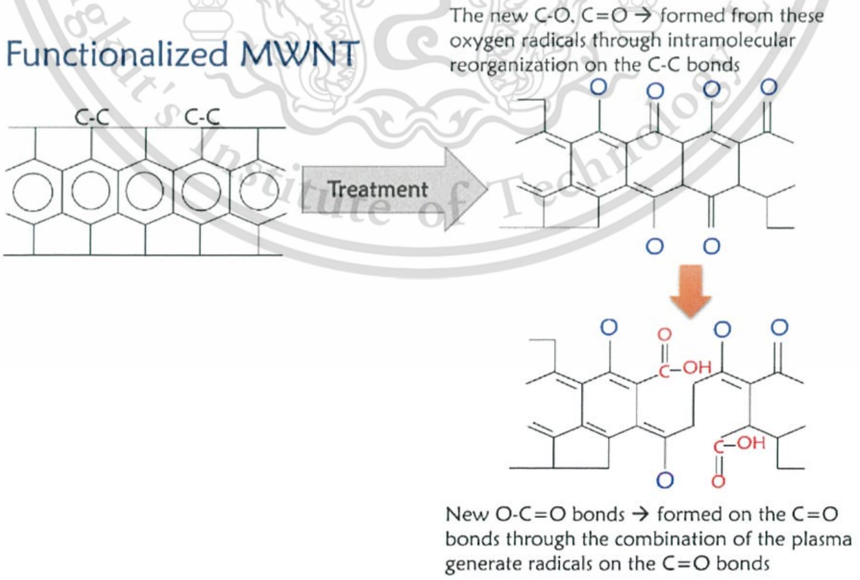

Figure 3.5 Schematic reaction mechanism on the sidewall of functionalized MWNT [69].

3.2.4 Surface area and porosity of f-MNWT

The nitrogen adsorption and desorption isotherms of each material shown in Fig. 3.6 exhibit the nature of type IV adsorption isotherms, implying the existence of the mesoporous structure. Fig. 3.7 shows the pore size distribution of all materials obtained by the DFT method. It can be seen that all the materials have the mesoporous size in the range of 2-50 nm. The specific surface area (S_{BET}) of pristine MWNT, m-MWMT, and p-MWNT were 276.38, 202.74 and 305.06 m^2g^{-1}, respectively. The pore volume (V_{total}) of pristine MWNT, m-MWMT, and p-MWNT were 0.755, 0.297 and 0.854 cm^3g^{-1}, respectively. The specific surface area was in the following order: p-MWNT>pristine MWNT>m-MWNT. The p-MWNT has the highest S_{BET} lead to the tube tips cut off and surface defected, the bundles of MWNT was separate. In addition, the added oxygen-contain functional groups in the carboxylate MNWT reduced aggregation of the individual tubes [70], thus increasing the effective surface area.

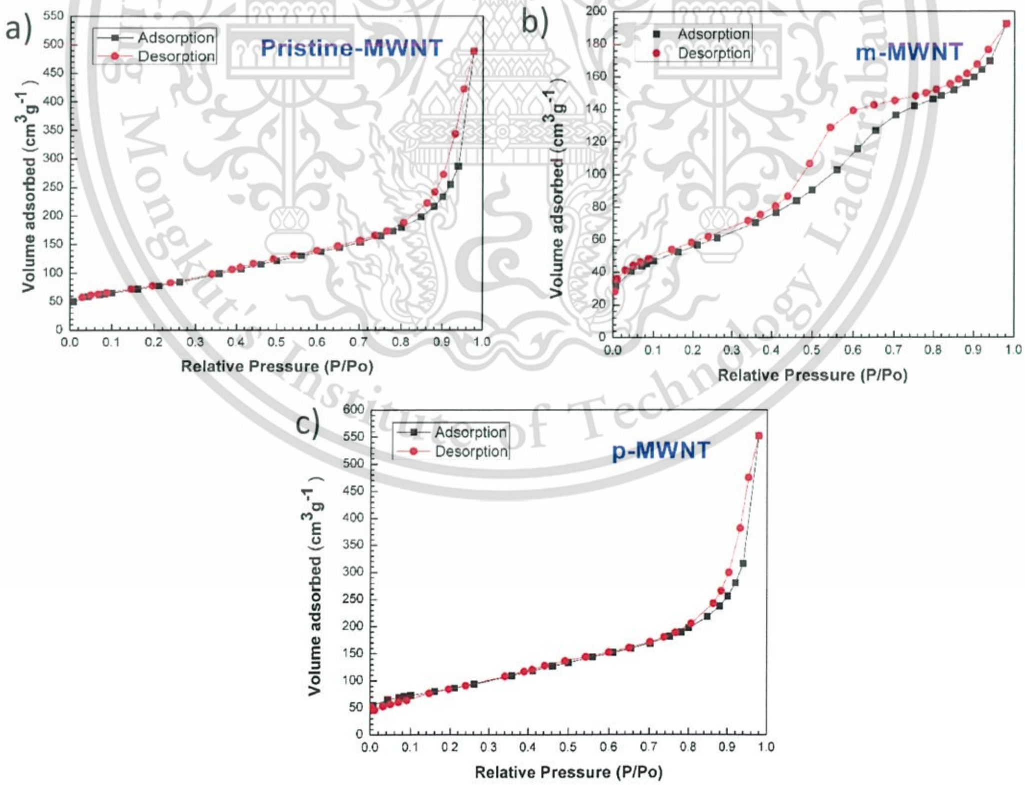

Figure 3.6 Nitrogen adsorption-desorption isotherm of different materials (a) pristine MWNT, (b) m-MWNT, and (c) p-MNWT

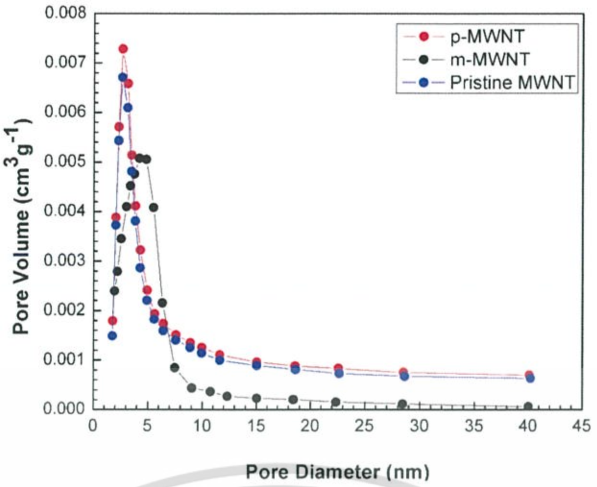

Figure 3.7 Pore size distribution of all materials

3.2.5 Wettability of f-MWNT

The hydrophilicity properties of f-MWNT was analyzed by the contact angle technique. Electrolyte aqueous solution was dropped onto f-MWNT-coated SS304.

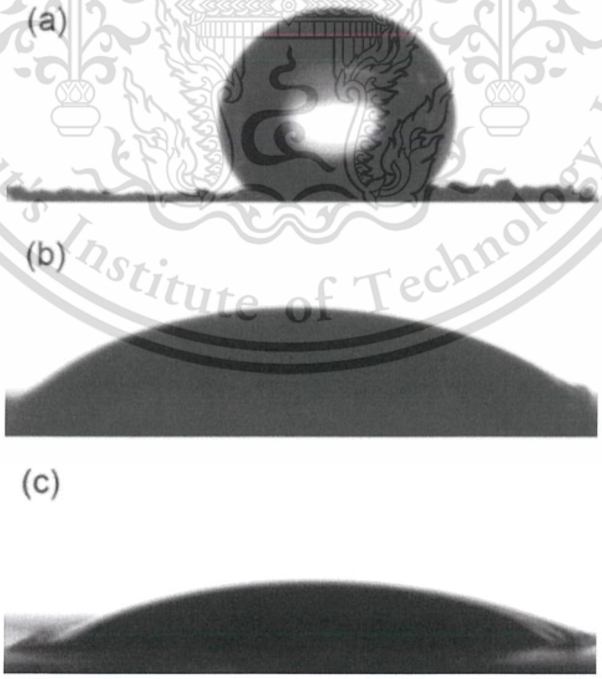

Figure 3.8 Contact angles of (a) pristine MWNT, (b) m-MWNT and (c) p-MWNT

The wettability properties were measured via the contact angle (CA) technique. CA can determine the wettability degree, which the surface is classified as hydrophilic (CA < 90°) or hydrophobic (CA > 90°). Fig. 3.8 shows the contact angle of the pristine MWNT, m-MWNT and p-MWNT are approximately 113.84, 36.48, and 19.87 degrees, respectively. These results show the trend of contact angle between the electrolyte solution and the electrode surface, the contact angle was in the following order: pristine MWNT> m-MWNT> p-MWNT. The low CA indicates the best wettability property. The improved wettability of the p-MWNT materials was attributed to the oxygenated functional group of MWNT.

3.3 Characterization of electrochemical properties of f-MWNT

3.3.1 Electrode assembly of f-MWNT

Electrochemical measurement of the f-MWNT was operated in a three-electrode system (Metrohm AUTOLAB PGSTAT 302) as shown in Fig. 3.9. The 3-electrode setup for electrochemical analysis is summarized in Table 3.2.

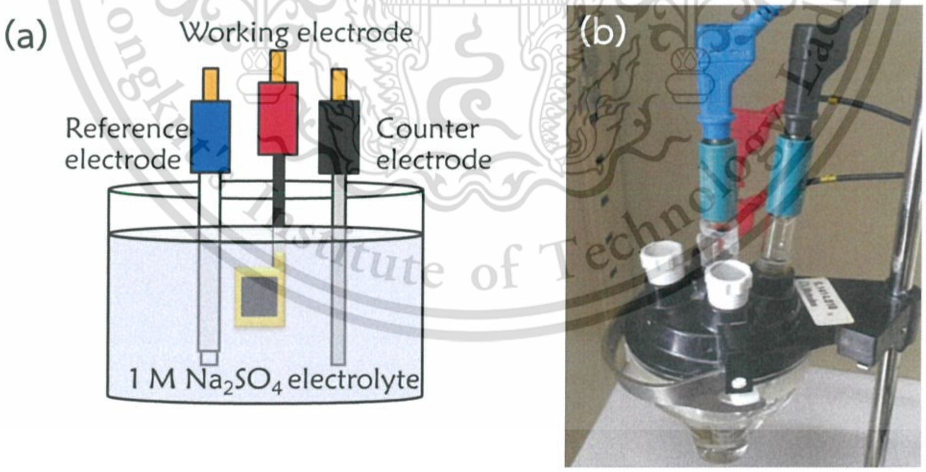

Figure 3.9 (a) Schematic diagram and (b) photograph of 3-electrode setup for electrochemical analysis

Table 3.2 Electrode setup for electrochemical properties

Electrode	3 electrodes setup
Working electrode	f-MWNT
Counter electrode	Pt sheet
Reference electrode	Ag/AgCl
Electrolyte	1 M Na_2SO_4

3.3.2 Cyclic voltammetry of f-MWNT

Electrochemical properties of f-MWNT was characterized by cyclic voltammetry (CV). The CV curves collected at a scan rate 100 mVs^{-1} in a window from 0.0 to 0.8 V. The specific capacitances (C_{sp}) were calculated from CV curves by the following equation:

$$C_{sp} = \frac{\int_{V_1}^{V_2} i(V)dV}{2(V_2-V_1)mv} \tag{3.1}$$

Where $\int i(V)dV$, V_2-V_1, m and v are integration of positive and negative sweeps in CV curve, voltage window (V), weight of active materials (g) and scan rate (Vs^{-1}), respectively.

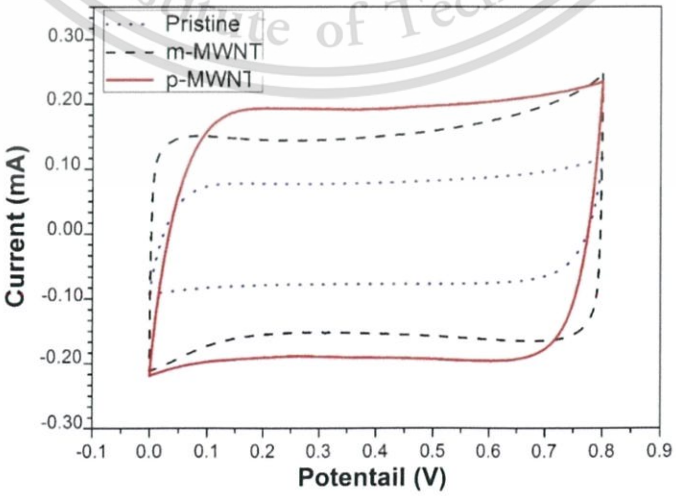

Figure 3.10 CV curve of different electrode materials at a scan rate of 100 mVs^{-1}

Fig. 3.10 presents the CV curves of pristine MWNT, m-MWNT, and p-MWNT. The CV curves show the rectangular shape without the redox peak, implying typical EDLC characteristics. The specific capacitance was calculated using equation (3.1). The specified capacitances of the pristine MWNT, m-MWNT, and p-MWNT were 24.58, 85.76, and 104.62 Fg^{-1}, respectively. Normally, MWNT has hydrophobic properties because of the sp^2 lattice of graphitic carbon suggested that the electrolyte ions were blocked accessibility into the electrode surface. On the other hand, microwave and oxygen plasma treatments of MWNT shows hydrophilic properties as demonstrated via the decrease in contact angle measurement. So, the m-MWNT and p-MWNT permit into access electrolyte ions to the surface of electrode more easily than the pristine MWNT, implying to enhance specific capacitance [71,72]

3.3.3 Galvanostatic charge-discharge of f-MWNT

The galvanostatic charge-discharge (CD) tests of f-MWNT was operated at a constant current of 1 mA in a window from -0.2 to 1.0 V. The specific capacitances (C_{sp}) were calculated from CD curves by the following equation:

$$C_s = \frac{I \times \Delta t}{\Delta V \times m} \tag{3.2}$$

Where *I*, *Δt*, and *ΔV* are current (A), discharge time (s), and voltage change after a full charge or discharge (V), respectively.

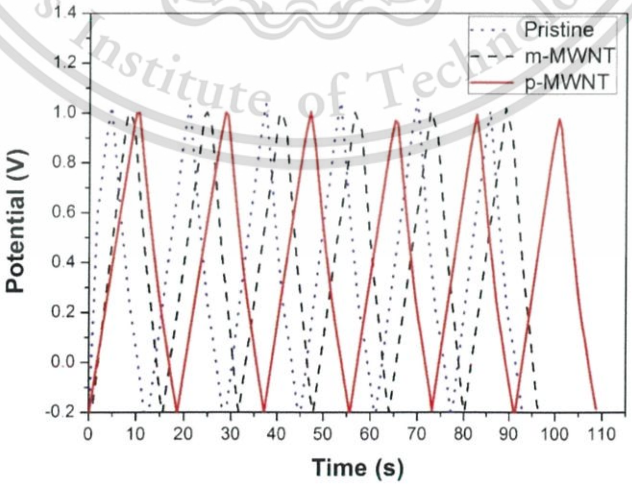

Figure 3.11 CD curve of different electrode materials at an applied constant current of 1 mA

Fig. 3.11 shows the galvanostatic charge–discharge (CD) curves of pristine MWNT, m-MWNT, and p-MWNT. The CD curve shows a shape look like as isosceles triangle, implying a good electrochemical reversibility. In this CD curves, voltage drop was disappeared, resulting a low internal resistance of the electrode [73].

3.3.4 Electrochemical impedance spectroscopy of f-MWNT

Electrochemical properties of f-MWNT were characterized by electrochemical impedance spectroscopy (EIS). The EIS tests were operated at an amplitude of 5 mV in a frequency range between 10 kHz and 0.01 Hz.

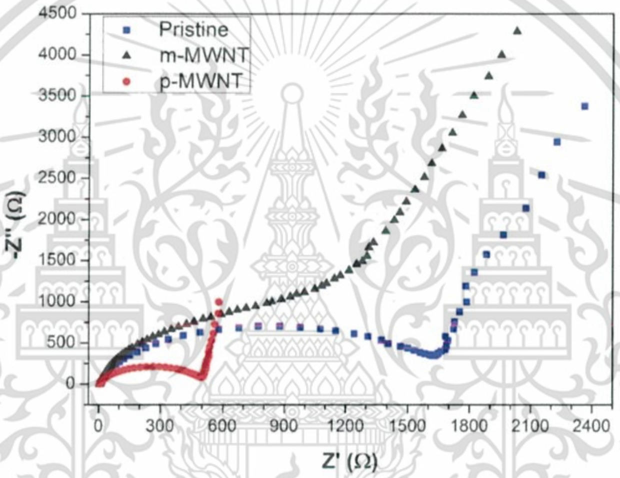

Figure 3.12 The Nyquist plot in the frequency range of 10 kHz–10 mHz at an amplitude of 5 mV in 1 M Na_2SO_4 aqueous electrolyte

Fig. 3.12 shows the Nyquist spectra of all electrode materials. A semicircle relates to high frequencies and a linear portion relates to low frequencies. The slopes of the lines in the low-frequency regions range from lowest to highest agree with the pristine MWNT, m-MWNT and p-MWNT, respectively. The p-MWNT shows a straight line, implying the highest ion diffusion rate at interface of electrode materials and electrolyte, and indicating an ideal supercapacitor behavior. For the functionalization of the oxygen-containing functional group via plasma treatment, the wettability property of the electrode surface is exhibited the high ion diffusion rate [17]. The wettability properties improve the movement of Na^+ and SO_4^{2-} ions in the electrolyte penetrating deeply inside the micropores, while the m-MWNT shows a slightly less wettability compared to p-MWNT. Furthermore, the Nyquist spectra at the high-frequency (semicircle shapes) could be described intrinsic resistance, electrolyte resistance, and the resistivity of contact between the current collector and the electrode materials, which is a measure of series resistance (R_s) [31]. The R_s of the pristine MWNT, m-MWNT, and p-MWNT were 4.99, 4.87, and 4.18 Ω, respectively. The diameter of the semicircle is the charge transfer resistance (R_{CT}). The pristine MWNT display the largest diameter, indicating the highest R_{CT}, which the p-MWNT display the smallest diameter, indicating the lowest R_{CT}. These results indicated that the treated MWNT could be attributed to the good charge transfer in the electrode-electrolyte interface, implying the improvement in the conductivity and wettability property.

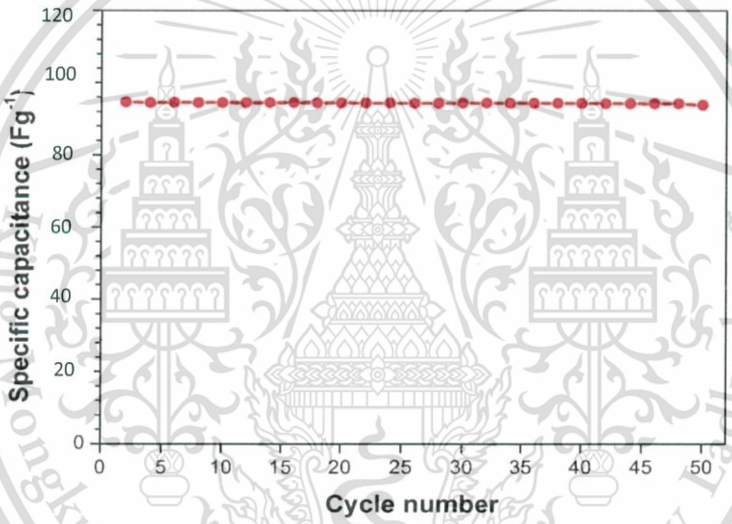

Figure 3.13 The cycling stability of p-MWNT in 1 M Na_2SO_4 aqueous electrolyte

The energy density (E) and power density (P) were calculated using the following equations:

$$Energy\ density\ (E; Whkg^{-1})\ = \frac{CV^2}{2x3.6} \tag{3.3}$$

$$Power\ density\ (P; Wkg^{-1})\ = \frac{Ex3600}{discharge\ time} \tag{3.4}$$

where *C*, *V*, and *discharge time* are specific capacitance (Fg^{-1}), potential window (V) and discharge time (s), respectively.

Table 3.3 Electrochemical performance of pristine MNWT and functionalized MWNT

Electrode	Specific capacitance (Fg^{-1})	Energy density ($Whkg^{-1}$)	Power density ($kWkg^{-1}$)
pristine-MWNT	24.58	2.18	0.12
m-MWNT	85.76	7.62	0.31
p-MWNT	104.62	9.30	0.33

The electrochemical performance of pristine MWNT and functionalized MNWT was summarized in table 3.3. The p-MWNT shows energy density of 9.30 $Whkg^{-1}$ and power density of 0.33 $kWkg^{-1}$ respectively. Fig. 3.13 shows the stability of the p-MWNT electrode materials. The specific capacitance of p-MWNT remains 99.13% after 1,000 CD cycles. Though the p-MWNT seem to as deteriorate easily meanwhile exhibits better stability. The p-MWNT presents a promising use as energy storage devices

3.4 Summary

The microwave and oxygen plasma treatments of electrode materials for supercapacitor based on MWNTs were researched. The treated MWNT shows the increasing of oxygen-containing functional groups, surface area and wettability property. The p-MWNT shows the highest specific capacitance of 104.62 Fg^{-1}, an energy density of 9.30 $Whkg^{-1}$, power density of 0.33 $kWkg^{-1}$ at the voltage window of 0.8 V. The specific capacitance of p-MWNT remains 99.13% after 1,000 CD cycles. The p-MWNT shows the highest specific capacitance and energy density with the 4.3-fold increasing compared to that of the pristine-MWNT. The capacitance improvement is attributed to the increase in the number of oxygen-containing functional groups, implying that oxygen plasma treatment is a rapid and efficient method for the modification of MWNTs.

CHAPTER 4

SYNTHESIS OF MANGANESE DIOXIDE NANOSHEET AND FUNCTIONALIZED MULTI-WALLED CARBON NANOTUBE HYBRID MATERIALS

This chapter describes the method to improve energy density of supercapacitor by increasing capacitance. The capacitance was increased by hybrid materials of manganese dioxide (MnO_2) nanosheet and functionalized MWNT (f-MWNT) hybrid materials (MnO_2/f-MWNT) to combine pseudocapacitive and EDLC properties. The electrode consists of 2 layers; f-MWNT, and MnO_2 nanosheet. MnO_2 is well known as a good material for the electrode due to its wide potential range in positive side and high theoretical specific surface area, low cost, and environmental friendliness. The MnO_2/f-MWNT was characterized the morphology, the chemical states, and the crystal structure by scanning electron microscope (SEM), X-ray photoelectron spectroscopy (XPS), and X-ray diffraction (XRD) techniques, respectively. The nitrogen-adsorption isotherm was observed by the gas adsorption analyzer. The electrochemical properties of MnO_2/f-MWNT were characterized by cyclic voltammetry (CV), galvanostatic charge/discharge (CD) and electrochemical impedance spectroscopy (EIS) techniques.

4.1 Synthesis of electrode materials

4.1.1 Manganese dioxide (MnO_2) nanosheet and f-MWNT hybrid materials (MnO_2/f-MWNT)

This section explains the synthesis of MnO_2/f-MWNT hybrid electrodes for supercapacitor application. The supercapacitor electrode consists of 2 layers; f-MWNT and MnO_2 nanosheet (MnO_2-NS). MnO_2-NS was deposited onto the f-MWNT/Ni foam by electroplating technique. Supercapacitor performance based on these hybrid materials was optimized by varying synthesis times of MnO_2-NS to increase the specific surface area of electrode as shown in Fig. 4.1. The following section describes each step-in detail.

Figure 4.1 Schematic view of MnO_2-NS to increase the surface area

4.1.1.1 Functionalized multi-walled carbon nanotube (f-MWNT) layer

The f-MWNT was prepared by the method described in section 3.1.1.2. Next, the f-MWNT and PVDF were mixed at a weight ratio of 11:1 in NMP, and subsequently pasted onto nickel (Ni) foam with an area of 5x5 mm^2 and heated at 100 °C for overnight under an argon gas.

4.1.1.2 Manganese dioxide nanosheet (MnO_2-NS) layer

MnO_2 nanosheets was deposited onto the prepared MnO_2 thin film/f-MWNT/Ni foam by GS mode of electrodeposition technique at a constant current of 1 mA/cm^2 using 0.1 M $MnSO_4$ as a precursor with different deposited times of 10, 15 and 20 min (hereinafter referred to as MnO_2-NS-10, MnO_2-NS-15, and MnO_2-NS-20, respectively). The MnO_2 nanosheet conditions was summarized in Table 4.1

Table 4.1 Electrodeposition condition of MnO_2-NS

Precursor concentration:	0.1 M $MnSO_4$
Current density:	1 mA/cm^2
Temperature	60°C
Electrode gap:	1 cm
Time:	10, 15 and 20 min
Cathode	Ni foam
Anode:	Graphite

4.1.2 Electrode preparation based on MnO_2/f-MWNT

After electroplating, the MnO_2/f-MWNT hybrid electrodes were washed with deionized water and dried under air ambient at 100 °C for 12 h before electrochemical characterization. The weight of MnO_2/f-MWNT coated on Ni foam was measured by weighing the Ni foam before and after coating using a digital balance.

4.2 Morphology and structural characterization of MnO_2/f-MWNT

The analytical instruments used for characterization of electrode materials were summarized in Table 4.2.

Table 4.2 Characterization techniques and their corresponding information

Techniques	Information
Field emission scanning electron microscopy (FE-SEM; Hitachi S-4800)	Morphology structure
X-ray photoelectron spectroscopy (XPS; AXIS Ultra DLD)	Elemental and chemical composition
X-ray diffraction (XRD; Rigaku, TTRAX III)	Crystal structure

4.2.1 Morphology property of MnO_2/f-MWNT

The morphologies of the MnO_2/f-MWNT hybrid electrodes were characterized by field-emission scanning electrode microscopy (FE-SEM; HITACHI S-4700) using an accelerated voltage at 10 kV in high vacuum mode with a base pressure of approximately 9×10^{-5} Pa.

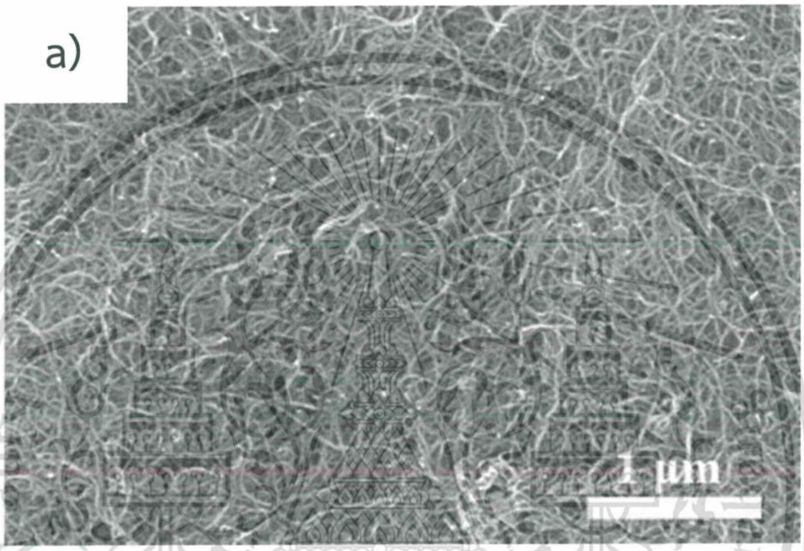

Figure 4.2 SEM image shows the morphological structure of f-MWNT on Ni foam

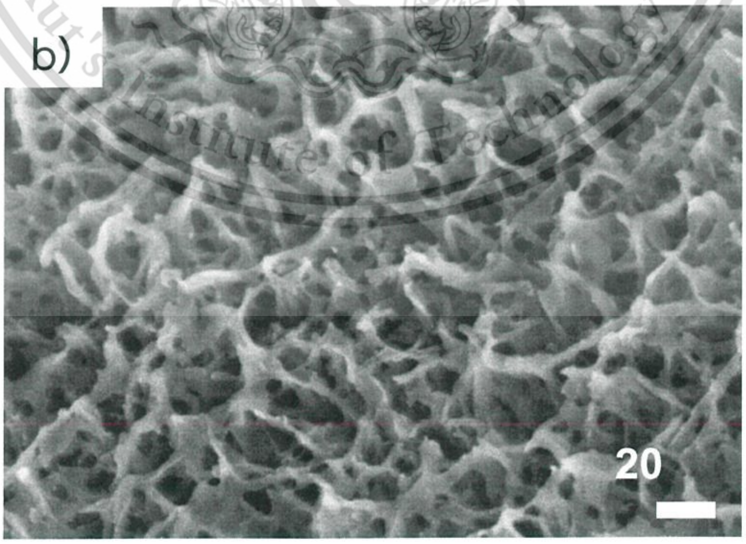

Figure 4.3 SEM images shows the morphological structure of MnO_2-NS-15 on Ni foam

Fig. 4.2 shows the SEM images of f-MWNT on Ni foam. The f-MNWTs combined with a network of overlying MWNTs, arranging a conductive network structure on the Ni foam. The MnO_2-NS-15 min as shown in Fig. 4.3 exhibits the porous with a pore diameter approximately 5-20 nm due to the interconnection of the MnO_2 nanosheet. The average pore diameter of hybrid materials (MnO_2-NS-15/f-MWNT) calculated from nitrogen adsorption/desorption isotherm was 21.71 nm, respectively. This morphology is ideal for the supercapacitor electrode since it can enhance the mass transport of electrolyte due to the capillary force [74].

The mechanism of MnO_2 nanosheet is proposed that OH^- ions were supplied and Mn2$^+$ ions migrated to cathode to form $Mn(OH)_2$, by following reaction;

$$Mn^{2+} + 2OH^- \rightarrow Mn(OH)_2 \tag{4.1}$$

After that, $Mn(OH)_2$ was ionized by following reaction

$$Mn(OH)_2 \rightarrow MnO + H_2O \tag{4.2}$$

From question (4.2), only MnO was formed. The crystal structure of MnO, α-MnO_2, and δ-MnO_2 were detected, as will show in XPS results. This indicates the possible oxidation of MnO as follows.

$$2MnO + O_2 \rightarrow 2MnO_2 \tag{4.3}$$

and/or

$$4MnO + O_2 \rightarrow 2Mn_2O_3 \tag{4.4}$$

proceeded.

4.2.2 Chemical states of MnO_2 nanosheet

From peak deconvolution as shown in Fig. 4.4, the separated peaks were illustrated and matched with binding energy at 641.09, 642.45, 643.84, and 645.25 eV, indicating that oxidation states were Mn^{2+}, Mn^{4+}, Mn^{6+} and Mn^{7+} as showing details in Table 4.3. The XPS spectra shows the two main peaks at 653.8 and 641.9 eV, indicating to core-level Mn $2p_{3/2}$ and Mn $2p_{1/2}$ peak. A spin-energy separation of 11.8 eV was seen between the two peaks, implying the formation of MnO_2 [75]. This result will also be confirmed by XRD analysis.

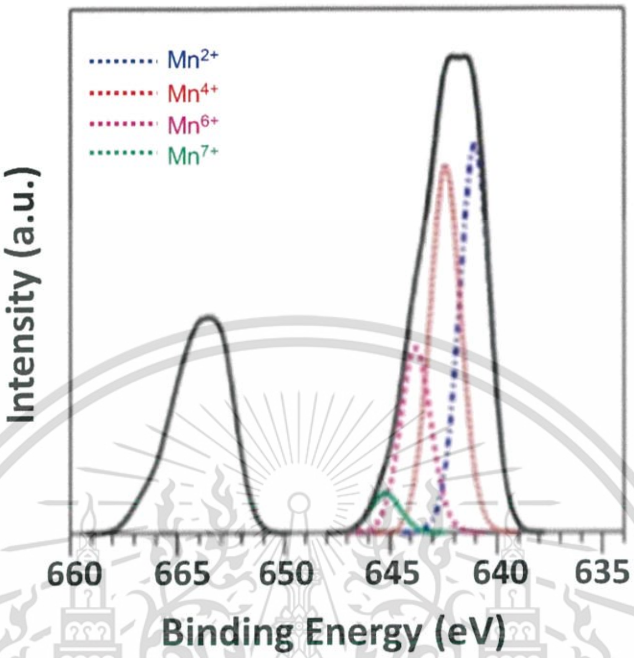

Figure 4.4 XPS spectra of MnO_2-NS-15

Table 4.3 The atomic percentage of each oxidation states of MnO_2-NS

Binding energy (eV)	Oxidation stage	Atomic % of Mn information
641.09	Mn^{2+}	39.5
642.45	Mn^{4+}	39.0
643.84	Mn^{6+}	18.0
645.25	Mn^{7+}	3.5

4.2.3 Crystal structure of MnO_2 nanosheet

To confirm the crystallinity, the MnO_2-NS-15 was characterized by XRD as shown in Fig. 4.5. The XRD spectra exhibit a board peaks at ~18.7°, ~22.4° and 36.2 °, which correspond to the structure of α-MnO_2 (200) and δ-MnO_2 (002, 110). The MnO_2

nanosheet is indexed as a mixture of α- and δ-phases (JCPDS 44-141 and 43-1456), respectively [76,77]. The structures of α-MnO_2 and δ-MnO_2 were shown in Fig 4.6. This result shows a facile synthesis of hybrid materials by electrodeposition technique. The nanosheet structures were mixed between α- and δ-phase-MnO_2. The α-MnO_2 has a good electron transport while the δ-MnO_2 has high external surface area and large reactive active sites for fast charge transfer, which is favorable for the electrochemical reaction at electrode/electrolyte interface. In addition, it is well known that the crystal structure of MnO_2 with different tunnel sizes can strongly influence the insertion/extraction of protons or cation during the charge-discharge process. The α-MnO_2 with 2x2 tunnels (~4.6 Å) is generally considered to be stable structured supercapacitor material. However, smaller tunnels are not beneficial for the fast insertion/extraction of cations [78]. Compared with α-MnO_2, δ-MnO_2 has wider ionic diffusion tunnels (~6.9 Å). However, its crystal structure is very unstable during electrochemical reaction [78,79]. Fortunately, our MnO_2 nanosheet was successfully a mixture between α- and δ-phase-MnO_2, which can stabilize crystal structure during the charge-discharge process and contributes to the enhancement in high rate capability and cycling stability for pseudocapacitor.

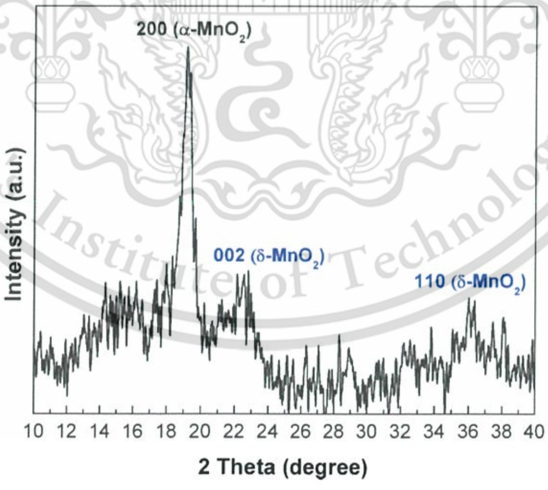

Figure 4.5 XRD spectra of MnO_2-NS-15

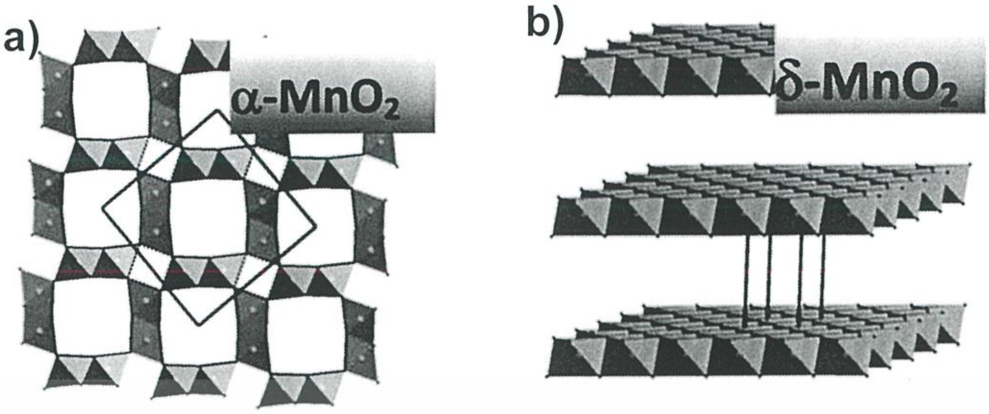

Figure 4.6 The crystal structure of MnO_2 a) α-MnO_2 and b) δ-MnO_2 [77,78]

4.3 Characterization of electrochemical properties of MnO_2/f-MWNT

4.3.1 Electrode assembly of MnO_2/f-MWNT

Electrochemical measurement of MnO_2/f-MWNT was carried out by the method described in section 3.3.1. The MnO_2/f-MWNT electrode was used as a working electrode. The Pt and Ag/AgCl electrodes were used as the counter and reference electrodes, respectively. 1 M Na_2SO_4 aqueous solution was used as the electrolyte.

4.3.2 Cyclic voltammetry of MnO_2/f-MWNT

Electrochemical properties of MnO_2/f-MWNT was characterized by cyclic voltammetry. CV tests were operated at a potential range of 0.0 to 0.8 V at a scan rates 100 mVs^{-1}. The specific capacitance from CV curve can be calculated by equation (3.1).

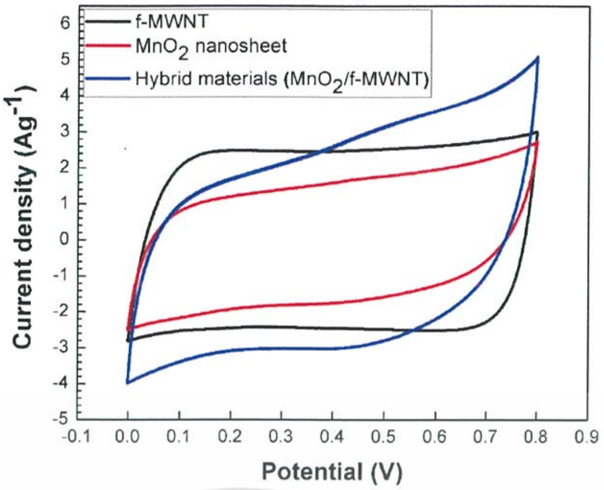

Figure 4.7 CV curve of f-MWNT, MnO_2 nanosheet and hybrid materials at a scan rate of 100 mVs^{-1}

Previously, the electrochemical behavior of f-MNWT, MnO_2 nanosheet and the hybrid materials (MnO_2-NS-15/f-MWNTs) were evaluated using the three-electrode system as shown in Fig. 4.7. From the area of the CV curve, the specific capacitances were calculated using equation (3.1). The specific capacitance of f-MNWT, MnO_2 nanosheet and the hybrid materials (MnO_2-NS-15/f-MWNTs) were approximately 104.62, 76.63, and 116.40 Fg^{-1}, respectively. The hybrid materials enabled approximately 1.5-fold improvement in the specific capacitance compared to the MnO_2 nanosheet, respectively. These results may be attributed to the increase in effective surface area by MWNTs and the increase in Faradic reaction by MnO_2.

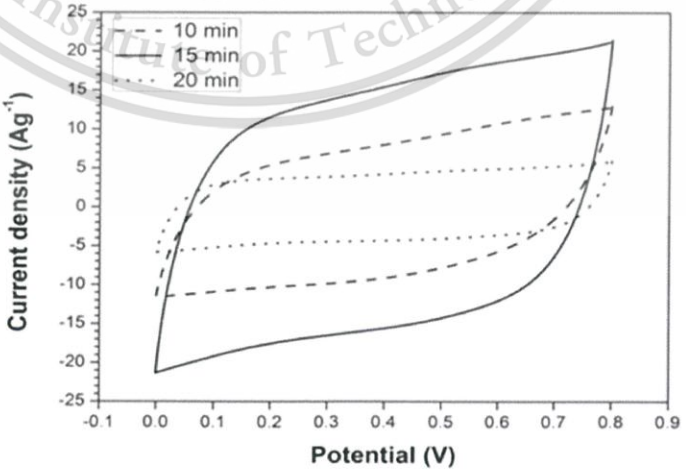

Figure 4.8 CV curve of different synthesis times of MnO_2-NS at a scan rate of 100 mVs^{-1}

Next, the optimum amount of the MnO_2-NS in the hybrid MnO_2-NS/f-MWNT electrode materials was investigated. Fig. 4.8 shows CV curves of the MnO_2-NS/f-MWNT with different deposition times of the MnO_2-NS at 10, 15 and 20 min. The CV curve shapes of the MnO_2-NS/f-MWNT electrodes are quasi-rectangular indicating the presence of both electrical double-layer capacitance and pseudocapacitance [80]. The area of CV curves was increased with increasing deposition time of the MnO_2-NS. However, when the deposition time increased to 20 min, the area of CV curve suddenly decreased. The MnO_2-NS-15/f-MWNT shows the largest of the area of CV curve due to maximizing the role of the porous structure and improving good conducting channels [81].

4.3.3 Galvanostatic charge-discharge of MnO_2/f-MWNT

The galvanostatic charge-discharge (CD) test of MnO_2/f-MWNT was performed in a voltage range of 0.0 to 0.8 V at a current density of 1 Ag^{-1}. The specific capacitance can be calculated from CD curve using the equation (3.2).

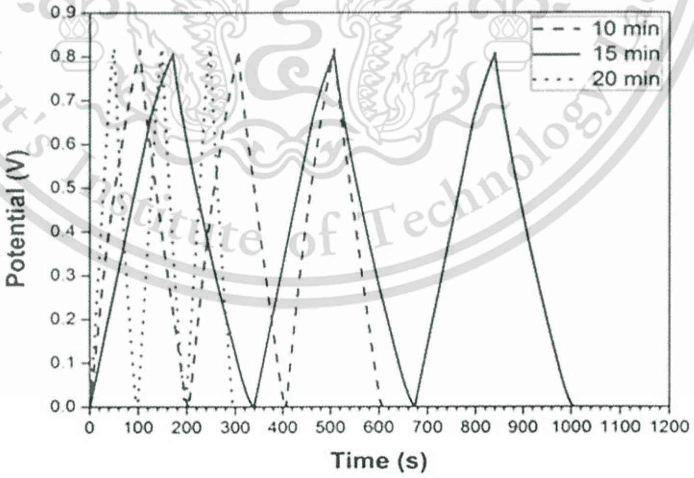

Figure 4.9 CD curve of different synthesis times of MnO_2 at current density of 1 Ag^{-1}

Fig. 4.9 presents the galvanostatic charge-discharge (CD) curves within the operating voltage range of 0 to 0.8 V at a current density 1 Ag^{-1}. The CD curves show a shape of a nearly isosceles triangle, implying good electrochemical reversibility. No apparent voltage drop was observed at the discharge current, suggesting a low internal resistance of the electrode. The specific capacitance was calculated using the equation (3.2). The specified capacitances of MnO_2-NS/f-MWNT with different deposited times of 10, 15 and 20 min were 122.31, 144.10, and 55.46 Fg^{-1}, respectively. The MnO_2-NS-15/f-MWNT shows the highest specific capacitance as follows; (i) the increase in effective surface area by the combination of MnO_2/f-MWNT, (ii) the increase in Faradaic reaction by MnO_2 nanosheet, (iii) the maximization of porous structure and (iv) the improvement of conducting channel. The specific capacitance derived from the CD curves shows the same trends as those from the area of CV curve, i.e. the specific capacitance was in the following order: 15 > 10 > 20. The charge times of the MnO_2-NS/f-MWNT with different deposition times of 10, 15 and 20 min were 100.68, 166.68 and 49.03 sec, respectively.

4.3.3 Electrochemical impedance spectroscopy of MnO_2/f-MWNT

Electrochemical properties of MnO_2/f-MWNT was characterized by electrochemical impedance spectroscopy (EIS). The EIS tests were carried out in a frequency range between 10 kHz and 10 mHz at an amplitude of 5 mV.

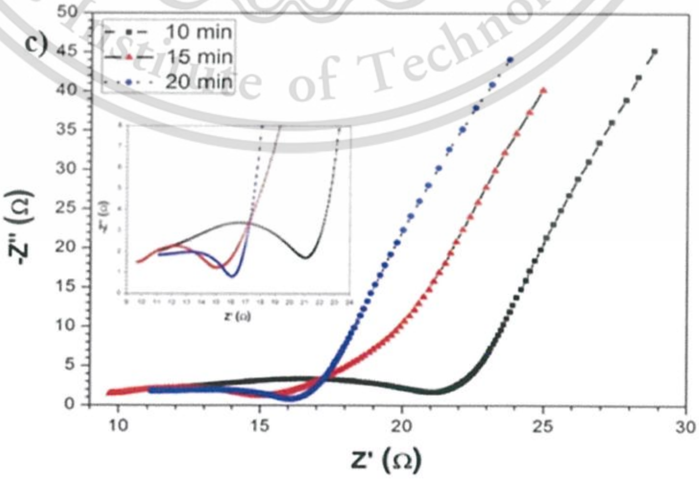

Figure 4.10 EIS in the frequency range of 10 kHz–10 mHz of different synthesis times of MnO_2 at an amplitude of 5 mV

Fig. 4.10 shows the Nyquist plots of the MnO_2/f-MWNT in the frequency range of 10 kHz–10 mHz. The inset shows the magnified high-frequency region. The obtained Nyquist spectra for all configurations consist of a semicircle in the high-frequency region and a linear line in the low-frequency regions. All electrodes show resembles semicircle curve, but different diameters, revealing the different intrinsic resistance (R_S) and the resistivity of contact between the electrode material and the current collector (R_{CT}), which is a measure of series resistance. The R_S and R_{CT} are determined from the offset on the x-axis, (Z') (Ω) of the high-frequency semicircle and the diameter of the semicircle, respectively. The values of R_S of the MnO_2/f-MWNT with different deposition times of 10, 15 and 20 min are estimated to be 11.06, 9.69, and 11.12 Ω, respectively. Similarly, the values of R_{CT} are estimated to be 9.98, 4.35, and 4.89 Ω, respectively. The MnO_2-NS-15/f-MWNT shows the smallest semicircle, implying the smallest R_{CT}. A comparable R_s of all sample shows a similar contact resistance between the electrode material and the current collector. The smallest R_{CT} of the MnO_2-NS-15/f-MWNT indicates the good charge transfer in the electrolyte–electrode interface, which is due to the highest surface area of the MnO_2/f-MWNT.

Table 4.4 Electrochemical performance of different synthesis times of MnO_2

Electrode	Specific capacitance (Fg^{-1})	Energy density ($Whkg^{-1}$)	Power density ($kWkg^{-1}$)
MnO_2-NS-10 f-MWNT	122.31	10.88	0.39
MnO_2-NS-15/ f-MWNT	144.10	12.80	0.28
MnO_2-NS-20/ f-MWNT	55.46	4.93	0.36

The electrochemical performance of different synthesis times of MnO2 was summarized in table 4.4. The energy density (E) and power density (P) of MnO_2-NS/f-MWNT with different deposited times of 10, 15 and 20 min were calculated using the equations (3.3) and (3.4). The MnO_2-NS-15/f-MWNT shows the highest energy density of 12.81 $Whkg^{-1}$ at power density of 0.28 Wkg^{-1}.

4.4 Summary

The hybrid MnO_2/f-MWNT electrode materials for supercapacitor were optimized by varying synthesis times of MnO_2. The MnO_2/f-MWNTs at 15-min-deposited MnO_2-NS show the highest specific capacitance of 144.10 Fg^{-1}, energy density of 12.81 $Whkg^{-1}$ and power density of 0.28 $kWkg^{-1}$ at the voltage window of 0.8 V. The MnO_2/f-MWNT shows the highest specific capacitance and energy density with the 5.8-fold increasing compared to that of the pristine-MWNT. The high capacitance value is due to the combination of the MnO_2 nanosheet and the f-MWNT, resulting in the high surface area, the low contact resistance between the electrode material and the current electrode, and the increase in Faradaic reaction. These results show that the MnO_2/f-MWNT hybrid materials are promising materials for a supercapacitor with high performance. Moreover, electrodeposition is a simple technique to control structure of the MnO_2/f-MWNT for electrode of supercapacitor.

CHAPTER 5

DESIGN OF ASYMMETRIC SUPERCAPACITOR BASED ON FUNCTIONLIZED MULTI-WALLED CARBON NANOTUBE AND HYBRID MATERILAS

This chapter explains the method to improve energy density of supercapacitor by increasing voltage window. A voltage window of supercapacitor was increased by fabrication of asymmetric supercapacitor (ASC) based on functionalized multi-walled carbon nanotubes (f-MWNT) and hybrid materials (MnO_2/f-MWNT). The requirements in the design and optimization of ASC are as follows; (i) the Faradaic and non-Faradaic electrodes should have a high charge/discharge rate capability, (ii) the potentials of the Faradaic and non-Faradaic electrodes should be close to either the low or high end of the operating potential window, (iii) this mismatch of the specific capacitance of the Faradaic and non-Faradaic electrodes can be compensated by balancing the active masses of the two electrode, and (iv) the non-Faradaic electrode should have a high electronic conductivity, surface area and porosity. ASC usually consists of two different electrodes. Generally, one electrode is for Faradaic reaction, and the other one is non-Faradaic or electrostatic. Therefore, in this research, the MnO_2/f-MWNT (positive electrode) was used as Faradaic electrode, assembled with the f-MWNT (negative electrode) was used as non-Faradaic electrode. The electrochemical properties of ASC were characterized by cyclic voltammetry, galvanostatic charge/discharge, and electrochemical impedance spectroscopy techniques.

5.1 Electrode preparation of asymmetric supercapacitor

5.1.1 Negative electrode base on f-MWNT

The negative electrode was prepared with the same condition as explained in section 3.1.1.2. Functionalized MWNT by oxygen plasma was used as a negative electrode material, called f-MWNT. The negative electrode was prepared by mixing f-MWNT and PVDF at the weight ratio of 11:1 in NMP, and then pasted on to Ni foam and dried at 100 °C for overnight.

5.1.2 Positive electrode base on MnO_2/f-MWNT

The positive electrode was prepared with the same condition as explained in section 4.1. The 15 min MnO_2/f-MWNT hybrid electrode material was used as a positive electrode material. The positive electrode consists of 2 layers: f-MWNT, and MnO_2 nanosheet. The f-MWNT was prepared with the same condition as explained in section 5.1.1. MnO_2 nanosheet was prepared by galvanostatic (GS) mode of electrodeposition technique at a constant current of 1 mA/cm^2 using 0.1 M $MnSO_4$ as a precursor with deposited time of 15 min. Next, the MnO_2/f-MWNT was washed by deionized (DI) water and dried at 100 °C for overnight.

5.1.3 Electrode assembly of f-MWNT//MnO_2/f-MWNT

The MnO_2/f-MWNT was used as a positive electrode and the f-MWNT was used as a negative electrode. For ASC assembly, Ni foam was used as a current collector with an area of 5x5 mm^2 and a polytetrafluoroethylene (PTFE) membrane was inserted between two electrodes as shown in Fig. 5.1. 1 M Na_2SO_4 aqueous solution was used as the electrolyte.

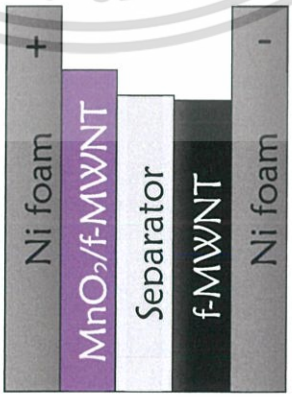

Figure 5.1 Schematic diagram of asymmetric supercapacitor (ASC)

5.2 Characterization of electrochemical properties of f-MWNT//MnO_2/f-MWNT

5.2.1 Cyclic voltammetry of f-MWNT//MnO_2/f-MWNT

Cyclic voltammetry (CV) curves of negative (f-MWNT) and positive (MnO_2/f-MWNT) electrodes were operated in a potential window range of 0.0 to 0.8 V at a scan rate of 100 mVs^{-1} as shown in Fig. 5.2. The electrochemical performance of negative and positive electrodes are summarized in Table 5.1. The capacitance value of the negative electrode is similar with positive electrode (normalized to the total active materials mass).

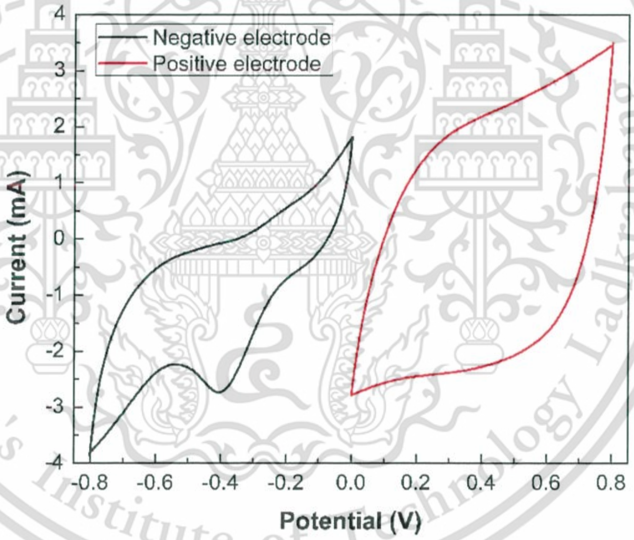

Figure 5.2 CV curves of negative (f-MWNT) and positive (MnO_2/f-MWNT) electrodes in 1 M Na_2SO_4 aqueous solution at a scan rate of 100 mVs^{-1}

Table 5.1 Electrochemical performance of negative and positive electrodes

Electrode	Weight (mg)	Voltage window (V)	Specific capacitance (Fg^{-1})	Energy density (Whkg-1)	Power density (kWkg-1)
Negative electrode	0.733	0.8	130.77	11.62	0.41
Positive electrode	0.744	0.8	142.67	12.68	0.27

The electrode potential can be defined against a reference electrode (known as electrochemical state) or with respect to electron energy at rest in vacuum (known as physical scale) [56,58]. When it is defined on a physical scale, the working voltage window of an electrochemical cell is given by

$$\mathrm{E} = \mathrm{E_0} + \Delta\mathrm{E_n} + \Delta\mathrm{E_p} \qquad \textbf{(6.1)}$$

$$\mathrm{E} = \left(\Phi_\mathrm{n} - \Phi_\mathrm{p}\right)\frac{\mathrm{qN_A}}{\mathrm{F}} + \Delta\mathrm{E_n} + \Delta\mathrm{E_p} \qquad \textbf{(6.2)}$$

where Φ_n and Φ_p are the work functions for the negative and positive electrodes, while q, N_A and F represent electron charge (1.6x10^{-9} C), the Avogadro's number (6.022x10^{23}) and Faraday constant (96,500 C/mol). ΔE_n and ΔE_p are the electrode potentials for the negative and positive electrodes, respectively

In ASC, the difference in the work function of the two electrodes can be widened by the operating voltage window beyond the decomposition energy of electrolyte because $\Phi_n - \Phi_p \neq 0$ and $\Delta E_1 \approx \Delta E_2$ for correctly charge balance electrode. In this work, work function of f-MWNT (negative electrode) was 4.95 eV and work function of MnO_2/f-MWNT (positive electrode) was 4.4 eV. Therefore, the expected stable operating voltage window was 2.15 V. In this work, the stable operating voltage window is 2.0 V as shown in Fig. 5.3. This decrease can be due to chemisorption of H^+ (OH^-) species on the negative (positive) electrode that modifies the work function different.

Also, the neutral aqueous (i.e., 1 M Na_2SO_4) electrolyte can provide maximum voltage up to 2.0 V without H_2/O_2 evolution due to highly hydrated sodium cation and sulfate anions i.e., ions with high hydration energy. Therefore, in this work, maximum open circuit voltage was limited to 2.0 V by the decomposition energy of the water.

CV curves were carried out with the various potential windows from 1.6 to 2.0 V. At 1.9 and 2.0 V, these are a hump which may be owing to irreversible chemical reaction. The maximum working potential window of ASC is 2.0 V. The CV curves of ASC in a potential window of 2.0 V shows the nearly rectangular shape as shown in Fig. 5.4, indicating excellent rate capability. The specific capacitance of ASC was calculated via equation (3.1) using the total mass of active materials from both negative and positive electrodes. The specific capacitance of ASC was approximately 66.97 Fg^{-1}.

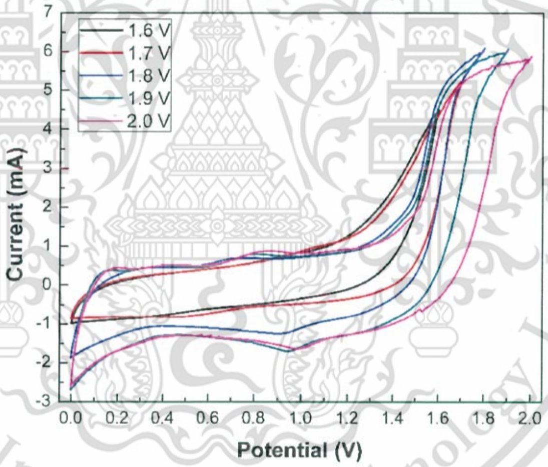

Figure 5.3 CV curves of ASC in different potential windows at a scan rate of 100 mVs^{1} in 1 M Na_2SO_4 aqueous solution

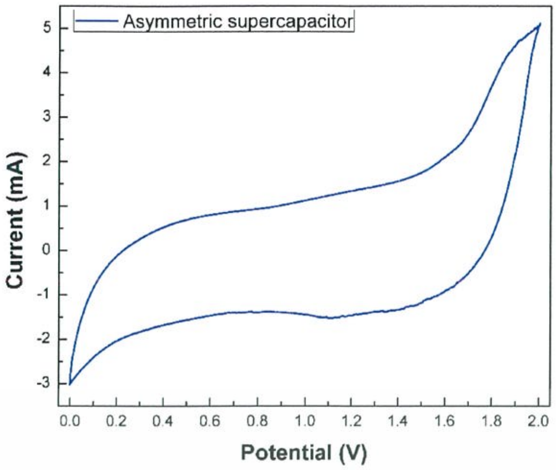

Figure 5.4 CV curves of ASC in a potential window from 0.0 to 2.0 V at a scan rate of 100 mVs^{-1} in 1 M Na_2SO_4 aqueous solution

5.2.2 Galvanostatic charge-discharge of f-MWNT//MnO_2/f-MWNT

The charge-discharge (CD) profiles of negative and positive electrodes were operated in potential window from 0.0 to 0.8 V at a current density of 1 Ag^{-1}. Fig. 5.5 shows a symmetrical triangle shape of negative and positive electrodes, indicating the good electrochemical meanwhile the CD curve of ASC shows a nearly triangular shape and have a slight IR drop, indicating small internal resistance as shown in Fig 5.6. The internal resistance of ASC will be confirmed by EIS.

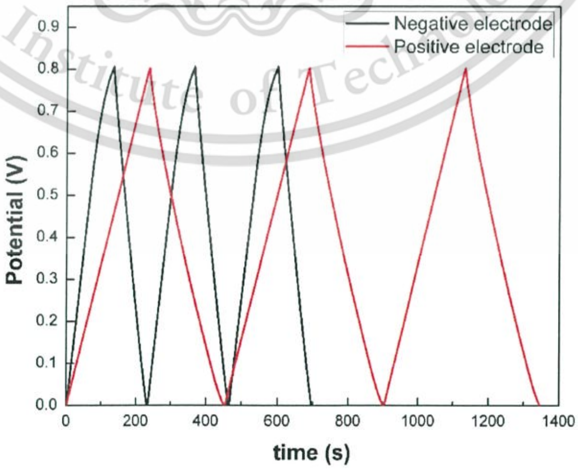

Figure 5.5 CD curves of negative (f-MWNT) and positive (MnO_2/f-MWNT) electrodes at a current density of 10 Ag^{-1} in 1 M Na_2SO_4 aqueous solution

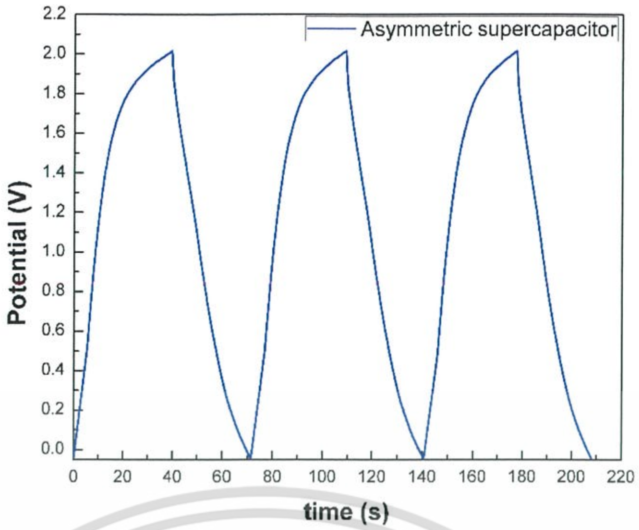

Figure 5.6 CD curves of ASC at a current density of 10 Ag^{-1} in 1 M Na_2SO_4 aqueous solution

5.2.3 Electrochemical impedance spectroscopy of f-MWNT//MnO_2/f-MWNT

Fig 5.7 shows the Nyquist plot of negative electrode, positive electrode and ASC device. The EIS spectra consists of a semicircle in the high frequencies and a linear portion in the low frequency regions. All EIS spectra represent the different offsets on the x-axis and different diameters of semicircle curves, indicating their different characteristics. The offset on the x-axis in the high-frequency region is the series resistance (R_s) of electrode such as intrinsic resistance, electrolyte resistance, and contact resistance between the current collector and the electrode materials. The Rs values of negative electrode, positive electrode and ASC device are evaluated to be 5.01, 6.06 and 7.09 Ω, respectively. The diameter of the semicircle indicates the kinetic resistance to charge transfer, called R_{CT}. The EIS spectra of negative electrode (black line) show the smallest semicircle, implying the lowest R_s and R_{CT} while showing a nearly vertical line in the low-frequency region, implying an ideal electrical double-layer capacitor (EDLC). The red line shows the EIS spectra of a positive electrode, in which a slope of 45° in the low frequency-line indicates a combination between EDLC and pseudocapacitor. The EIS spectra of ASC device (blue line) is worthy to note that the ASC device has battery type behavior [83,84].

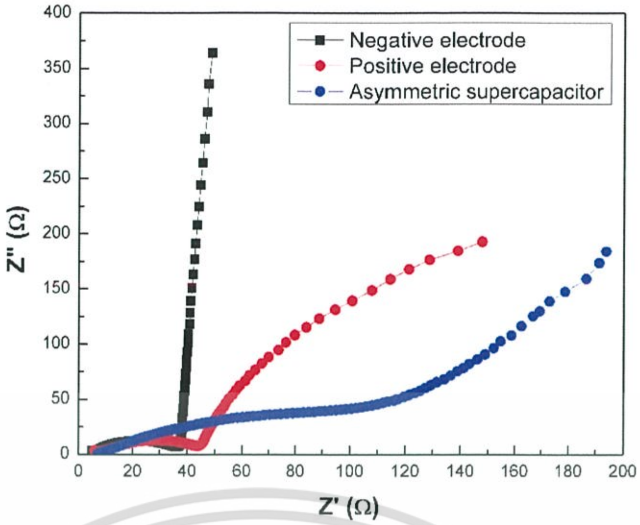

Figure 5.7 Nyquist plot of negative electrode, positive electrode and ASC in the frequency range of 10 kHz to 10 mHz at an amplitude of 5 mV

Table.5.2 Electrochemical performance of different electrode

Electrode	Weight (mg)	Voltage window (V)	Specific capacitance (Fg^{-1})	Energy density ($Whkg^{-1}$)	Power density ($kWkg^{-1}$)
Negative electrode	0.73	0.8	130.77	11.62	0.41
Positive electrode	0.74	0.8	142.67	12.68	0.27
Asymmetric supercapacitor	1.33	2.0	66.97	37.21	4.11

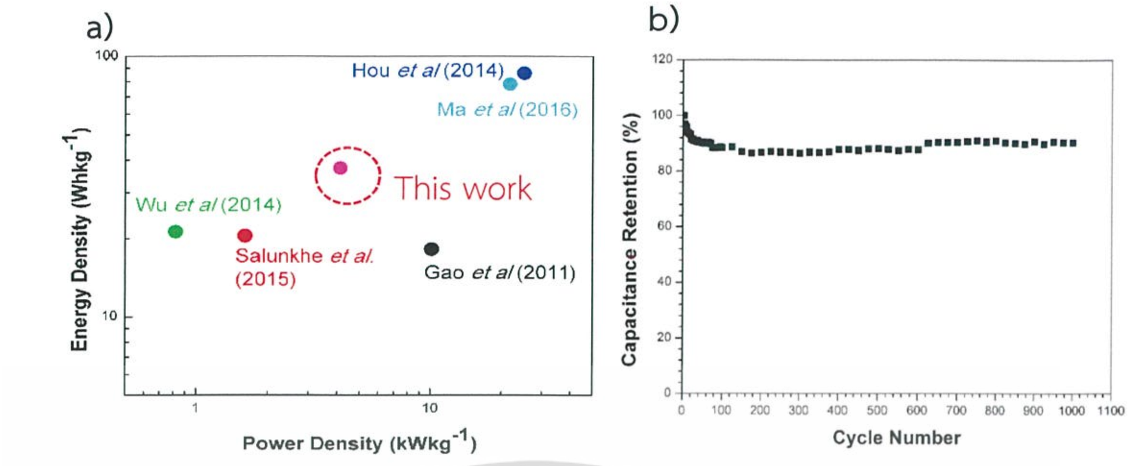

Figure 5.8 a) Ragone plot showing that the ASC (f-MWNTs and MnO_2/f-MWNTs) and other ASC data reported and b) Cycling stability of ASC device

Table 5.3 Electrochemical performance of the asymmetric supercapacitor

Electrode	Electrolyte	Capacitance (Fg^{-1})	Potential window (V)	Energy density ($Whkg^{-1}$)	Power density ($kWkg^{-1}$)
MnO_2-AC//AC (Gao *et al*, 2011)	Na_2SO_4	33.2	2.0	18.2	10.1
CNT-MnO_2 //ZNC (Salunkhe *et al*, 2015)	Na_2SO_4	57.0	1.6	20.4	1.6
MnO_2-rGO//rGO (Wu *et al*, 20114)	Na_2SO_4	59.9	1.6	21.2	0.82
MnO_2-rGO//Ppy-rGO (Hou *et al*, 2014)	$LiClO_4$	193.0	1.8	86	25
α-MnO2@δ-MnO_2// N-dope carbon (Ma *et al*, 2016)	KOH	153.8	1.6	78	21.7
This work	Na_2SO_4	66.97	2.0	37.21	4.11

The Ragone plot is a performance indicator for energy storage device. Fig. 5.8a shows the Ragone plot for energy density (*E*) and power density (*P*) of ASC device, which are calculated using the equations (3.3) and (3.4). The electrochemical performances of negative electrode, positive electrode and ASC are summarized in Table 6.2. The ASC device presents energy density of 37.21 Whkg^{-1} at power density 4.11 kWkg^{-1}, at an applied current density of 10 Ag^{-1}. Although, the specific capacitance of ASC decreased approximately 50%, compared to those of negative and positive electrode, but the window voltage of ACS increase from 0.8 V to 2.0 V. The increase of window voltage leads to an increase in energy density 3-times higher than those of negative and positive electrode. Moreover, the power density is also significantly improved 10- and 15-times, compared to those of negative and positive electrode, respectively. Moreover, these results indicated that the ASC device exhibits higher *E* and *P* than the previous reports by comparing with Na_2SO_4 aqueous electrolyte as shown in Fig. 5.8a. In the case of comparing between aqueous and ionic liquid electrolytes, energy density of ASC based on aqueous electrolyte is lower than that of ionic liquid electrolyte [21,29,77,81,85] as shown in Table 6.3. The enhancement of energy and power density are ascribed to the increased potential window. The electrochemical performance is enhanced via combination with good conductivity of f-MWNTs and the high energy density of MnO_2. Fig. 5.8b shows the capacitance retention *vs* the cycle numbers of ASC device. After 1000 cycles, the capacity retention is 90.5%, implying the good stability and good retention of capacitance.

5.3 Summary

Asymmetric supercapacitor (ASC) based on f-MWNT and MnO_2/f-MWNT was investigated. The MnO_2/f-MWNT was used as a positive electrode, assembled with the f-MWNT as a negative electrode. The specific capacitance of ASC is 66.97 Fg^{-1}. The ASC exhibits an energy density of 37.21 Whkg^{-1} at a power density of 4.11 kWkg^{-1}, indicating both considerable energy density and excellent power capability. The energy density of ASC was increased 17-fold compared to the pristine-MWNT. The ASC is an effective approach to enhance the energy density by increasing the operation voltage by utilizing the different potential windows of the two electrodes, and by increasing the specific capacitance by using hybrid material.

CHAPTER 6

SYNTHESIS OF ACTIVATED CARBON FROM GREEN LEAVES OF PAPAYA AND ITS ELECTROCHEMICAL PROPERTIES

This chapter explains the method to synthesize activated carbon form green leaves of papaya and study its electrochemical properties. The morphology, surface area, pore size distribution and chemical composition of activated carbon from papaya leaves were analyzed by scanning electron microscopy (SEM), nitrogen adsorption isotherm, and X-ray photoelectron spectroscopy (XPS). The electrochemical properties of activated carbon were characterized by cyclic voltammetry, and galvanostatic charge/discharge techniques.

6.1 Synthesis of electrode material

Since activated carbon (AC) is a main material used in commercial supercapacitor. Agricultural waste-derived AC has gained much attraction due to its low cost and locally available. Moreover, recently, it is reported that nitrogen-doped AC can significantly improve supercapacitor performance. Thus, in this research, one step synthesis of nitrogen-doped ACs from nitrogen-enrich papaya leaves was demonstrated.

6.1.1 Synthesis of activated carbon from papaya leaves

The fresh of papaya leaves were washed and dried in an oven at 100 °C for overnight. The leaves were cut into small pieces by a blender and subsequently carbonized at 400 °C for 2 h under argon flow rate of 0.5 Lmin^{-1} and washed with 1 M of sulfuric acid (H_2SO_4) for 3 h to remove impurities. It was dried at 110 °C in an oven for overnight. The activation process was mixed carbonized sample and sodium hydroxide (NaOH) at the weight ratio of 1:2.5 in the tubular furnace at 720 °C under argon gas at flow rate of 0.5 $\mathrm{Lmin^{-1}}$ for 2 h. Then, the sample was washed with deionized water and dried at 110 °C in an oven for overnight. The activated carbon from papaya leaves is called PL-AC.

6.1.2 Electrode preparation based on activated carbon from papaya leaves

The activated carbon paste was prepared by mixing the PL-AC, carbon black (CB) and polyvinylidene fluoride (PVDF) in n-methyl-2-pyrrolidone (NMP) at the weight ratio 80:10:10. The current collector was used as nickel (Ni) foam. The PL-AC pasted was coated onto Ni foam with an area of 5x5 $\mathrm{mm^2}$ and dried at 70 °C in an oven for overnight.

6.2 Morphology and structural characterization of activated carbon

The analytical instruments used for characterization of electrode materials were summarized in Table 6.1.

Table 6.1 Characterization techniques and their corresponding information

Techniques	Information
Scanning electron microscope (SEM; JEOL JSM-700F)	Morphologies
Nitrogen-adsorption isotherm (Micromeritics ASAP 2020)	Surface area and pore volume distribution
X-ray photoelectron spectroscopy (XPS; PHI Quantera II)	Chemical composition

6.2.1 Morphology of activated carbon

The morphology in Fig. 6.1 of the PL-AC shows a sponge-like structure and a lot of macropores appeared on surface.

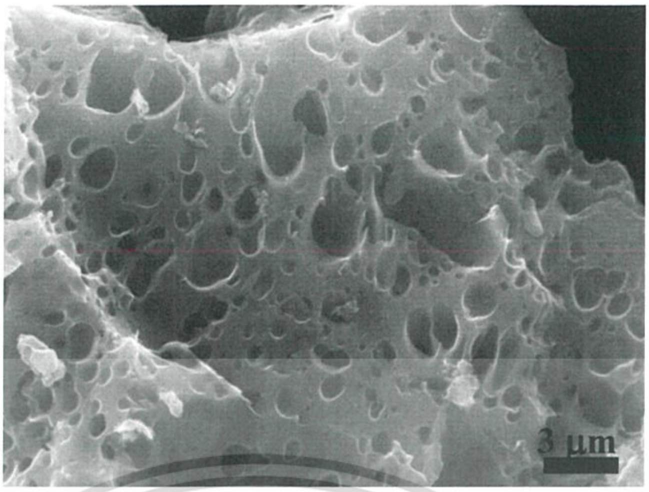

Figure 6.1 SEM image of PL-AC

6.2.2 Surface area and porosity of activated carbon

Fig. 6.2 shows the nitrogen adsorption and desorption isotherm of PL-AC. The PL-AC shows the type I isotherm indicated that the persistence of the microporous solid [86]. Fig 6.3 shows the pore size distribution of PL-AC got by the DFT method. It can be seen that the PL-AC have the highest pore volume at the diameter of 0.6 nm. The specific surface area (S_{BET}) and pore volume of PL-AC were 2664 m^2g^{-1} and 1.27 cm^3g^{-1}. The existence of micro- and mesoporous given a desirable pathway for transportation and penetration of electrolyte ion, which is important for fast ion transfer [87].

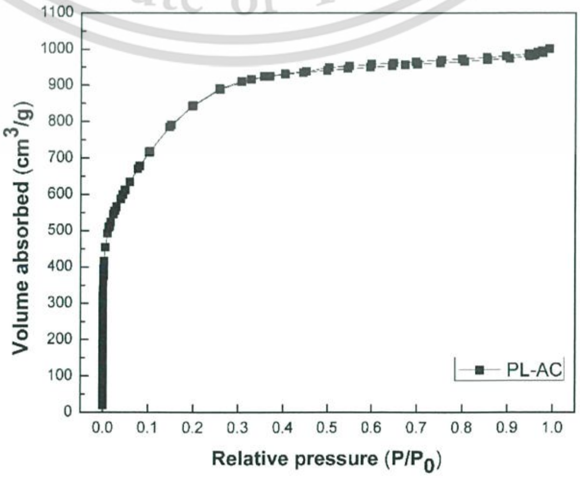

Figure 6.2 Nitrogen adsorption and desorption isotherm of PL-AC

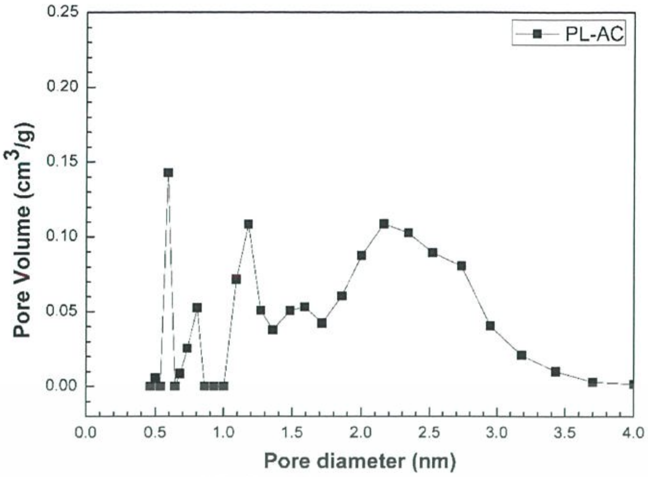

Figure 6.3 Pore size distribution of PL-AC

6.2.3 Chemical states of activated carbon

Fig. 6.4 and Fig. 6.5 show XPS spectra of O1s and N1s of PL-AC. The PL-AC shows the highest nitrogen content (2.3 at%) and the N/C ratio of 0.025. The O1s spectra can be deconvoluted divided into three different binding configurations, including O-C=O (533.5 eV), O-C-O/C-OH (532.2 eV), and C=O (531.2 eV) [88,89]. The N1s spectra can be deconvoluted divided into four binding contributions including pyridine N (N-6, 398.3 eV), pyrrolic N (N-5, 399.89 eV), quaternary N (N-Q, 401.3 eV), and oxidized pyridine N (N-X, 402.7 eV) [88–90]. The PL-AC shows the highest N-5, implying the pseudocapacitance property. Additionally, N-Q enhances the electronic conductivity and the N-X indicates the wettability properties. These results show that the PL-AC has the high specific capacitance, hierarchical porous structure (combination of micro-, meso- and macropores), numerous heteroatom (O and N) group, good electrical conductivity, and wettability properties, which are significant requirement of electrode materials for supercapacitor.

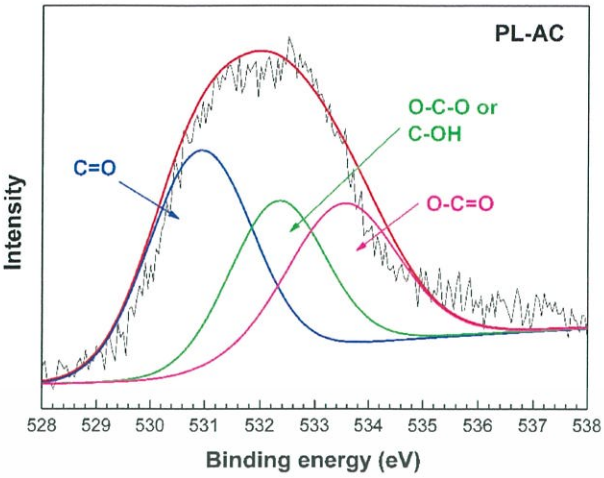

Figure 6.4 O1s XPS spectra of PL-AC

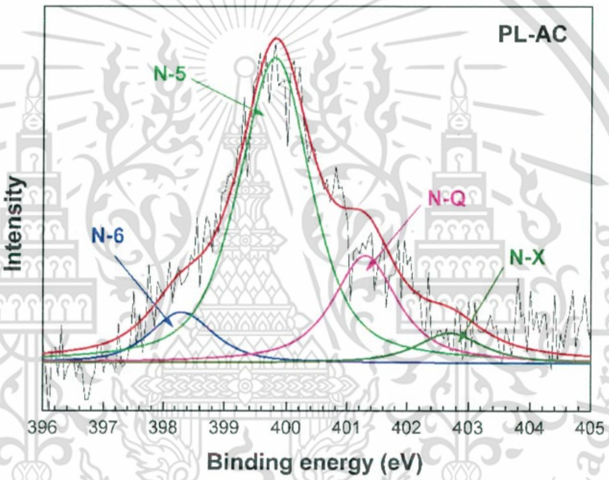

Figure 6.5 N1s XPS spectra of PL-AC

6.3 Characterization of electrochemical properties of activated carbon

6.3.1 Cyclic voltammetry of activated carbon

Cyclic voltammetry (CV) curves of different scan rates in aqueous electrolyte are shown in Fig. 6.6. From the CV curves, all scan rates show the quasi-rectangular shape, indicating the both of EDLC and pseudocapacitance behaviors.

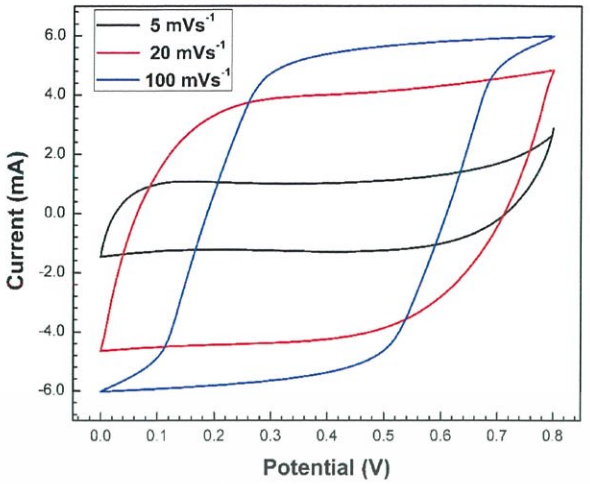

Figure 6.6 CV curves of PL-AC at different scan rates in 1 M Na_2SO_4 aqueous solution

6.3.2 Galvanostatic charge-discharge of activated carbon

The charge-discharge (CD) profiles of PL-AC was operated in potential window from 0.0 to 0.8 V at an applied constant current of 2 mA. Fig. 6.7 shows a symmetrical triangle shape of PL-AC, indicating the good electrochemical. The specific capacitance was calculated by equation (3.2). The specific capacitance of the PL-AC was approximately 68.94 Fg^{-1}. The excellent electrochemical property of the PL-AC is attributed to the high electrical capacitance owing to high surface area and the pseudocapacitive property derived from the nitrogen doping.

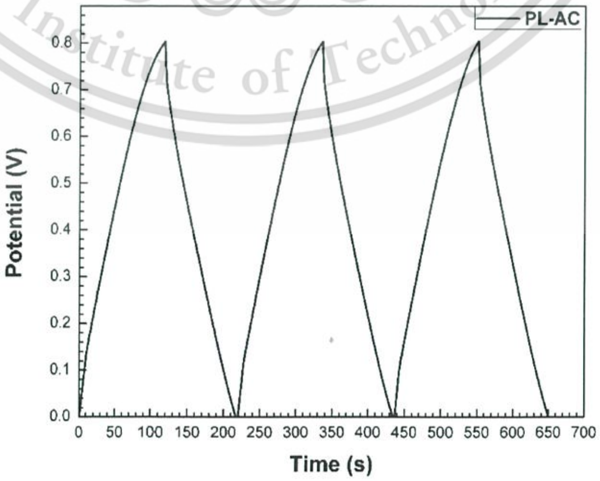

Figure 6.7 CD curves of PL-AC at an applied constant current of 2 mA in 1 M Na_2SO_4 aqueous solution

6.4 Summary

The activated carbon from the green leaves of PL was successfully synthesized. The PL-AC presents the high specific surface area (2664 m^2g^{-1}), hierarchical porous structure (1.27 cm^3g^{-1}), good conductivity and heteroatom doping, introducing to use as the electrode material for supercapacitor application. The PL-derived activated carbon can be used as the electrode materials for supercapacitor application with a specific capacitance of 68.94 Fg^{-1}. These results recommend that nitrogen-rich PL is potential precursors for the synthesis of nitrogen-doped activated carbon by one-step process.

CHAPTER 7

CONCLUSIONS AND PERSPECTIVES

7.1 Conclusions

Hybrid materials based on functionalized MWNT (f-MWNT) and manganese dioxide (MnO_2) nanosheet, and asymmetric supercapacitor (ASC) based on f-MWNT and MnO_2/f-MWNT were successfully fabricated. The energy density was increased by increasing in total capacitance and increasing in cell voltage. The summary of each part was summarized as follows:

The capacitance of supercapacitor was increased by functionalization of MWNT using microwave and oxygen plasma treatment. Functionalized MNWT exhibits the increasing of oxygen-containing functional group, surface area, and wettability property. Functionalized MWNT by using oxygen plasma (p-MWNT) shows the highest specific capacitance of 104.62 Fg^{-1}, an energy density of 9.30 $Whkg^{-1}$, a power density of 0.33 $kWkg^{-1}$ at a voltage window of 0.8 V. The specific capacitance of p-MWNT remains 99.13% after 1,000 CD cycles. The p-MWNT shows the highest specific capacitance and energy density with the 4.3-fold increasing compared to that of the pristine-MWNT. The capacitance improvement is attributed to the increase in the number of oxygen-containing functional groups, implying that oxygen plasma treatment is a rapid and efficient method for the modification of MWNTs.

The capacitance of supercapacitor was also increased by using hybrid materials based on MnO_2 nanosheet and f-MWNT (MnO_2/f-MWNT). The MnO_2/f-MWNT was optimized by varying synthesis times of MnO_2 nanosheet. The MnO_2/f-MWNTs at 15-min-deposited MnO_2-NS show the highest specific capacitance of 144.10 Fg^{-1} energy density of 12.80 $Whkg^{-1}$ and power density of 0.28 $kWkg^{-1}$ at the voltage window of 0.8 V. The MnO_2/f-MWNT shows the highest specific capacitance and energy density with the 5.8-fold increasing compared to that of pristine-MWNT. The high capacitance value is due to the combination of the MnO_2 nanosheet and the f-MWNT, resulting in the high surface, the low contact resistant between the electrode material and the current electrode, and the increase in total capacitance by the pseudocapacitive property from MnO_2 nanosheet and EDLC property from f-MWNT.

The voltage window of supercapacitor was increased by designing ASC based on f-MWNT and MnO_2/f-MWNT. For ASC assembly, a PTFE membrane was inserted between two electrodes and 1 M Na_2SO_4 was used an electrolyte at the voltage window of 2.0 V. The specific capacitance of ASC is 66.97 Fg^{-1}. The ASC shows an energy density of 37.21 $Whkg^{-1}$ at a power density of 4.11 $kWkg^{-1}$, indicating both considerable energy density and excellent power capability. The energy density of ASC was increased 17-fold with compared to pristine-MWNT. The ASC is an effective approach to enhance the energy density by increasing the operation voltage by utilizing the different potential windows of the two electrodes, and by increasing the specific capacitance by using hybrid materials. The electrochemical performance of each electrode materials is summarized in Table 8.1.

Table 7.1 Electrochemical performance of each electrode materials

Electrode material	Voltage window (V)	Specific capacitance (Fg^{-1})	Energy density ($Whkg^{-1}$)	Power density ($kWkg^{-1}$)
Pristine-MWNT	0.8	24.58	2.18	0.12
m-MWNT	0.8	85.76	7.62	0.31
p-MWNT	0.8	104.62	9.30	0.33
MnO_2/ f-MWNT	0.8	144.10	12.80	0.28
ASC	2.0	66.97	37.21	4.11

Finally, activated carbon was prepared by green leaves of papaya (PL-AC) as a precursor and its electrochemical properties were studied. The PL-AC shows the high specific surface area (2664 m^2g^{-1}), hierarchical porous structure (1.27 cm^3g^{-1}), good conductivity and heteroatom doping, suitable to use as the electrode material for supercapacitor application. The PL-derived activated carbon can be used as the electrode materials for supercapacitor application with a specific capacitance of 68.49

Fg^{-1}. These results recommend that nitrogen-rich PL is potential precursors for the synthesis of nitrogen-doped active carbon by one-step process.

7.2 Perspectives for future work

The findings from chapter 4 show that the increase in capacitance is achieved by the MnO_2 nanosheet and f-MWNT hybrid materials. However, the mechanisms of this hybrid materials have not been clearly elucidated yet. Thus, future study is proposed to realize the mechanism to maximize the potential use of hybrid materials.

7.2.1 Study on the morphology and porosity of hybrid materials

Supercapacitor performance based on MnO_2/f-MWNT hybrid materials were optimized by varying synthesis times of MnO_2 nanosheet at 10, 15 and 20 min Fig. 7.1 shows the SEM images of MnO_2/f-MWNT synthesized by different synthesis times. The morphologies of MnO_2 nanosheets were increased with increasing time to synthesize. These results be attributing to enhance specific surface area, which should be confirmed by BET.

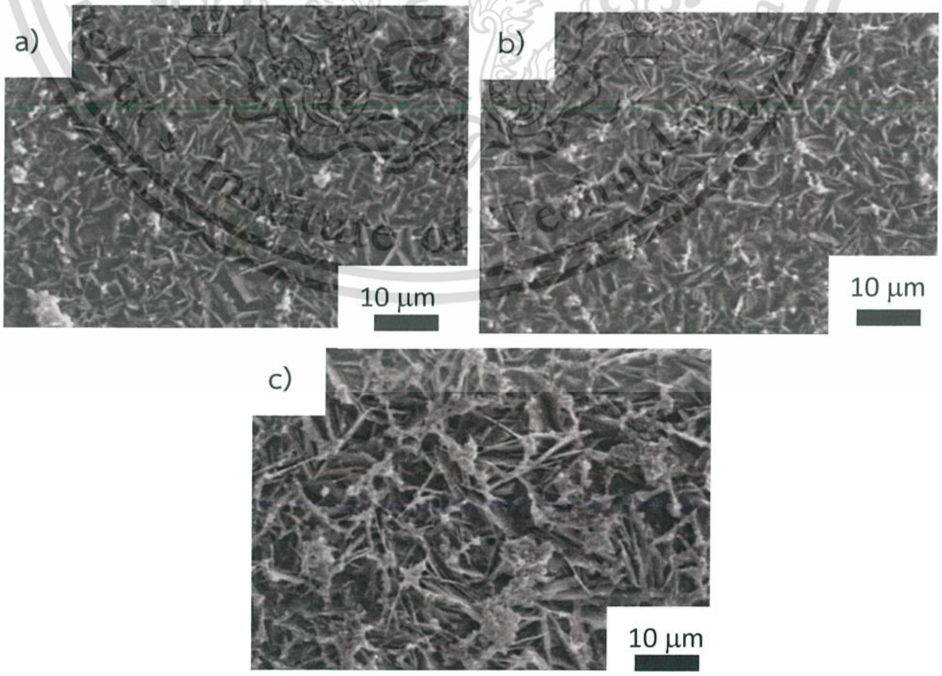

Figure 7.1 SEM images of MnO_2/f-MWNT synthesized by different synthesis times a) 10, b) 15 and c) 20 min

7.2.2 Study on effect of MnO2 phase on electrochemical properties

MnO_2 has many phase, such as α-, β-, γ-, and δ-MnO_2 types, which depend on the fabrication conditions [77,82]. These different crystallographic structures give different performance when used as supercapacitor electrode as indicated in Fig. 7.2. For example, it was reported that α- and δ-MnO_2 give higher capacitance, 241 and 236 Fg^{-1}, respectively, than the β- and γ- MnO_2, 9 and 107 Fg^{-1}, respectively. Generally, the reactivity of MnO_2 for electrochemical properties greatly depends on its crystal structure, while among different MnO_2 phases, the most reactive candidates are amorphous or nanocrystalline (α- and δ-MnO_2) and the least reactive one is β-MnO_2.

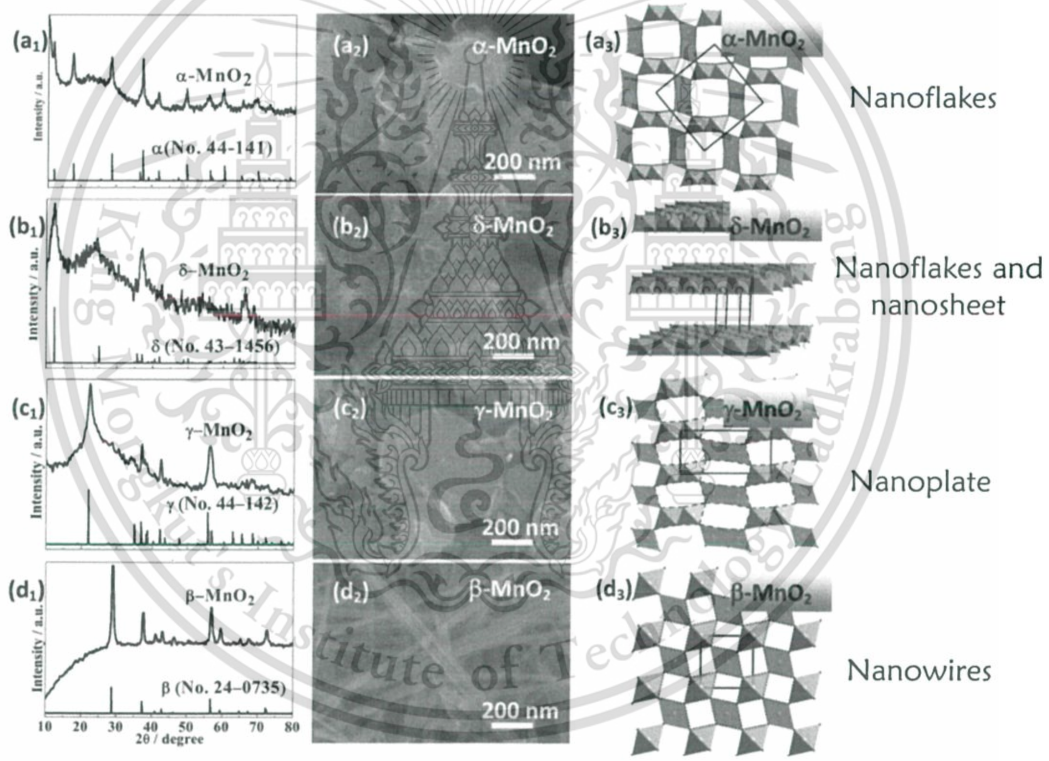

Figure 7.2 Structure characteristics of as-crystallized MnO_2 samples. XRD patterns of (a_1) α-MnO_2, (b_1) δ-MnO_2, (c_1) γ-MnO_2 and (d_1) β-MnO_2 as well as their corresponding SEM images (a_2-d_2) and crystallographic details (a_3-d_3) [82]

In this research, it was found that the synthesized MnO_2 nanosheet at 15 min had a mix phase of α-and δ-MnO_2 phases. The α-MnO_2 phase has a good electron transport, while the δ-MnO_2 phase has high external surface area and large reactive

active sites for fast charge transfer, which is favorable for the electrochemical reaction at electrode/electrolyte interface. Therefore, further study on structure of MnO_2 nanosheet synthesized by each condition should be conducted. The correlation between the hybrid material morphology, porosity, crystallization and their electrochemical properties should be discussed.

To realize the effect of MnO_2 phase on its electrochemical properties, it is a challenge to control phase of MnO_2, i.e. single phase, mixed phase with specified ratio, for example, a growth control by growth temperature.

7.2.3 Study on the hysteresis in cyclic voltammetry characteristics of hybrid materials

The information from cyclic voltammetry (CV) technique describes the electrochemical reaction between the surface of electrode materials and the electrolyte. The hysteresis of hybrid materials of each voltage window should be further discussed to realize the electrochemical reaction.

REFERENCES

1) C. Arbizzani, M. Mastragostino, and F. Soavi, **J. Power Sources** 100, 164 (2001).
2) J.R. Miller and P. Simon, **Science** (80-.). 321, 651 (2008).
3) R. Kötz, R. Kötz, M. Carlen, and M. Carlen, **Electrochim. Acta** 45, 2483 (2000).
4) A. Burke, **Electrochim. Acta** 53, 1083 (2007).
5) P. Simon and Y. Gogotsi, **Nat. Mater**. 7, 845 (2008).
6) A.G. Pandolfo and A.F. Hollenkamp, **J. Power Sources** 157, 11 (2006).
7) B.E. Conway, V. Birss, and J. Wojtowicz, **J. Power Sources** 66, 1 (1997).
8) C. Zhao and W. Zheng, Front. **Energy Res.** 3, 1 (2015).
9) R. Quintero, D.Y. Kim, K. Hasegawa, Y. Yamada, A. Yamada, and S. Noda, **RSC Adv**. 4, 8230 (2014).
10) M. Biswal, A. Banerjee, M. Deo, and S. Ogale, **Energy Environ. Sci**. 6, 1249 (2013).
11) B. Xu, Y. Chen, G. Wei, G. Cao, H. Zhang, and Y. Yang, Mater. **Chem. Phys.** 124, 504 (2010).
12) R. Wang, P. Wang, X. Yan, J. Lang, C. Peng, and Q. Xue, **ACS Appl. Mater. Interfaces** 4, 5800 (2012).
13) Y. Zhai, Y. Dou, D. Zhao, P.F. Fulvio, R.T. Mayes, and S. Dai, **Adv. Mater**. 23, 4828 (2011).
14) P. Dulyaseree, V. Yordsri, and W. Wongwiriyapan, **Jpn. J. Appl. Phys.** 55, 02BD05 (2016).
15) B.-J. Yoon, S.-H. Jeong, K.-H. Lee, H. Seok Kim, C. Gyung Park, and J. Hun Han, **Chem. Phys. Lett.** 388, 170 (2004).
16) R.K. Gupta, M. Dubey, P. Kharel, Z. Gu, and Q.H. Fan, **J. Power Sources** 274, 1300 (2015).
17) K. Wang, C. Li, and B. Ji, **J. Mater. Eng. Perform**. 23, 588 (2014).
18) C.-C. Lai and C.-T. Lo, **RSC Adv**. 5, 38868 (2015).
19) G.X. Wang, B.L. Zhang, Z.L. Yu, and M.Z. Qu, **Solid State Ionics** 176, 1169 (2005).
20) M. Zhi, C. Xiang, J. Li, M. Li, and N. Wu, **Nanoscale** 5, 72 (2013).
21) L. Li, Z.A. Hu, N. An, Y.Y. Yang, Z.M. Li, and H.Y. Wu, **J. Phys. Chem. C** 118, 22865 (2014).

22) C. Wang, F. Li, H. Qu, Y. Wang, X. Yi, Y. Qiu, Z. Zou, Y. Luo, and B. Yu, **Electrochim. Acta** 158, 35 (2015).

23) Y.T. Kim and T. Mitani, **J. Power Sources** 158, 1517 (2006).

24) V. Khomenko, E. Raymundo-Piñero, E. Frackowiak, and F. Béguin, Appl. **Phys. A Mater. Sci. Process.** 82, 567 (2006).

25) V.D. Patake, S.S. Joshi, C.D. Lokhande, and O.S. Joo, **Mater. Chem. Phys.** 114, 6 (2009).

26) I.-H. Kim, J.-H. Kim, B.-W. Cho, Y.-H. Lee, and K.-B. Kim, **J. Electrochem. Soc.** 153, A989 (2006).

27) C. Portet, P.L. Taberna, P. Simon, and C. Laberty-Robert, **Electrochim. Acta** 49, 905 (2004).

28) F. Wang, S. Xiao, Y. Hou, C. Hu, L. Liu, and Y. Wu, **RSC Adv.** 3, 13059 (2013).

29) Y. Jin, H. Chen, M. Chen, N. Liu, and Q. Li, **ACS Applied materials and interfaces** 5, 3408 (2013

30) X. Xiao, T. Li, Z. Peng, H. Jin, Q. Zhong, Q. Hu, B. Yao, Q. Luo, C. Zhang, L. Gong, J. Chen, Y. Gogotsi, and J. Zhou, Nano **Energy** 6, 1 (2014).

31) B. Vidyadharan, I.I. Misnon, J. Ismail, M.M. Yusoff, and R. Jose, **J. Alloys Compd.** 633, 22 (2015).

32) Wikipedia. 2017. **Ragone polt.** [online]. Available: https://en.wikipedai.org/wiki/Ragone_plot.

33) F. Beguin and E. Frackowiak, 2013 **Supercapacitors: Materials, Systems, and Applications.** Weinheim : Wiley-VCH.

34) P. Xu, K. Ye, M. Du, J. Liu, K. Cheng, J. Yin, G. Wang, and D. Cao, **RSC Adv.** 5, 36656 (2015).

35) M. Behpour, S.M. Ghoreishi, N. Soltani, and M. Salavati-Niasari, **Corros. Sci.** 51, 1073 (2009).

36) P.J. Hall, M. Mirzaeian, S.I. Fletcher, F.B. Sillars, A.J.R. Rennie, G.O. Shitta-Bey, G. Wilson, A. Cruden, and R. Carter, **Energy Environ. Sci.** 3, 1238 (2010).

37) J.R. Miller and P. Simon, **Science** (80-.). 321, 651 (2008).

38) M.N. Rahuma, **Am. J. Appl. Chem**. 2, 1 (2014).

39) A. Jain, V. Aravindan, S. Jayaraman, P.S. Kumar, R. Balasubramanian, S. Ramakrishna, S. Madhavi, and M.P. Srinivasan, **Sci. Rep.** 3, 1 (2013).

40) Y.-J. Ou, C. Peng, J.-W. Lang, D.-D. Zhu, and X.-B. Yan, Xinxing Tan **Cailiao/New**

Carbon Mater. 29, 209 (2014).

41) M. Fujishige, I. Yoshida, Y. Toya, Y. Banba, and K. Oshida, **Biochem. Pharmacol**. 5, 1801 (2017).

42) K.S. Sulaiman, A. Mat, and A.K. Arof, **Ionics** (Kiel). 22, 911 (2016).

43) Y. Liu, Y. Wang, G. Zhang, W. Liu, D. Wang, and Y. Dong, **Mater. Lett.** 176, 60 (2016).

44) Wikipedia. 2017. **Activated carbon.** [online]. Available: http://en.wikipedia.org /wiki/Activated_carbon

45) T.H. Niu C, Sichel E, Hoch R, Moy D, **Appl Phys Lett** 70, 1997 (1997).

46) K.H. An, W.S. Kim, Y.S. Park, Y.C. Choi, S.M. Lee, D.C. Chung, D.J. Bae, S.C. Lim, and Y.H. Lee, **Adv. Mater.** 13, 497 (2001).

47) K.H. An, W.S. Kim, Y.S. Park, J.M. Moon, D.J. Bae, S.C. Lim, Y.S. Lee, and Y.H. Lee, **Adv. Funtional Mater**. 11, 387 (2001).

48) Wikipedia. 2017. **Carbon nanotubes (Single- and multiwalled carbon nanotube).** [online]. Available: https://en.wikipedia.org/wiki/Carbon_nanotube.

49) Y. Wang, Z. Shi, Y. Huang, Y. Ma, C. Wang, M. Chen, and Y. Chen, **J. Phys. Chem**. C 113, 13103 (2009).

50) Wikipedia. 2017. **Graphene.** [online]. Available: http://en.wikipedia.org /wiki/Graphene.

51) A. Burke, **J. Power Sources** 91, 37 (2000).

52) S. Wen, J.W. Lee, I.H. Yeo, J. Park, and S. Il Mho, **Electrochim. Acta** 50, 849 (2004).

53) S. Wang, L.J. Ji, B. Wu, Q. Gong, Y. Zhu, and J. Liang, **Appl. Surf. Sci.** 255, 3263 (2008).

54) S.W. Zhang and G.Z. Chen, **Energy Mater**. 3, 186 (2008).

55) A. Singh and A. Chandra, **Sci. Rep**. 6, 1 (2016).

56) A. Singh and A. Chandra, **Sci. Rep**. 5, 1 (2015).

57) J. Chang, M. Jin, F. Yao, T.H. Kim, V.T. Le, H. Yue, F. Gunes, B. Li, A. Ghosh, S. Xie, and Y.H. Lee, **Adv. Funct. Mater**. 23, 5074 (2013).

58) I. Riess and C.G. Vayenas, **Solid State Ionics** 159, 313 (2003).

59) Wikipedia. 2017. **Transmission Electron Microscopy.** [online]. Available: https:// en.wikipedia.org/wiki/Transmission_electron_microscopy.

60) Wikipedia. 2017. **Scanning Electron Microscopy**. [online]. Available: https://en.

wikipedia.org/wiki/Scanning_electron_microscope.

61) Wikipedia. 2017. **Fourier Transform Infrared Spectroscopy**. [online]. Available: https://en.wikipedia.org/wiki/Fourier_transform_infrared_spectroscopy.

62) Wikipedia. 2017. **Raman Spectroscopy**. [online]. Available: https://en.wikipedia. org/wiki/Raman_spectroscopy

63) Wikipedia. 2017. **X-ray Crystallography.** [online]. Available: https://en.wikipedia. org/wiki/X-ray_crystallography.

64) Micrometrics ASAP 2020. **Nitrogen-adsorbtion isotherm.** [online]. Available: http://sites.udel.edu/amcl/micromertics-asap-2020.

65) Dataphysics OCA40 2017. **Contact angle.** [online]. Available: http://www.dataphysics.de/2/start/products/contact-angle-measuring-and-contour-analysis-systems/oca-measuring-instruments

66) Autolab PGSAT 302. **Electrochemical measurement.** [online]. http://www.metrohmautolab.com/Products/Echem/NSeriesFolder/PGSTAT302

67) M.S. Dresselhaus, G. Dresselhaus, R. Saito, and a. Jorio, **Phys. Rep.** 409, 47 (2005).

68) M.S. Dresselhaus, A. Jorio, M. Hofmann, G. Dresselhaus, and R. Saito, **Nano Lett.** 10, 751 (2010).

69) S. Tang, N. Lu, J.K. Wang, S.-K. Ryu, and H.-S. Choi, **J. Phys. Chem**. 111, 1820 (2007).

70) Z. Wang, Z. Wu, G. Di Benedetto, J.L. Zunino, and S. Mitra, **Carbon N. Y.** 91, 103 (2015).

71) J.H. Park, J.M. Ko, and O. Ok Park, **J. Electrochem. Soc**. 150, A864 (2003).

72) H. Zanin, E. Saito, H.J. Ceragioli, V. Baranauskas, and E.J. Corat, **Mater. Res. Bull**. 49, 487 (2014).

73) D.P. Dubal, R. Holze, and P. Gomez-Romero, **Sci. Rep.** 4, 7349 (2014).

74) P. Iamprasertkun, A. Krittayavathananon, A. Seubsai, N. Chanlek, P. Kidkhunthod, W. Sangthong, S. Maensiri, R. Yimnirun, S. Nilmoung, P. Pannopard, S. Ittisanronnachai, K. Kongpatpanich, J. Limtrakul, and M. Sawangphruk, **Sci. Rep**. 6, 1 (2016).

75) V.H. Nguyen, T.T. Nguyen, and J.J. Shim, **Synth. Met.** 199, 276 (2015).

76) W.H. Ho and S.K. Yen, **J. Electrochem. Soc**. 152, A506 (2005).

77) Z. Ma, G. Shao, Y. Fan, G. Wang, J. Song, and D. Shen, **ACS Appl. Mater.**

Interfaces 8, 9050 (2016).

78) Y. Sun, L. Wang, Y. Liu, and Y. Ren, **Small** 11, 300 (2015).

79) T.T. Truong, Y. Liu, Y. Ren, L. Trahey, and Y. Sun, **ACS Nano** 6, 8067 (2012).

80) B. Brown, I.A. Cordova, C.B. Parker, B.R. Stoner, and J.T. Glass, **Chem. Mater**. 27, 2430 (2015).

81) R.R. Salunkhe, H. Ahn, J.H. Kim, and Y. Yamauchi, **Nanotechnology** 26, 204004 (2015).

82) Y. Zhang, C. Sun, P. Lu, K. Li, S. Song, and D. Xue, **CrystEngComm** 14, 5892 (2012).

83) Y. Zhao, M. Lu, P. Tao, Y. Zhang, X. Gong, Z. Yang, G. Zhang, and H. Li, **J. Power Sources** 307, 391 (2016).

84) X. Cai, R. V. Hansen, L. Zhang, B. Li, C.K. Poh, S.H. Lim, L. Chen, J. Yang, L. Lai, J. Lin, and Z. Shen, **J. Mater. Chem.** A 3, 22043 (2015).

85) P.C. Gao, A.H. Lu, and W.C. Li, **J. Power Sources** 196, 4095 (2011).

86) M. Thommes, K. Kaneko, A. V. Neimark, J.P. Olivier, F. Rodriguez-Reinoso, J. Rouquerol, and K.S.W. Sing, **Pure Appl. Chem**. 87, 1051 (2015).

87) X. Ying, C. Chen, Z. Jie, D. Hua, X. Deng, and J. Wei, **J. Power Sources** 230, 50 (2013).

88) B.D. Hulicova-jurcakova, M. Seredych, G.Q. Lu, and J. Bandosz, **Advanced functional materials** 19, 438 (2009).

89) R. Arrigo, M. Ha, S. Wrabetz, R. Blume, M. Lerch, J. Mcgregor, E.P.J. Parrott, J.A. Zeitler, L.F. Gladden, A. Knop-gericke, and R. Schlo, **J. American chemical socity** 132, 9616 (2010)

90) M. Zhou, F. Pu, Z. Wang, and S. Guan, **Carbon N. Y**. 68, 185 (2013).

AUTHOR BIOGRAPHY

Name-Surname	Miss Paweena Dulyaseree
Date of Birth	February 07, 1987
Present Address	41 Muslimbomrung Rd., Tambol Sateng, Amphoe Mueang, Yala Province 95000 Thailand

Education

2005-2009	Bachelor of Science (Applied Physics), King Mongkut's Institute of Technology Ladkrabang, Thailand
2011-2017	Master of Science (MSc.) and Doctor of Philosophy (Ph.D.) in Nanoscience and Nanotechnology, College of Nanotechnology, King Mongkut's Institute of Technology Ladkrabang, Thailand

Work Experience

2009-2011	Laboratory Officer, Thai Microelectronics Center (TMEC), National Electronics and Computer Technology Center (NECTEC), National Science and Technology Development Agency (NSTDA)

Recent/relevant publications:

(1) Paweena Dulyaseree, Masatsugu Fujishige, Ichiro Yoshida, Yumiko Toya, Yasuo Banba, Yu-suke Tanaka, Takaaki Aoyama, Mayuree Phonyiem, Winadda

Wongwiriyapan, Kenji Takeuchi, Morinobu Endo

“Nitrogen-rich green leaves of papaya and *Coccinia grandis* as precursors of activated carbon and their electrochemical properties”

RSC Advances, 7 (2017), 4264-4272

(2) Songsak Rattanamai, Paweena Dulyaseree, Thantumrong Wanchaem, Winadda Wongwiriyapan

“Optimized manganese oxide nanosheet/manganese oxide thin film/ multiwalled carbon nanotubes as hybrid electrode materials for supercapacitors”

Materials Today: Proceedings, 4 (2017) 6404-6409

(3) Masatsugu Fujishige, Ichiro Yoshida, Yumiko Toya, Yasuo Banba, Yu-suke Tanaka, Paweena Dulyaseree, Winadda Wongwiriyapan, Kenji Takeuchi

“Preparation of activated carbon from bamboo-cellulose fiber and its use for EDLC electrode material”

Journal of Environmental Chemical Engineering, 5(2) (2017), 1801–1808

(4) Thantumrong Wanchaem, Songsak Rattanamai, Paweena Dulyaseree, Wirat Jarernboon, Winadda Wongwiriyapan

“Electrodeposition of Manganese Oxide Nanosheets as Supercapacitor Electrode Materials”

Key Engineering Materials, 675-676 (2016), 273-276

(5) Paweena Dulyaseree, Visittapong Yordsri, Winadda Wongwiriyapan

“Effects of microwave and oxygen plasma treatments on capacitive characteristics of supercapacitor based on multiwalled carbon nanotubes”

Japanese Journal of Applied Physics, 55 (2016), 02BD05

(6) Paweena Dulyaseree, Wirat Jarernboon, Winadda Wongwiriyapan

“Supercapacitor based on multi-walled carbon nanotubes/carbon black composites-coated wooden sheet”

Energy Procedia, 56 (2014), 481–486

Honors & Award:

1. The M.Sc.scholarship: Thailand Center of Excellence in Physics, 2011-2013
2. The Ph.D. scholarship: The Strategic Scholarships Fellowships Frontier Research Networks (Specific for Southern region) from the Office of the Higher Education Commission (OHEC), 2013-2017
3. Research scholarship:
   - The Strategic Scholarships Fellowships Frontier Research Networks under project “Synthesis of activated carbon from Thailand agricultural wastes and its supercapacitor application” August 1, 2016 - April, 28, 2017 at Shinshu University, Nagano, Japan
   - New Energy and Industrial Technology Development Organization (NEDO) under project “Study on structure and its electric properties of nanocarbon

materials by transmission electron microscopy" October 21, 2013 - November 9, 2013 at Shinshu University, Nagano, Japan

4. Third honor award for poster presentation: The 7th Annual Conference of the Thai Physics Society (SPC2012, May 9-12, 2012) under entitle of "Facile Growth of Carbon Nanofibers and Carbon Nanotubes on Stainless Steel Sheet"

Japanese Journal of Applied Physics **55**, 02BD05 (2016)
http://doi.org/10.7567/JJAP.55.02BD05

REGULAR PAPER

Effects of microwave and oxygen plasma treatments on capacitive characteristics of supercapacitor based on multiwalled carbon nanotubes

Paweena Dulyaseree[1], Visittapong Yordsri[2], and Winadda Wongwiriyapan[1,3,4*]

[1]*College of Nanotechnology, King Mongkut's Institute of Technology Ladkrabang, Bangkok 10520, Thailand*
[2]*National Metal and Materials Technology Center, Pathunthani 12120, Thailand*
[3]*Nanotec-KMITL Center of Excellence on Nanoelectronics Device, Bangkok 10520, Thailand*
[4]*Thailand Center of Excellence in Physics, CHE, Bangkok 10400, Thailand*

*E-mail: kwwinadd@kmitl.ac.th

Received July 1, 2015; accepted October 7, 2015; published online January 26, 2016

The effects of microwave and oxygen plasma treatments on the capacitive characteristics of a supercapacitor based on multiwalled carbon nanotubes (MWNTs) were investigated. MWNTs were heat-treated under air ambient at 500 °C for 1 h, and subsequently microwave-treated at 650 W for 70 s (m-MWNTs). Another batch of MWNTs was treated by oxygen plasma for 30 min (p-MWNTs). Pristine MWNTs, m-MWNTs, and p-MWNTs were separately used as electrode materials for supercapacitors. Their cyclic voltammetry, galvanostatic charge/discharge, and electrochemical impedance spectroscopy results were analyzed. The p-MWNTs show the best performance with a specific capacitance of 238.23 $F\cdot g^{-1}$. The capacitance improvement is attributed to the increase in the number of oxygen-containing functional groups, as evidenced by Fourier transform-infrared spectroscopy and contact angle measurement. These results suggest that oxygen plasma treatment is a rapid and efficient method for oxygen functionalization. © 2016 The Japan Society of Applied Physics

1. Introduction

A supercapacitor, also called an electrochemical capacitor, is a kind of electrical device for energy storage, bridging the gap between batteries and dielectric capacitors. Supercapacitors have gained considerable attention in recent years as an energy storage device owing to their high power density, high rates of charge/discharge, and long cycle life.[1–5] Supercapacitors are classified as electrical double-layer capacitors (EDLCs) and pseudocapacitors according to charge storage mechanisms.[3] The typical electrode materials of EDLCs are carbon materials with a high surface area, which can store energy in the double layers on the surface of carbon materials.[6] In the case of pseudocapacitors, the most commonly used electrode materials are metal oxides and conducing polymers, which can transfer the faradaic charges between an electrode and an electrolyte.[7]

An EDLC consists of three important parts: an electrode, a separator, and an electrolyte. To improve the performance of EDLCs, most efforts have been focused on the improvement of electrode materials. Electrode materials are required to have high specific surface area, good conductivity, and good chemical stability properties.[8,9] Various different carbon forms can be used as materials in an EDLC electrode such as activated carbon, carbon aerogels, carbon nanotubes (multi- and single-walled carbon nanotubes), and graphene.[10] An EDLC based on carbon nanotube materials exhibited good electrical performance.[11] Recently, substantial efforts have been expended to improving the electrochemical performance of carbon-based electrodes through modifying the surface of carbon materials by, for example, functionalization with various metal oxides or a conductive polymer, or by treatment with plasma.[12–20] Functionalization of the electrode material surface with oxygen-containing functional groups is key to the enhancement of supercapacitor performance.[21–26] Since the pristine carbon surface is hydrophobic, the high resistance between the carbon surface and the aqueous electrolyte hinders the accessibility of the electrolyte ions into the carbon materials.[15,26,27]

In this study, we tailored the carbon-based materials by surface modification using low-cost equipment with rapid time and efficiency. The multiwalled carbon nanotube (MWNT) functionalization by microwave treatment using a commercial microwave oven and oxygen plasma treatment using a commercial oxygen plasma cleaner were investigated. The electrochemical characteristics of the surface-modified MWNTs were evaluated.

2. Experimental methods

Three types of MWNT-based electrodes were prepared: pristine MWNTs, microwave-treated MWNTs (m-MWNTs), and plasma-treated MWNTs (p-MWNTs). For microwave treatment, 2.5 g of MWNTs (diameter, 10–20 nm; length, 1–5 μm) was treated by heating under air ambient at 500 °C for 1 h and subsequently treated with microwave in air at 650 W for 70 s (hereinafter referred to as m-MWNTs) using a commercial microwave oven. For plasma treatment, 0.55 g of MWNTs was treated with oxygen plasma using an expanded plasma cleaner (Harrick Scientific) at an RF frequency of 13.56 MHz and a power of 18 W for 30 min (hereinafter referred to as p-MWNTs). Next, the MWNT paste was prepared by mixing the treated MWNTs and poly(vinylidene fluoride) (PVDF) at a weight ratio of 11 : 1 in *n*-methyl-2-pyrrolidone (NMP) using a homogenizer at 7,000 rpm for 30 min and subsequently sonicated in an ultrasonic bath for 30 min. To fabricate MWNT-based electrodes for a supercapacitor, stainless-steel-type 304 (SS304) was used as a current collector. SS304 was cleaned by soaking in 37% hydrochloric acid (HCl) for 10 min and washed with deionized water to remove residual HCl solution until its pH became neutral. The prepared MWNT paste was dip-coated on the treated SS304 with an area of $5 \times 5\,mm^2$ and dried at room temperature overnight. The weight of the treated MWNT coating on SS304 was measured by weighing the SS304 before and after coating using a digital balance. The treated MWNTs were characterized in terms of their functional groups and structures by Fourier transform-infrared spectroscopy (FT-IR; Thermo Scientific Nicolet

6700), Raman spectroscopy (Thermo Scientific DXR Smart Raman), and transmission electron microscopy (TEM; JEOL JEM-2010). The hydrophilicity property of the treated MWNTs was characterized by the contact angle technique (Dataphysics OCA 40). A droplet of 1 M Na_2SO_4 aqueous solution (a volume of 1 µl) was dropped on the treated-MWNT-coated SS304.

Electrochemical measurements of the treated MWNTs were carried out in a three-electrode cell connected to an electrochemical workstation (Metrohm AUTOLAB PGSTAT 302). The treated-MWNT-based SS304 was used as a working electrode. The Pt and Ag/AgCl electrodes were used as the counting and reference electrodes, respectively. 1 M Na_2SO_4 aqueous solution was used as the electrolyte. Electrochemical properties were characterized by cyclic voltammetry (CV), galvanostatic charge/discharge (CD), and electrochemical impedance spectroscopy (EIS) techniques. CV tests were operated in a potential range of 0.0 to 0.8 V at scan rates of 5 and 100 $mV{\cdot}s^{-1}$. CD tests were carried out in a potential range of −0.2 to 1.0 V at a constant current of 1 mA. EIS was carried out in a frequency range between 10 kHz and 0.01 Hz at an amplitude of 5 mV. The specific capacitances of the supercapacitor (C_S) were evaluated from CV and CD curves using the following equations:

$$C_S = \frac{\int_{V_1}^{V_2} i(V)\,dV}{2(V_2 - V_1)m\upsilon}, \qquad (1)$$

$$C_S = \frac{I \times \Delta t}{\Delta V \times m}. \qquad (2)$$

where $\int_{V_1}^{V_2} i(V)\,dV$ is the total voltammetric charge obtained by the integration of positive and negative sweeps in the CV curve, $V_2 - V_1$ is the potential window width (V), m is the weight of the treated MWNTs in the electrode paste (g), υ is the scan rate ($V{\cdot}s^{-1}$), I is the discharge current (A), Δt is the discharge time (s), and ΔV represents the voltage change after a full charge or discharge (V).

3. Results and discussion

The changes in surface functional groups of pristine MWNTs after microwave and oxygen plasma treatments were confirmed from FTIR spectra through the changes in peak positions as well as the appearance of new peaks. Figure 1(a) shows comparative FT-IR spectra of the pristine MWNTs, m-MWNTs, and p-MWNTs with several peaks of functional groups. The broad peak at 3432 cm^{-1} corresponds to the stretching vibration of the hydroxyl group (–OH). The bands at 2922 and 2856 cm^{-1} are attributed to the C–H stretching vibrations of the methyl group. The peak at 2360 cm^{-1} could be assigned to CO_2 that was absorbed during the FTIR spectra measurements. The absorption bands at 1750, 1640, and 1596 cm^{-1} are assigned to the stretching vibrations of the carboxyl, carbonyl (C=O), and aromatic rings (C=C), respectively.[28] The band at 1020 cm^{-1} is assigned to the stretching vibration of the C–O group. Moreover, the new peaks at 3742 cm^{-1} corresponding to the –OH stretching of the hydroxyl group apparently appeared from p-MWNTs, while a small peak appeared for the m-MWNTs. Interestingly, focusing at the peaks at 1640 and 1596 cm^{-1}, the aromatic ring stretching was largely suppressed and the carbonyl stretching was enhanced in the m-MWNTs and p-MWNTs. These results indicate that oxygen plasma and microwave treatments are effective methods for functionalizing oxygen-containing functional groups on the walls of MWNTs. However, the chemical bonds between oxygen and carbon on the MWNT sidewall require further confirmation by X-ray photoelectron spectroscopy.

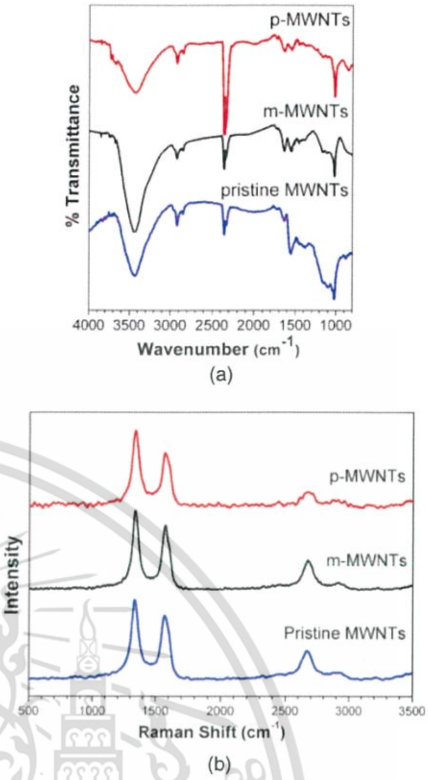

Fig. 1. (Color online) (a) FT-IR and (b) Raman spectra of the different electrode materials.

The purity and crystallinity of MWNTs were characterized by Raman spectroscopy using an argon ion laser with a wavelength of 532 nm (2.33 eV) as an excitation light at a power of 5 mW. As shown in Fig. 1(b), the Raman spectra of pristine MWNTs, m-MWNTs, and p-MWNTs consist of two characteristic peaks, which are the so-called D-band, which originated from the disordered carbon structure and sp^3 hybridized carbon at a Raman shift of ~1336 cm^{-1}, and the G-band, which originated from the graphitic structure dominated by sp^2 bonds at a Raman shift of ~1567 cm^{-1}.[29,30] Generally, the purity and crystallinity of MWNTs can be evaluated on the basis of the I_D/I_G ratio between the intensities of D and G bands. An increase in I_D/I_G ratio indicates the impurity structure and a higher proportion of sp^3 carbon.[30,31] It is found that the I_D/I_G ratio increased after MWNT treatments, i.e., the I_D/I_G ratios were 1.22, 1.26, and 1.41 for pristine MWNTs, m-MWNTs, and p-MWNTs, respectively. This result implies that oxygen plasma could etch sp^2 carbon faster than sp^3 carbon.[19]

The nanostructure of MWNTs was investigated by TEM. Figures 2(a)–2(c) show TEM images of pristine MWNTs,

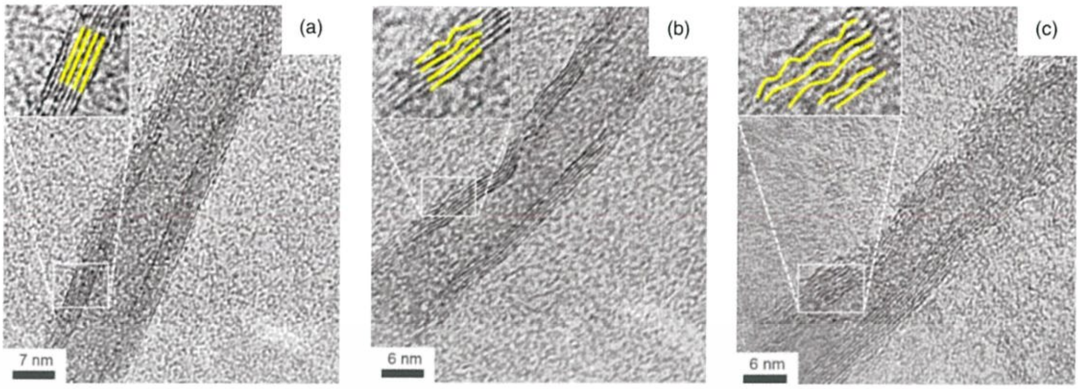

Fig. 2. (Color online) TEM images of (a) pristine MWNTs, (b) m-MWNTs, and (c) p-MWNTs.

m-MWNTs, and p-MWNTs, respectively. Figure 2(a) shows graphene planes parallel to each other and parallel to the axis of the tubular structure, implying an MWNT structure, illustrating as straight lines in the inset. As can be observed in Fig. 2(b), the m-MWNTs had partly damaged sidewalls, illustrated as curved lines in the inset. The damage on sidewalls was significantly increased in p-MWNTs [see Fig. 2(c)]. However, it was found that only the outer walls of MWNTs were damaged owing to defect generation, while the inner walls of MWNTs still remained intact. The TEM results coincided with the I_D/I_G of Raman spectra, which indicates the purity and crystallinity of MWNTs.

Next, the contact angle (CA) measurements were conducted to characterize the wettability of the substrate. CA can define the wettability degree, on the basis of which the surface is classified as superhydrophilic (CA < 5°), hydrophilic (CA < 90°), hydrophobic (CA > 90°), or superhydrophobic (CA > 150°).[32] Figures 3(a)–3(c) show the droplet of 1 μL of 1 M Na_2SO_4 aqueous solution on pristine-MWNT-, m-MWNT-, and p-MWNT-coated SS304 substrates, respectively. The contact angles of the pristine MWNTs, m-MWNTs and p-MWNTs are approximately 113.84 ± 4.15, 36.48 ± 8.69, and $19.87 \pm 5.05°$, respectively. The p-MWNTs show low contact angles, implying the best hydrophilicity property. The improved wettability of the p-MWNT-coated SS304 was attributed to the oxygenated functional group functionalization and the surface roughness of MWNTs owing to the defects as evidenced by FT-IR and TEM results.

Figure 4(a) shows CV curves of pristine MWNTs, m-MWNTs, and p-MWNTs in a potential window of 0 to 0.8 V at a scan rate of $100\,\mathrm{mV{\cdot}s^{-1}}$. The CV curves showed typical EDLC characteristics and are rectangular with no obvious redox peak. The clear rectangular curves further reflect a higher ion diffusion rate in the electrode materials. From the area of the CV curve, the specific capacitances were calculated using Eq. (1). The specified capacitances of the pristine MWNTs, m-MWNTs, and p-MWNTs were 61.46, 214.45, and $238.23\,\mathrm{F{\cdot}g^{-1}}$, respectively. The p-MWNTs show the highest specific capacitance. Generally, pristine MWNTs are hydrophobic materials due to the sp^2 lattice of graphitic carbon. In the case of using pristine MWNTs as the electrode material in an aqueous electrolyte system, the high resistance between the carbon surface and the aqueous electrolyte hinders the accessibility of the electrolyte ions into the electrode materials. In this study, microwave and oxygen plasma treatments facilitate the easy control of the wetting properties of m-MWNTs and p-MWNTs as evidenced by the decrease in contact angle. Thus, the m-MWNTs and p-MWNTs allow electrolyte ions to access to their surface more easily than the pristine-MWNTs, resulting in an increase in capacitance.[15,33] Figure 4(b) shows the galvanostatic charge–discharge (CD) curves within the operating voltage range of −0.2 to 1 V at a current of 1 mA. The CD profiles show a shape of a nearly isosceles triangle, suggesting good electrochemical reversibility. No obvious voltage drop was observed at the discharge current, indicating a low internal resistance of the electrode.[34]

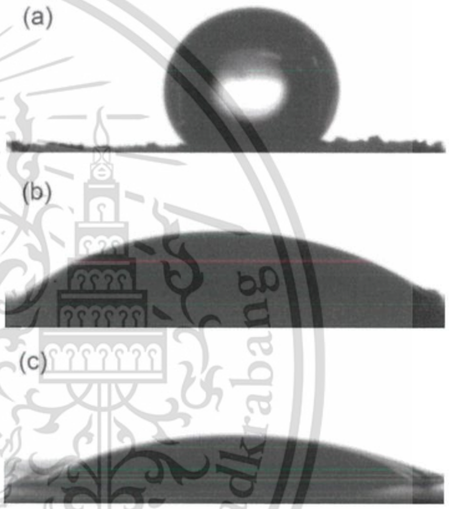

Fig. 3. Contact angles of (a) pristine MWNTs, (b) m-MWNTs, and (c) p-MWNTs.

The resistance and capacitance of supercapacitors can be further explained by electrochemical impedance spectroscopy (EIS). EIS is a technique that can reveal the complex phenomena of electron interception and diffusion at the

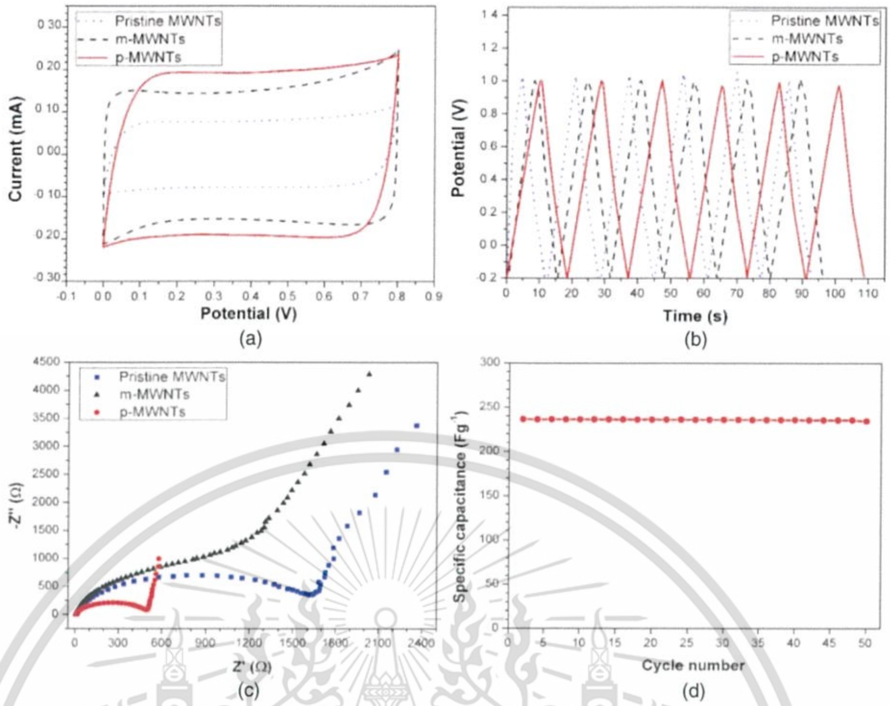

Fig. 4. (Color online) Electrochemical properties of different electrode materials in 1 M Na_2SO_4 aqueous electrolyte. (a) CV at a scan rate of 0.1 $V{\cdot}s^{-1}$, (b) galvanostatic charge/discharge curves at an applied constant current of 1 mA, (c) Nyquist plot in the frequency range of 10 kHz–0.01 Hz at an amplitude of 5 mV, and (d) cycling stability of p-MWNTs.

electrode–electrolyte interface. Figure 4(c) shows the Nyquist plots of the pristine MWNTs, m-MWNTs, and p-MWNTs in the frequency range of 10 kHz–0.01 Hz. The obtained Nyquist spectra for all the configurations consist of a semicircle in the high-frequency region, followed by a linear portion extending in the low-frequency regions. The slopes of the lines in the low-frequency regions ranging from highest to lowest correspond to the p-MWNTs, m-MWNTs, and pristine MWNTs, respectively. The p-MWNTs show a straight line with a slope near unity, indicating the highest ion diffusion rate at the interface between the electrolyte and electrode materials, and suggesting an ideal supercapacitive behavior. This high ion diffusion rate could be attributed to the wettability improvement of the electrode surface by the functionalization of the oxygen-containing functional group by plasma treatment.[18] The wettability of the electrode promotes the movement of Na^+ and SO_4^{2-} in the electrolyte penetrating deeply inside the micropores. The microwave-treated sample (m-MWNTs) shows a slight improvement in wettability.

The offset on the *x*-axis, Z' (Ω), of the high-frequency semicircle [see Fig. 4(c)] is a dominant resistive nature of the supercapacitor consisting of (i) electrolyte resistance, (ii) the intrinsic resistance of the electrode material, and (iii) the contact resistance between the electrode material and the current collector, which is a measure of series resistance, R_S.[35] The R_S values of the pristine MWNTs, m-MWNTs, and p-MWNTs are determined to be 4.99, 4.87, and 4.18 Ω, respectively. Since the same electrolyte, 1 M Na_2SO_4, was used in the EIS measurement, a decrease in the R_S of the treated MWNTs may be attributed to a decrease in the intrinsic resistance of the treated MWNTs due to the formation of intershell cross-linking by the oxygen-containing functional group,[36,37] and a decrease in contact resistance between the electrode material and the current collector due to the improvement of the wettability property.

The diameter of the semicircle represents the kinetic resistance to the charge transfer, called the charge transfer resistance (R_{CT}). The p-MWNTs show the smallest semicircle, implying the smallest R_{CT}, while the pristine MWNTs show the largest semicircle and thus the highest R_{CT}. This result indicates the good charge transfer in the electrolyte–electrode interface, which is due to the improvements in the conductivity and wettability of the treated MWNTs. Note that the EIS-measured impedance included contributions from both the MWNT-based electrodes and the electrolyte. The supercapacitor fabrication process was kept the same; only the MWNTs differed owing to the treatment process. Therefore, the measured Re(Z) values reflected the effects of only the properties and morphologies of the treated MWNTs.

Figure 4(d) shows the specific performance vs the number of CV cycles for the p-MWNT-based supercapacitor. The specific capacitance of p-MWNTs changes from 236.63 to 234.57 $F{\cdot}g^{-1}$ (remains 99.13%) after 50 cycles at the scan rate of 100 $mV{\cdot}s^{-1}$. Although the p-MWNTs may seem to deteriorate easily, they still show good stability with good retention of capacitance, showing a promising use as energy storage devices.

4. Conclusions

The effects of microwave and oxygen plasma treatments on the capacitive characteristics of a supercapacitor based on MWNTs were investigated. FT-IR, Raman spectroscopy, TEM, and contact angle measurement indicated that the hydroxyl functional groups were introduced, the surface morphology of the MWNTs was changed, and the wettability property was improved after oxygen plasma treatment. The electrochemical measurement reveals that MWNTs modified by oxygen plasma show the highest specific capacitance of $238.23\,\mathrm{F{\cdot}g^{-1}}$. Moreover, R_S is reduced to $4.18\,\Omega$ and the specific capacitance can be maintained at 99.13% after 50 cycles. The capacitance improvement is attributed to the increase in the number of oxygen-containing functional groups, suggesting that oxygen plasma treatment is a rapid and efficient method for the modification of MWNTs. These preliminary results suggest that the p-MWNTs are a promising electrode material for EDLC application.

Acknowledgments

We acknowledge the support from the KMITL Research Fund (KREF045508) and support from the National Nanotechnology Center (NANOTEC), NSTDA, Ministry of Science and Technology, Thailand, through its program of the Center of Excellence Network and the Thailand Center of Excellence in Physics (ThEP). P.D. acknowledges the support from the Office of the Higher Education Commission (OHEC).

---

1) C. Arbizzani, M. Mastragostino, and F. Soavi, J. Power Sources **100**, 164 (2001).
2) J. R. Miller and P. Simon, Science **321**, 651 (2008).
3) R. Kötz and M. Carlen, Electrochim. Acta **45**, 2483 (2000).
4) A. Burke, Electrochim. Acta **53**, 1083 (2007).
5) P. Simon and Y. Gogotsi, Nat. Mater. **7**, 845 (2008).
6) A. G. Pandolfo and A. F. Hollenkamp, J. Power Sources **157**, 11 (2006).
7) B. E. Conway, V. Birss, and J. Wojtowicz, J. Power Sources **66**, 1 (1997).
8) J. R. Miller, R. A. Outlaw, and B. C. Holloway, Science **329**, 1637 (2010).
9) Y. Zhu, S. Murali, M. D. Stoller, K. J. Ganesh, W. Cai, P. J. Ferreira, A. Pirkle, R. M. Wallace, K. A. Cychosz, M. Thommes, D. Su, E. A. Stach, and R. S. Ruoff, Science **332**, 1537 (2011).
10) F. Beguin and E. Frackowiak, *Supercapacitors: Materials, Systems, and Applications* (Wiley-VCH, Weinheim, 2013) p. 135.
11) Y. Zhai, Y. Dou, D. Zhao, P. F. Fulvio, R. T. Mayes, and S. Dai, Adv. Mater. **23**, 4828 (2011).
12) Y. Jin, H. Chen, M. Chen, N. Liu, and Q. Li, ACS Appl. Mater. Interfaces **5**, 3408 (2013).
13) L. Li, Z. A. Hu, N. An, Y. Y. Yang, Z. M. Li, and H. Y. Wu, J. Phys. Chem. C **118**, 22865 (2014).
14) C. C. Wang and C. C. Hu, Mater. Chem. Phys. **83**, 289 (2004).
15) J. H. Park, J. M. Ko, and O. O. Park, J. Electrochem. Soc. **150**, A864 (2003).
16) Q. Wu, Y. Xu, Z. Yao, A. Liu, and G. Shi, ACS Nano **4**, 1963 (2010).
17) C. C. Lai and C. T. Lo, RSC Adv. **5**, 38868 (2015).
18) K. Wang, C. Li, and B. Ji, J. Mater. Eng. Performance **23**, 588 (2014).
19) R. K. Gupta, M. Dubey, P. Kharel, Z. Gu, and Q. H. Fan, J. Power Sources **274**, 1300 (2015).
20) B. J. Yoon, S. H. Jeong, K. H. Lee, H. S. Kim, C. G. Park, and J. H. Han, Chem. Phys. Lett. **388**, 170 (2004).
21) R. L. McCreery, K. K. Cline, C. A. McDermott, and M. T. McDermott, Colloids Surf. **93**, 211 (1994).
22) E. Frackowiak, K. Metenier, V. Bertagna, and F. Beguin, Appl. Phys. Lett. **77**, 2421 (2000).
23) Y. T. Kim, Y. Ito, K. Tadai, T. Mitani, U. S. Kim, H. S. Kim, and B. W. Cho, Appl. Phys. Lett. **87**, 234106 (2005).
24) S. Ghosh, X. An, R. Shah, D. Rawat, B. Dave, S. Kar, and S. Talapatra, J. Phys. Chem. C **116**, 20688 (2012).
25) X. Xiao, T. Li, Z. Peng, H. Jin, Q. Zhong, Q. Hu, B. Yao, Q. Luo, C. Zhang, L. Gong, J. Chen, Y. Gogotsi, and J. Zhou, Nano Energy **6**, 1 (2014).
26) S. Deheryan, D. J. Cott, P. W. Mertens, M. Heyns, and P. M. Vereecken, Electrochim. Acta **132**, 574 (2014).
27) E. Dujardin, T. W. Ebbesen, H. Hiura, and K. Tanigaki, Science **265**, 1850 (1994).
28) Y. T. Kim and T. Mitani, J. Power Sources **158**, 1517 (2006).
29) M. S. Dresselhaus, G. Dresselhaus, R. Saito, and A. Jorio, Phys. Rep. **409**, 47 (2005).
30) M. S. Dresselhaus, A. Jorio, M. Hofmann, G. Dresselhaus, and R. Saito, Nano Lett. **10**, 751 (2010).
31) C. Chen, A. Ogino, X. Wang, and M. Nagatsu, Diamond Relat. Mater. **20**, 153 (2011).
32) A. O. Lobo, S. C. Ramos, E. F. Antunes, F. R. Marciano, V. J. Trava-Airoldi, and E. J. Corat, Mater. Lett. **70**, 89 (2012).
33) H. Zanin, E. Saito, H. J. Ceragioli, V. Baranauskas, and E. J. Corat, Mater. Res. Bull. **49**, 487 (2014).
34) D. P. Dubal, R. Holze, and P. Gomez-Romero, Sci. Rep. **4**, 7349 (2014).
35) B. Vidyadharan, I. I. Misnon, J. Ismail, M. M. Yusoff, and R. Jose, J. Alloys Compd. **633**, 22 (2015).
36) S. Agrawal, M. S. Raghuveer, H. Li, and G. Ramanath, Appl. Phys. Lett. **90**, 193104 (2007).
37) S. Lee and J. W. Peng, J. Phys. Chem. Solids **72**, 1101 (2011).

ROYAL SOCIETY OF CHEMISTRY

RSC Advances

PAPER

View Article Online
View Journal | View Issue

Cite this: *RSC Adv.*, 2017, **7**, 42064

Nitrogen-rich green leaves of papaya and *Coccinia grandis* as precursors of activated carbon and their electrochemical properties

Paweena Dulyaseree,[ab] Masatsugu Fujishige,[b] Ichiro Yoshida,[b] Yumiko Toya,[b] Yasuo Banba,[b] Yu-suke Tanaka,[c] Takaaki Aoyama,[c] Mayuree Phonyiem,[a] Winadda Wongwiriyapan,*[a] Kenji Takeuchi*[b] and Morinobu Endo[b]

Activated carbon (AC) was synthesized from papaya and *Coccinia grandis* leaves (PL-AC and CL-AC, respectively) which are nitrogen-rich precursors and their electrochemical properties were investigated. The synthesis process included carbonization at 400 °C, impurity removal by H_2SO_4 cleaning, and post activation by NaOH at 720 °C. Surpassing the conventional bamboo-derived AC (B-AC), PL- and CL-ACs show relatively high surface areas of 2664 and 2576 m^2 g^{-1}, respectively. Moreover, the nitrogen contents in the PL- and CL-ACs were approximately 2.3 and 1.8 at%, respectively. Furthermore, the electrochemical properties of the synthesized PL- and CL-ACs were investigated using both aqueous and organic electrolytes. The specific capacitances of the PL- and CL-ACs were 98.47 and 89.91 F g^{-1}, respectively, in Na_2SO_4 electrolyte. Especially, compared to the B-AC, the PL-AC shows a dramatic decrease in series resistances (R_S) from 1.33 to 0.53 Ω and charge transfer resistances (R_{CT}) from 25.83 to 9.00 Ω. The decrease of R_S and R_{CT} is attributed to the existence of nitrogen in the PL-AC, resulting in a higher conductivity of electrode material and an enhancement of the charge transfer between electrode material and electrolyte. The large surface area of the PL- and CL-ACs was successfully achieved without detriment to the electrical conductivity. These results suggest that nitrogen-rich PL and CL are potential precursors for the synthesis of nitrogen-doped AC in a one-step process, which can be used as an alternative electrode material for electrochemical capacitors and can potentially be applied for large-scale industrial production with low cost.

Received 30th May 2017
Accepted 16th August 2017

DOI: 10.1039/c7ra06048c

rsc.li/rsc-advances

1. Introduction

Agriculture has long been the mainstay of the Thai economy, with abundant natural resources, and the majority of the Thai population engages in agricultural practices. The total area of Thailand is approximately 513 000 km^2 and 46% of this is used for agricultural purposes. After harvesting, there is a large amount of agricultural waste left. Thus, it is strongly desired to reduce the amount of agricultural waste and investigate the potential to maximize its uses. Agricultural waste can be used as feed for livestock, biomass energy, and raw material for activated carbon (AC) production. For use in AC, the raw materials are currently dominated by trunk, branch, shell, and seed of plants which are mainly composed of cellulose, lignin and hemicellulose.[1-7] The obtained AC exhibits a high content of carbon with high surface area and high porosity. These ACs can be used in a wide application such as gas purification, metal extraction, water purification, sewage treatment, air filters and electrode in energy storage devices. Besides the above mentioned parts of the plants, there is a growing interest in the use of green leaves as precursors for the AC production. The green leaves contain nitrogen and a pigment called chlorophyll responsible for photosynthesis. The green leaves-derived AC is expected to contain nitrogen which is initially included in the raw materials, affording one-step preparation process of the nitrogen-doped AC.[8-11] The nitrogen-doped AC has the potential to broaden the appeal of AC in both existing and emerging applications, especially in the use as electrode materials of high-performance electrochemical capacitor (EC).

Recently, EC has been focused due to the increasing energy crisis arising from the limited fossil fuels. EC has the potential to bridge the gap between battery and conventional capacitor, as the great advantages including high power density, high rates of charge/discharge and long cycle life.[12-16] To improve the performance of EC, most efforts have been focused on the improvement of electrode materials. AC is currently extensively

---

[a] *College of Nanotechnology, King Mongkut's Institute of Technology Ladkrabang, Chalongkrung Road, Ladkrabang, Bangkok 10520, Thailand. E-mail: winadda.wo@kmitl.ac.th*

[b] *Institute of Carbon Science and Technology, Shinshu University, 4-17-1 Wakasato, Nagano, 380-8553, Japan. E-mail: takeuchi@endomoribu.shinshu-u.ac.jp*

[c] *Interdisciplinary Graduate School of Science and Technology, Shinshu University, 4-17-1 Wakasato, Nagano, 380-8553, Japan*

examined and widely utilized as electrode materials with a focus on high specific surface area (SSA), hierarchical porous structure (combination of macro-, meso-, and micro-pores), and heteroatom doping (introduction of nitrogen (N) and oxygen (O) into the carbon framework).[8,17–19] In addition, heteroatom doping can improve capacitance value due to charge transfer from faradic reaction as well as the increased accessibility of the electrolytes to electroactive species.[8,18,20–23] The microstructure and the element composition of resulting AC largely depend on the raw materials. Thus, by selecting appropriate raw materials, the AC with a controlled microstructure and a desired amount of heteroatoms could be obtained.

In this study, a novel perspective of agricultural wastes for high-performance AC derived from green leaves, papaya and *Coccinia grandis* leaves (hereinafter referred to as PL and CL, respectively), is proposed. Papaya and *Coccinia grandis* are cultivated as an important food plant in many countries such as Mexico, India, Thailand, and Southeast Asia. The great popularity of papaya and *Coccinia grandis* may be attributed to several factors; it is easy to grow and has a high productivity. All parts of papaya tree and *Coccinia grandis* contain medicinal properties and are used by Thais as herbal medicine also. Synthesis of AC from PL and CL (hereinafter referred to as PL-AC and CL-AC, respectively) was demonstrated by carbonization at 400 °C followed with acid cleaning and NaOH activation. Surpassing the conventional bamboo-derived AC (hereinafter referred to as B-AC), the PL-and CL-ACs shows the hierarchical porous structure (combination of macro-, meso-, and micro-pores), high SSA, numerous heteroatom (O and N) groups, good electrical conductivity, and the wettability properties. To demonstrate their potential application as electrode material of the EC, the electrochemical properties of the PL- and CL-ACs were investigated. The specific capacitances of the PL- and CL-ACs were 98.47 and 89.91 F g^{-1}, respectively, in aqueous electrolyte. The PL-AC shows the dramatic decrease in the series resistances (R_S) from 1.33 to 0.53 Ω and the charge transfer resistances (R_{CT}) from 25.83 to 9.00 Ω. These results suggest that nitrogen-rich PL and CL are potential precursors for the synthesis of nitrogen-doped AC in one-step process and can potentially be applied for large-scale industrial production with a low cost.

2. Experimental

2.1 Preparation of activated carbon from papaya and *Coccinia* leaves

The PL and CL were used as the precursors of the AC production. The fresh PL and CL were obtained from Thailand local farm. The typical AC synthesis process is shown in Fig. 1. Firstly, the fresh leaves were washed with deionized water and dried in an oven at 100 °C for 12 h. The leaves were grinded into small pieces by a blender. The carbonization of the leaves was carried out at 400 °C for 2 h at a heating rate of 10 °C min^{-1} under argon flow rate of 500 mL min^{-1}. The carbonized sample was then washed with 1 M of sulfuric acid (H_2SO_4) on a hotplate at 100 °C for 3 h to remove impurities, and was repeatedly washed with deionized water until neutral pH. It was dried at 110 °C in ambient for 12 h. The activation process was conducted by the heat-treatment of a solid mixture of carbonized sample and sodium hydroxide (NaOH) (at the weight ratio of 1 : 2.5) in the tubular furnace at 720 °C for 1 h under argon gas at a flow rate of 500 mL min^{-1}. After that, the sample was washed with deionized water and dried under air ambient at 110 °C for overnight. The ACs thus derived from PL and CL are hereafter referred to as PL-AC and CL-AC, respectively. For comparison, the AC from the bamboo (hereafter referred to as B-AC) was prepared by the same processes.

2.2 Material characterizations

The morphologies of all the materials were characterized by scanning electron microscope (SEM, JEOL JSM-700F). The Raman spectra were observed by Raman spectroscope (Renishaw) using a laser wavelength of 532 nm. The nitrogen-adsorption isotherms were observed by the gas adsorption analyzer (Micromeritics ASAP 2020). The BET surface area and pore volume were determined from the adsorption isotherms. The calculation of pore volume was performed based on the method of density functional theory.[24] The elemental and the chemical composition of the sample were estimated by X-ray photoelectron spectroscopy (XPS, PHI Quantera II).

2.3 Characterization of electrochemical properties

To characterize the electrochemical properties of the synthesized AC, the AC samples were used as the host material of the electrodes of coin type supercapacitor. To construct the electrode, each AC sample was mixed with carbon black and polytetrafluoroethylene (PTFE) in the weight ratio of 90 : 5 : 5, respectively, in the mortar. Then, the mixture was pressed under applied pressure of 10 kN for 1 min to form an electrode pellet with a diameter of 10 mm, and subsequently dried at 100 °C for 12 h in a vacuum oven. The total mass loading of the electrode material was approximately 20 mg. Two types of electrolytes were used to characterize the electrochemical properties; 1 M Na_2SO_4 as an aqueous electrolyte and 1 M tetraethylammonium tetrafluoroborate (Et_4NBF_4) dissolved in propylene carbonate as an organic electrolyte. In the case of the aqueous electrolyte, the electrochemical performance was characterized using a conventional Teflon electrochemistry cell with a three-electrode cell, consisting of two identical electrode pellets on Ni foams with a relatively same weight separated by the a 30 μm-thick separator serving as working and counter electrodes, and a Ag wire as the reference electrode. In the case of the organic electrolyte, the electrochemical performance was determined using a conventional two-electrode coin cell, consisting of two identical electrode pellets with a relatively same weight separated by the a 30 μm-thick separator. All electrochemical tests were carried out by an electrochemical workstation (Bio-Logic Science Instruments VSP Potentiostat). The electrochemical properties were characterized by cyclic voltammetry (CV), galvanostatic charge–discharge (CD), and electrochemical impedance spectroscopy (EIS, with an amplitude of 5 mV in the frequency range of 1 MHz to 10 mHz). The specific capacitances of the supercapacitor (C_S) were evaluated from CD curves using the following equations:

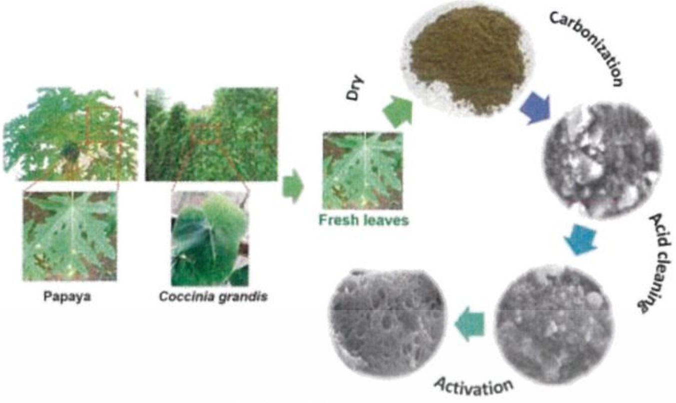

Fig. 1 Schematic illustration of activated carbon (AC) synthesis.

$$C_S = \frac{I \times \Delta t}{\Delta V \times m}$$

where C_S, I, Δt, ΔV and m are the specific capacitance (F g^{-1}), discharge current (A), discharge time (s), voltage change after a full charge or discharge (V) and the total loading mass of two electrode pellets (g), respectively.

3. Results and discussion

3.1 Morphology and structure characterization

Fig. 2 shows SEM images at low and high magnifications of the PL-AC (Fig. 2a and d), CL-AC (Fig. 2b and e), and B-AC (Fig. 2c and f), respectively. The morphologies of three types of AC were totally different. The PL-AC shows a sponge-like structure, with lots of pores, while the CL-AC contains many small wrinkled sheets fused each other. The B-AC shows the coagulation of fibrous and clustered particles. Fig. 3a shows the nitrogen adsorption and desorption isotherms at 77 K of each sample. The adsorption of nitrogen was remarkably increased in the relatively low pressure region and then gradually saturated. In addison, hysteresis was not obviously observed. The PL-AC shows the highest saturated adsorption amount. Thus, the AC samples can be classified as the type I isotherms (definition of IUPAC[25]), implying the existence of the microporous solids. Fig. 3b shows the pore size distribution of the AC samples obtained by the DFT method. It can be seen that all the samples have pore sizes mainly in the range of 0.5–3.7 nm, in which the

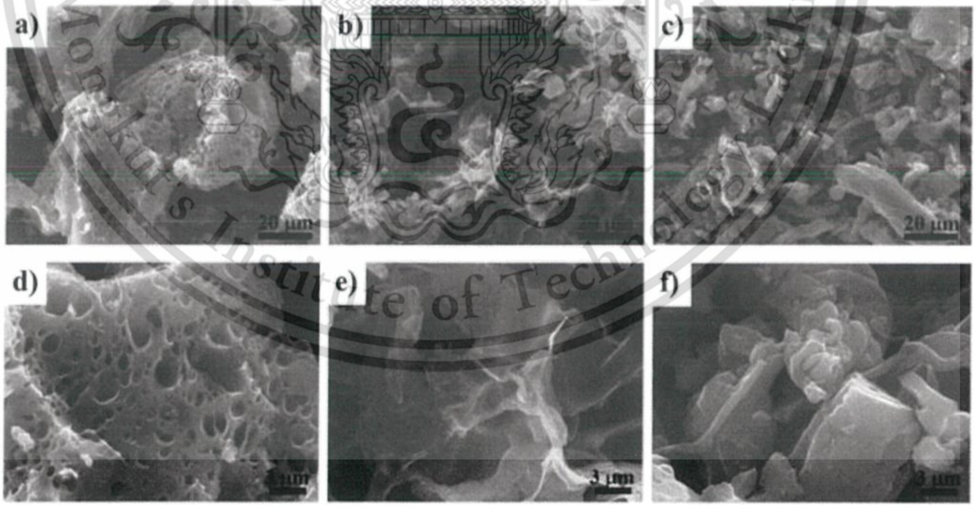

Fig. 2 SEM images at low and high magnifications: (a) and (d), PL-AC; (b) and (e) CL-AC; (c) and (f), B-AC.

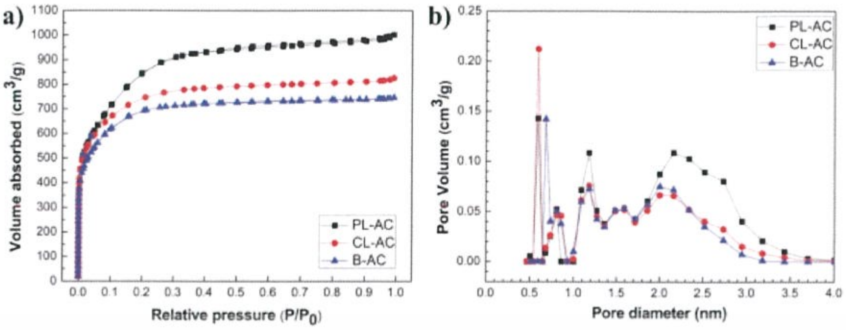

Fig. 3 (a) Nitrogen adsorption and desorption isotherms at 77 K, and (b) pore size distribution of PL-, CL- and B-ACs.

Table 1 Surface properties of ACs estimated from N_2 adsorption/desorption isotherms

Sample	S_{BET}[a] (m^2 g^{-1})	V_{total}[b] (cm^3 g^{-1})	V_{micro}[c] (cm^3 g^{-1})	V_{meso}[d] (cm^3 g^{-1})	V_{macro}[e] (cm^3 g^{-1})	V_{micro}/V_{total} (%)	V_{meso}/V_{total} (%)
PL-AC	2664	1.270	0.798	0.466	0.005	62.83	36.69
CL-AC	2576	1.054	0.824	0.221	0.008	78.18	20.96
B-AC	2370	0.968	0.796	0.191	0.008	79.44	19.73

[a] BET specific surface area. [b] DFT total pore volume. [c] DFT micro-pore volume. [d] DFT meso-pore volume. [e] DFT macro-pore volume.

PL- and CL-ACs possess the highest pore volume at the diameter of 0.6 nm, in comparison with that at slightly larger diameter of 0.7 nm for B-AC. The specific surface area (S_{BET}) and pore volume of all the samples calculated from nitrogen adsorption/desorption isotherms were summarized in Table 1. The PL-AC has the highest S_{BET} (2664 m^2 g^{-1}) and V_{total} (1.27 cm^3 g^{-1}), whereas the B-AC has the lowest S_{BET} (2370 m^2 g^{-1}) and V_{total} (0.97 cm^3 g^{-1}). The S_{BET} and V_{total} of the CL-AC are 2576 m^2 g^{-1} and 1.05 cm^3 g^{-1}, respectively. The PL-AC is characterized by the relatively high V_{micro} (0.798 cm^3 g^{-1}) and the highest V_{meso} (0.466 cm^3 g^{-1} with pore sizes ranging from 2.0 to 3.7 nm). The ratios of the V_{micro} to V_{total} and the V_{meso} to V_{total} of the PL-AC are 62.83 and 36.69%, respectively. The existence of mesopores in the AC provides a favorable path for transportation and penetration of electrolyte ion, which is important for fast ion transfer.[19]

Fig. 4 shows Raman spectra of the AC samples. All the AC samples exhibit two broad overlapping bands, which are the so-called D-band originated from the defects and disordered carbon structure at a Raman shift of around 1360 cm^{-1}, and the G-band originated from the graphitic structure at a Raman shift of around 1600 cm^{-1}.[26,27] The ratio of the intensities of the D peak to the G peak (D/G ratio) is generally used as the measure of the degree of graphitization of activated carbon, and the higher ratio means the lower degree of graphitization.[27] The corresponding values of the D/G ratio were 1.00, 0.988, and 0.941 for the PL-, CL- and B-AC, respectively. The high D/G ratio indicates the less graphitized carbons.[28,29] It is known that the introduction of nanoscale pores on carbon framework usually leads to an increase of defects and disorders.[30] Thus, the relatively high D/G ratio of the PL- and CL-ACs implies the structural defects are concerned with the large pore volume in the PL- and CL-ACs. The above results confirms that the PL and CL can be used as the promising precursors to obtain the AC containing nanoporous carbon with relatively large specific surface area and micro-pore volume surpassing the B-AC and the commercial AC (Kansai Coke and Chemicals Company).[7]

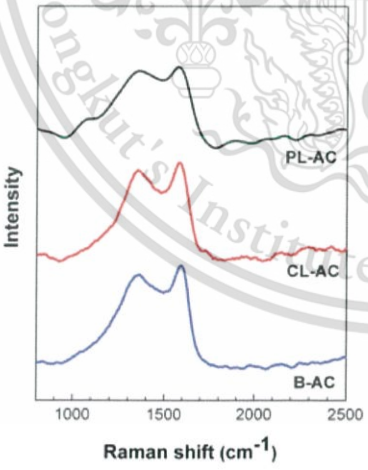

Fig. 4 Raman spectra of PL-, CL- and B-ACs.

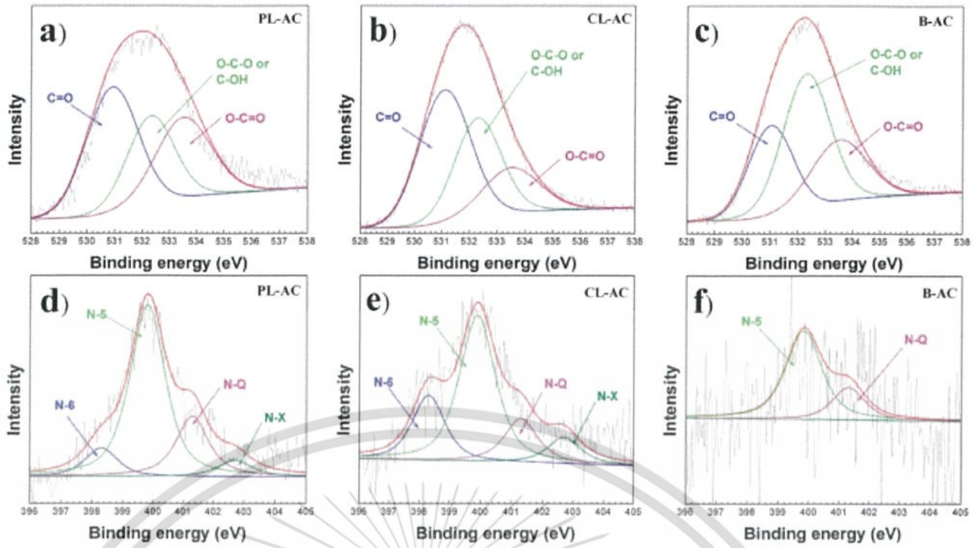

Fig. 5 O 1s and N 1s XPS spectra of PL-, CL- and B-ACs: (a) and (d), PL-AC; (b) and (e), CL-AC; (c) and (f), B-AC.

3.2 Elemental and chemical composition

The chemical composition of the AC samples was studied by XPS. Fig. 5 shows XPS spectra of O 1s and N 1s observed for the AC samples. The chemical composition, N/C ratio and the relative N 1s peak area are summarized in Table 2. The PL-AC shows the highest nitrogen content (2.3 at%) and the N/C ratio (0.025), while the CL-AC shows the highest oxygen content of 9.5 at%. The PL- and CL-ACs show relatively high nitrogen content compared to that of the B-AC, implying that nitrogen-rich leaves can be used as precursors of the nitrogen-doped AC. The high-resolution O 1s spectra, shown in Fig. 5a–c, can be divided into three different binding configurations, including O–C=O in carboxylic (533.5 eV), O–C–O/C–OH in ester or phenol (532.2 eV), and C=O in carbonyl/quinone (531.2 eV).[18-31] The content of oxygen functional groups included in each AC is different. The dominant oxygen functional group in the PL- and CL-ACs is C=O, while that of the B-AC is O–C–O/C–OH. On the other hand, the high-resolution N 1s spectra, shown in Fig. 5d–f, can be deconvoluted by incorporation of four contributions including pyridine N (398.3 eV, N-6), pyrrolic N (399.89 eV, N-5), quaternary N (401.3 eV, N-*Q*) and oxidized pyridine N (402.70 eV, N-*X*).[18,31,32] The content of nitrogen functional groups included in the green leaves-derived ACs and the B-AC are completely different. The PL- and CL-ACs show the compositions of N-6, N-5, N-*Q* and N-*X*, with the highest content of N-5, while the B-AC shows only the compositions of N-5 and N-*Q*. Normally, N-5 and N-6 are the defects in the graphene layer and could induce pseudocapacitance property. In addition, high content N-*Q* group in AC obviously improve the electronic conductivity and the high content of N-*X* implies the wettability properties. These results show that the raw materials of AC directly affect the microstructure and heteroatom doping properties. Owing to the hierarchical porous structure (combination of macro-, meso-, and micro-pores), high SSA, numerous heteroatom (O and N) groups, good electrical conductivity, and the wettability properties of the PL-and CL-ACs which are important requirements of an ideal electrode material of EC, it is a challenge to investigate the potential of the PL-and CL-ACs as the electrode material of EC.

Table 2 Chemical composition of PL-, CL- and B-ACs evaluated from elemental analysis

	Content (at%)				Relative N 1s peak area[a] (%)			
Sample	C	O	N	N/C ratio	N-6	N-5	N-*Q*	N-*X*
PL-AC	91.0	6.6	2.3	0.025	0.21	1.44	0.50	0.14
CL-AC	87.3	9.5	1.8	0.021	0.39	0.95	0.28	0.17
B-AC	89.3	9.1	0.1	0.001	—	0.07	0.03	—

[a] Pyridine N (N-6), pyrrolic N (N-5), quaternary N (N-*Q*) and oxidized pyridine N (N-*X*).

3.3 Electrochemical properties in aqueous electrolyte

The electrochemical properties of the AC samples were investigated in a three-electrode system using 1 M Na_2SO_4 aqueous electrolyte. The cyclic voltammetry (CV) curves collected at a scan rate 1 mV s^{-1}, and galvanostatic charge–discharge (CD) at an applied constant current of 5 mA are presented in Fig. 6a and b, respectively. The CV curves in a potential window from −1.0 to 0 V present quasi-rectangular shapes with obvious reversible hump, suggesting the capacitive response combination between the electrical double-layer capacitor (EDLC) and pseudo-

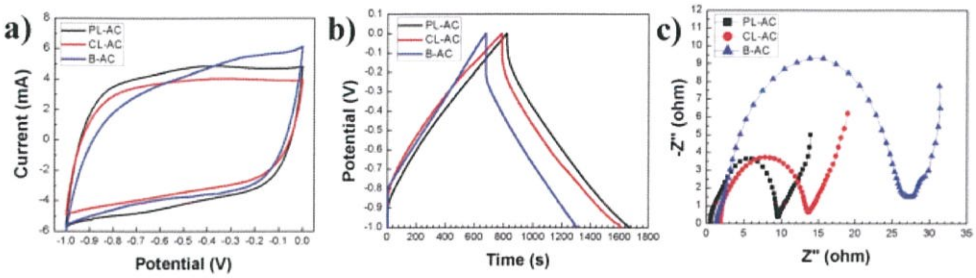

Fig. 6 Electrochemical properties of the PL-, CL- and B-ACs in 1 M Na_2SO_4 electrolyte from −1 to 0 V: (a), cyclic voltammetry curve at a scan rate 1 mV s^{-1}; (b), galvanostatic charge–discharge curve of papaya electrode material at an applied constant current of 5 mA; (c), Nyquist plot in the frequency range of 1 MHz to 10 mHz at an amplitude of 5 mV.

capacitor. The PL-AC exhibits the largest area of CV curve, indicating the highest capacitance due to the high specific surface area and the high nitrogen content. The steep slopes of the current change at the switching potential at a potential of −0.7 V indicate a small mass-transfer resistance of all electrodes. Obviously, the hierarchical pore structure of all materials provides a short ion pathway and electrolyte reservoir for rapid ionic transportation. The CD curves (Fig. 6b) show a shape of an imperfectly symmetrical triangle, indicating that all AC samples have good electrochemical behaviors accompanied by the pseudocapacitive contribution of the functional group. From CD curves, the specified capacitances of the PL-, CL- and B-ACs were approximately 98.47, 89.91, and 83.68 F g^{-1}, respectively. The excellent capacitive behavior of the PL-AC-based EC was also reflected in their long charge–discharge time. The best electrochemical performance of the PL-AC is attributed to the co-contribution of the high electronic double-layer capacitance due to its high surface area and the additional pseudocapacitance mainly derived from the doped nitrogen. To further understand the origin of the improved electrochemical performance of the PL-AC, the EIS characteristics were investigated.

Fig. 6c shows the Nyquist plots of all AC samples in the frequency range of 1 MHz to 10 mHz at an amplitude of 5 mV. The EIS spectra consist of a semicircle in the high-frequency and a linear line in the low-frequency regions. All AC samples show resembles semicircle curve, but different offsets on the *x*-axis and different diameters, revealing their different characteristics. The offset on the *x*-axis (Z') (Ω) of the high-frequency semicircle is a series resistance (R_S) of the electrode consisting of the electrode material resistance, the electrolyte resistance and the contact resistance between the electrode material and the current collector. The values of R_S of the PL-, CL- and B-ACs are estimated to be 0.53, 1.82, and 1.33 Ω, respectively. The diameter of the semicircle represents the kinetic resistance to the charge transfer, called the charge transfer resistance (R_{CT}). The values of R_{CT} of the PL-, CL- and B-ACs are estimated to be 9.00, 11.86, and 25.83 Ω, respectively. In the case of AC, its properties in terms of surface area, pore structure and conductivity need to be monitored as these properties can be mutually exclusive, that is, one can be improved only to the detriment of another. In this experiment, the significant decrease in R_S and R_{CT} of the PL-AC although its relatively large surface area compared to that of the B-AC can be ascribed to the combination properties of high surface area, hierarchical porous structure, and nitrogen doping. In respect of the low value of R_S, it may be attributed to the N-*Q* existence. The quaternary N atoms take the position inside an aromatic ring with sp^2 hybridization and fully saturated bonding, and further enhance the electrical conductivity of the carbon material.[33] This is evidenced by the high content of N-*Q* in the PL-AC compared to the B-AC as shown in Table 2, resulting in the low R_S of the PL-AC although its high surface area. In respect of the value of R_{CT}, it can be attributed to the following reasons: (i) nanoporous carbon of electrode materials. The large volume of the mesopore of the PL-AC compared to that of the CL- and B-ACs leads provide the accessible route to electrolyte to enter into electrode more easily.[34] (ii) the existence of negatively charged nitrogen-containing groups of N-5 and N-6. Generally, N-5 and N-6 species lie at the edges of graphitic layer, where nitrogen atom is bonded to two carbon atoms, creating cavities and defects. The nitrogen atom of N-6 contributes one π-electron to the aromatic ring and has a lone electron pair in the plane of ring, whereas the nitrogen atom of N-5 contributes two π-electron and a hydrogen atom is bound in the plane of the ring.[35,36] Due to the high electron density, N-5 and N-6 act as the acceptor and can accept the donors, thereby causing the faradic reaction for contributing to pseudocapacitance (as expressed by e^- with the curved blue arrows in Fig. 8). This is evidenced by the high content of N-5 and N-6 in the PL- and CL-ACs compared to the B-AC as shown in Table 2. (iii) The existence of the positively charged nitrogen-containing groups of N-*Q* and N-*X*. The N-*Q* and N-*X* are the nitrogen species that the nitrogen atom substitutes carbon atom in aromatic ring, and the oxidized pyridine nitrogen atom, respectively, providing the positively charge. Since fast electron transfer is a crucial requirement to keep the constant energy at any operation load. Most of electrochemical capacitors based on porous carbon often suffer from a capacitance drop caused by an increase in the ohmic resistance of porous carbon. Thus, the enrichment of carbons with positively charged N-*Q* and N-*X* may help in electron transfer through the porous carbon, resulting in enhancing the capacitance (as expressed by e$^-$ with the straight yellow arrows in Fig. 8).[18] This is evidenced by the high content of N-*Q* and N-*X* in the PL- and CL-ACs compared to the B-AC as shown in Table 2. (iv) The existence of oxygen-containing functional groups. Generally, the micropores of carbon cannot be fully wetted in aqueous electrolyte, and thus are not fully accessible to electrolyte.[37] Oxygen-containing functional groups such as C=O and/or C–OH, and the oxidized pyridine (N-*X*) may improve carbon wettability of the internal structure of micropores, thus resulting in a corresponding decrease in R_{CT} and increase in specific capacitance (as expressed by ions of aqueous electrolyte in Fig. 8). The B-AC could also deliver the relatively good capacitance owing to the existence of the oxygen-containing functional groups and thus compensate the low concentration of nitrogen-containing groups and its relatively low surface area.

3.4 Electrochemical properties in organic electrolyte

To investigate the versatile use of the green leaves-derived AC in various types of electrolyte, the electrochemical performance of the AC samples were also characterized in the organic electrolyte in order to achieve higher operational voltages and therefore greater specific energy. Similar to the case of aqueous electrolyte, the rectangular CV curves at a scan rate 1 mV s^{-1} in a potential window from 0 to 2.5 V were obtained confirming the electrochemical properties (Fig. 7a). The imperfectly symmetrical triangle of the CD curves in an applied constant current of 5 mA shown in Fig. 7b also indicates their electrochemical properties. From the Nyquist plot shown in Fig. 7c, the PL-, CL- and B-ACs show the R_S of 1.05, 1.27 and 2.40 Ω, respectively, with the R_{CT} of 13.60, 23.06 and 44.02 Ω, respectively. The increase in the R_S and R_{CT} in the organic electrolyte compared to that of aqueous electrolyte is due to the lower ionic conductivity of the organic electrolyte. Nevertheless, the PL-AC shows the smallest R_S and R_{CT}, especially with the 3.4-fold lowering in R_{CT} compared to that of the B-AC. The specific capacitances calculated from the charge–discharge measurement of all AC samples at different current densities ranging from 0.02 to 0.5 A g^{-1} are shown in Fig. 7d. The PL-AC shows the highest specified capacitances of 47 F g^{-1} at the current density of 0.02 A g^{-1} with the relatively stable specific capacitance at the high current density up to 0.5 A g^{-1}, implying the relatively high capacitance retention of 95.65%. The specific capacitances of the CL- and B-ACs are 45 and 42 F g^{-1}, respectively. Moreover, the energy density and the power density were calculated at the current density of 0.5 A g^{-1}. The energy density of the PL-, CL- and B-ACs was approximately 39, 33 and 30 W h kg^{-1}, respectively, while the power density of the PL-, CL- and B-ACs was approximately 1.7, 3.3 and 4.4 kW kg^{-1}, respectively.

Fig. 7e shows the specific capacitance *vs.* the cycle numbers of CD cycles at the constant current of 10 mA of all AC samples. The specific capacitance of the PL-, CL- and B-ACs remains 98.70, 95.02 and 91.26% after 3500 CD cycles. All AC samples

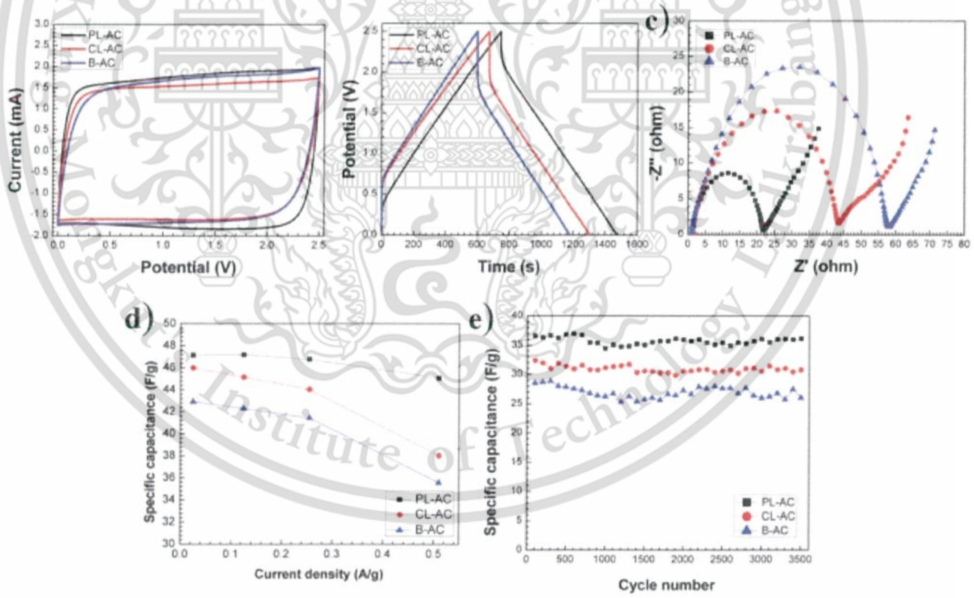

Fig. 7 Electrochemical properties of the PL-, CL- and B-ACs in 1 M Et_4NBF_4 electrolyte from 0 to 2.5 V: (a), cyclic voltammetry curve at a scan rate 1 mV s^{-1}; (b), galvanostatic charge–discharge curve at an applied constant current of 5 mA; (c), Nyquist plot in the frequency range of 1 MHz to 10 mHz at an amplitude of 5 mV; (d), dependence of specific capacitance on current density from 1.27 to 25.46 mA cm^{-2}; (e), cycling stability at an applied constant current of 10 mA.

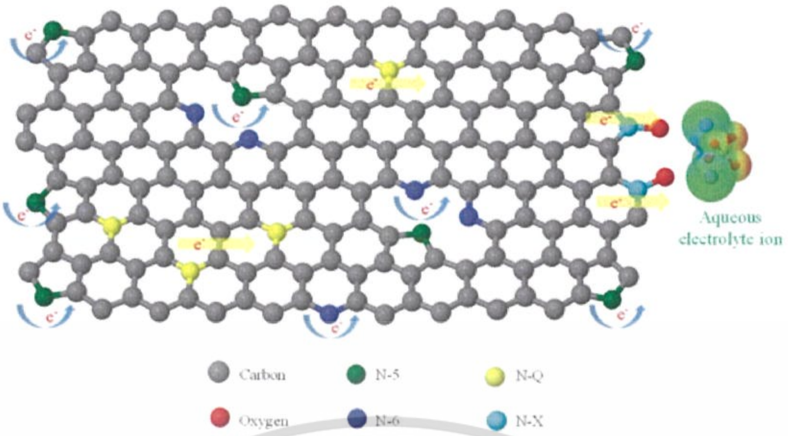

Fig. 8 Schematic view of the effect of the properties of the N-5, N-6, N-*Q* and N-*X* on the charge transfer resistance.

show good stability with good retention of capacitance. The specific capacitance, energy density and power density of the PL-AC is relatively comparable to AC derived from other parts of the tree.[8,9,11,38,39] In our study, not only the specific surface area of the activated carbon, the effect of the role of heteroatom doping (nitrogen and oxygen) on electrochemical properties also discussed. The morphology and structure of the PL-AC can be further maximized by using the optimized activation agent such as the mixing of K_2CO_3 and KOH, which is importance in enlargement of pore channel, providing the relatively high specific surface area.[17]

4. Conclusion

In summary, the nitrogen-containing ACs derived from the green leaves of PL and CL were successfully synthesized by carbonization, acid cleaning and chemical activation processes. The PL- and CL-ACs show the relatively high specific surface area of 2664 and 2576 $m^2\ g^{-1}$, respectively, compared to that of the B-AC (2370 $m^2\ g^{-1}$). The nitrogen contents composing of N-6, N-5, N-*Q* and N-*X* including in the PL- and CL-ACs was approximately 2.3 and 1.8 at%, respectively. Thus, the PL- and CL-ACs offer the relatively high specific surface area, hierarchical porous structure (combination of macro-, meso-, and micro-pores), good conductivity and heteroatom doping, fulfilling the requirement of the use as the electrode material of AC. The PL- and CL-ACs shows excellent electrochemical properties in both aqueous and organic electrolytes. The specific capacitances of the PL- and CL-ACs were 98.47 and 89.91 F g^{-1}, respectively, comparable to 83.68 F g^{-1} of the B-AC in Na_2SO_4 electrolyte. Especially, compared to the B-AC, the PL-AC shows the dramatic decrease in the series resistances (R_S) from 1.33 to 0.53 Ω and the charge transfer resistances (R_{CT}) from 25.83 Ω to 9.00 Ω. The decrease of R_S and R_{CT} is attributed to the existence of the nitrogen in the PL-AC, resulting in a higher conductivity of electrode material and an enhancement of the charge transfer between electrode material and electrolyte. These results suggest that nitrogen-rich PL and CL are potential precursors for the synthesis of nitrogen-doped activated carbon by one-step process, and can potentially be applied for large-scale industrial production with a low cost.

Contributions

Synthesis and characterizations were done by P. D., M. F., I. Y., Y. T., Y. B, Y. T., T. A. and M. P. Manuscript was written by P. D., M. F., W. W., K. T. and M. E. with discussions.

Conflicts of interest

There are no conflicts to declare.

Acknowledgements

This research was partially supported by grants from the Project of the NARO Bio-oriented Technology Research Advancement Institution (Integration research for agriculture and interdisciplinary fields). We also thank Dr Noboru Akuzawa of Shinshu University for his kind suggestions. We also acknowledge the support from the Strategic Scholarships Fellowships Frontier Research Networks (Specific for Southern region) from the Office of the Higher Education Commission (OHEC).

References

1 J. Deng, T. Xiong, H. Wang, A. Zheng and Y. Wang, *ACS Sustainable Chem. Eng.*, 2016, **4**, 3750–3756.

2 M. Z. Hussein, M. B. Abdul Rahman, A. H. Yahaya, Y. H. Taufiq-Yap and N. Ahmad, *J. Porous Mater.*, 2001, **8**, 327–334.

3 A. Jain, V. Aravindan, S. Jayaraman, P. S. Kumar, R. Balasubramanian, S. Ramakrishna, S. Madhavi and M. P. Srinivasan, *Sci. Rep.*, 2013, **3**, 1–6.

4 M. Dhelipan, A. Arunchander, A. K. Sahu and D. Kalpana, *J. Saudi Chem. Soc.*, 2016, **21**, 487–494.

5 R. K. Gupta, M. Dubey, P. Kharel, Z. Gu and Q. H. Fan, *J. Power Sources*, 2015, **274**, 1300–1305.

6 S. Uçar, M. Erdem, T. Tay and S. Karagöz, *Appl. Surf. Sci.*, 2009, **255**, 8890–8896.

7 M. Fujishige, I. Yoshida, Y. Toya, Y. Banba and K. Oshida, *Biochem. Pharmacol.*, 2017, **5**, 1801–1808.

8 G. Ma, J. Li, K. Sun, H. Peng, E. Feng and Z. Lei, *J. Solid State Electrochem.*, 2017, **21**, 525–535.

9 B. Liu, Y. Liu, H. Chen, M. Yang and H. Li, *J. Power Sources*, 2017, **341**, 309–317.

10 X. Xia, H. Liu, L. Shi and Y. He, *J. Mater. Eng. Perform.*, 2012, 21, 1956–1961.

11 H. Peng, G. Ma, K. Sun, Z. Zhang, Q. Yang and Z. Lei, *Electrochim. Acta*, 2016, **190**, 862–871.

12 P. Simon and Y. Gogotsi, *Nat. Mater.*, 2008, 7, 845–854.

13 J. R. Miller and P. Simon, *Science*, 2008, 321, 651–653.

14 C. Arbizzani, M. Mastragostino and F. Soavi, *J. Power Sources*, 2001, **100**, 164–170.

15 A. Burke, *Electrochim. Acta*, 2007, **53**, 1083–1091.

16 R. Kötz and M. Carlen, *Electrochim. Acta*, 2000, **45**, 2483–2498.

17 Y. T. Li, Y. T. Pi, L. M. Lu, S. H. Xu and T. Z. Ren, *J. Power Sources*, 2015, **299**, 519–528.

18 B. D. Hulicova-jurcakova, M. Seredych, G. Q. Lu and J. Bandosz, *Adv. Funct. Mater.*, 2009, **19**, 438–447.

19 X. Ying, C. Chen, Z. Jie, D. Hua, X. Deng and J. Wei, *J. Power Sources*, 2013, **230**, 50–58.

20 M. Inagaki, H. Konno and O. Tanaike, *J. Power Sources*, 2010, 195, 7880–7903.

21 A. Chen, Y. Wang, Y. Yu, H. Sun, Y. Li, K. Xia and S. Li, *J. Mater. Sci.*, 2017, 52, 3153–3161.

22 B. Duan, X. Gao, X. Yao, Y. Fang, L. Huang, J. Zhou and L. Zhang, *Nano Energy*, 2016, **27**, 482–491.

23 J. Chang, Z. Gao, X. Wang, D. Wu, F. Xu, X. Wang, Y. Guo and K. Jiang, *Electrochim. Acta*, 2015, **157**, 290–298.

24 J. P. Olivier, *Carbon*, 1998, **36**, 1469–1472.

25 M. Thommes, K. Kaneko, A. V. Neimark, J. P. Olivier, F. Rodriguez-Reinoso, J. Rouquerol and K. S. W. Sing, *Pure Appl. Chem.*, 2015, **87**, 1051–1069.

26 M. S. Dresselhaus, G. Dresselhaus, R. Saito and A. Jorio, *Phys. Rep.*, 2005, **409**, 47–99.

27 M. S. Dresselhaus, A. Jorio, M. Hofmann, G. Dresselhaus and R. Saito, *Nano Lett.*, 2010, **10**, 751–758.

28 T. C. Chieu, M. S. Dresselhaus and M. Endo, *Phys. Rev. B: Condens. Matter Mater. Phys.*, 1982, **26**, 5867–5877.

29 C. Hu, S. Sedghi, A. Silvestre-Albero, G. G. Andersson, A. Sharma, P. Pendleton, F. Rodrguez-Reinoso, K. Kaneko and M. J. Biggs, *Carbon*, 2015, **85**, 147–158.

30 H. Wang, Z. Xu, A. Kohandehghan, Z. Li, K. Cui, X. Tan, T. J. Stephenson, C. K. King, C. M. B. Holt, B. C. Olsen, J. K. Tak, D. Harfield, A. O. Anyia and D. Mitlin, *ACS Nano*, 2013, **7**, 5131–5141.

31 R. Arrigo, M. Ha, S. Wrabetz, R. Blume, M. Lerch, J. Mcgregor, E. P. J. Parrott, J. A. Zeitler, L. F. Gladden, A. Knop-gericke, R. Schlo and D. S. Su, *J. Am. Chem. Soc.*, 2010, **132**, 9616–9630.

32 M. Zhou, F. Pu, Z. Wang and S. Guan, *Carbon*, 2013, **68**, 185–194.

33 M. Yang and Z. Zhou, *Adv. Sci.*, 2017, 1600408.

34 N. Guo, M. Li, Y. Wang, X. Sun, F. Wang and R. Yang, *RSC Adv.*, 2016, **6**, 101372–101379.

35 J. R. Pels, F. Kapteijn, J. A. Moulijn, Q. Zhu and K. M. Thomas, *Carbon*, 1995, **33**, 1641–1653.

36 J. Casanovas, J. M. Ricart, J. Rubio, F. Illas and J. M. Jiménez-Mateos, *J. Am. Chem. Soc.*, 1996, **118**, 8071–8076.

37 C. T. Hsieh and H. Teng, *Carbon*, 2002, **40**, 667–674.

38 C. Chen, D. Yu, G. Zhao, B. Du, W. Tang, L. Sun, Y. Sun, F. Besenbacher and M. Yu, *Nano Energy*, 2016, **27**, 377–389.

39 Y. Zhao, M. Lu, P. Tao, Y. Zhang, X. Gong, Z. Yang, G. Zhang and H. Li, *J. Power Sources*, 2016, **307**, 391–400.